ISSN 2435-7499 (Online)
ISSN 2189-6909 (Print)
December 2023

LASTI
Annual Report

Laboratory of Advanced Science and Technology for Industry
University of Hyogo

Vol.24 (2022)

Preface

This annual report reviews the research activities of the Laboratory of Advanced Science and Technology for Industry (LASTI) in the academic year of 2022 which is from April 2022 to March 2023 including research activities using NewSUBARU light source at the SPring-8 site and other research activities carried out at the Center for Advanced Science and Technology (CAST) II. NewSUBARU facility has a 1.0-1.5 GeV electron storage ring, which provides light beams from infrared (IR) to hard X-ray regions, and is the largest university-operated synchrotron light facility in Japan.

At NewSUBARU, researches are mainly focusing on the academic fields of 1) development of new synchrotron light source technology, 2) the next generation lithography using extreme ultraviolet (EUV) conducted at beamlines BL3, BL9B, BL9C, and BL10, 3) applications of lithographie galvanoformung abformung (LIGA) process technology at BL2 and BL11, 4) materials analysis by X-ray absorption spectroscopy at BL5, BL7 and BL9A, X-ray emission spectroscopy at BL9A, and photoemission spectroscopy at BL7. Other than the synchrotron radiation researches, various researches, such as material syntheses, device fabrication, and microfluid mechanics, are also being conducted at CAST II. Most of our research activities are being conducted in collaboration research works with industries, research institutes, and other universities, inside and outside Japan. We would like to take this opportunity to thank all the collaborators.

Previously, the Spring-8 linear accelerator had also been used to injection of the electron beam to the NewSUBARU electron storage ring in cooperation of the Spring-8 accelerator team. However, the new linear accelerator dedicated to NewSUBARU was installed at the beam transportation tunnel in 2020 and it started operation in April 2020. The construction of the new injector has been completed in great cooperation of the SPring-8 accelerator team. We would like to appreciate the SPring-8 accelerator team for their huge contributions.

Satoru Suzuki

Satoru Suzuki

Director of Laboratory of Advanced Science and Technology for Industry,
University of Hyogo

CONTENTS

Part 1. Current Status of NewSUBARU

Part 2. Research Activities

Beamlines

Koji Nakanishi
LASTI, University of Hyogo

The arrangement of the beamlines in the NewSUBARU synchrotron radiation (SR) facility is shown in Fig.1. Total nine beamlines are operating in the NewSUBARU SR facility. Four beamlines of BL01, 03, 06 and 11 were constructed until 1999. Three beamlines of BL07, 09 and 10 were started the operation from 2000. BL02 beamline was constructed for the usage of LIGA in 2003. BL03B beamline branched from the BL03 beamline propose for the usage of the EUVL (extreme ultraviolet lithography) microscope for the EUVL finished mask inspection. BL05 was built to perform industrial analysis by soft/tender X-ray XAFS in 2008. A major upgrade was started in 2020 for more effective use. The tender X-ray XAFS capabilities that are part of BL05 have been upgraded and moved to BL06. BL06 was reconstructed as a tender X-ray XAFS beamline and will be further upgraded in 2022 to enable soft/hard X-ray (1-10 keV) XAFS. A new high-vacuum measurement chamber for soft X-ray XAFS and a load lock chamber with transfer vessel were installed in BL09A. BL09B beamline branched from BL09 beamline for the usage of the EUV interference lithography to evaluate. And BL09C beamline branched from BL09B beamline for the usage of the thickness measurement of the carbon contamination originated to the resist outgassing during the EUV exposure.

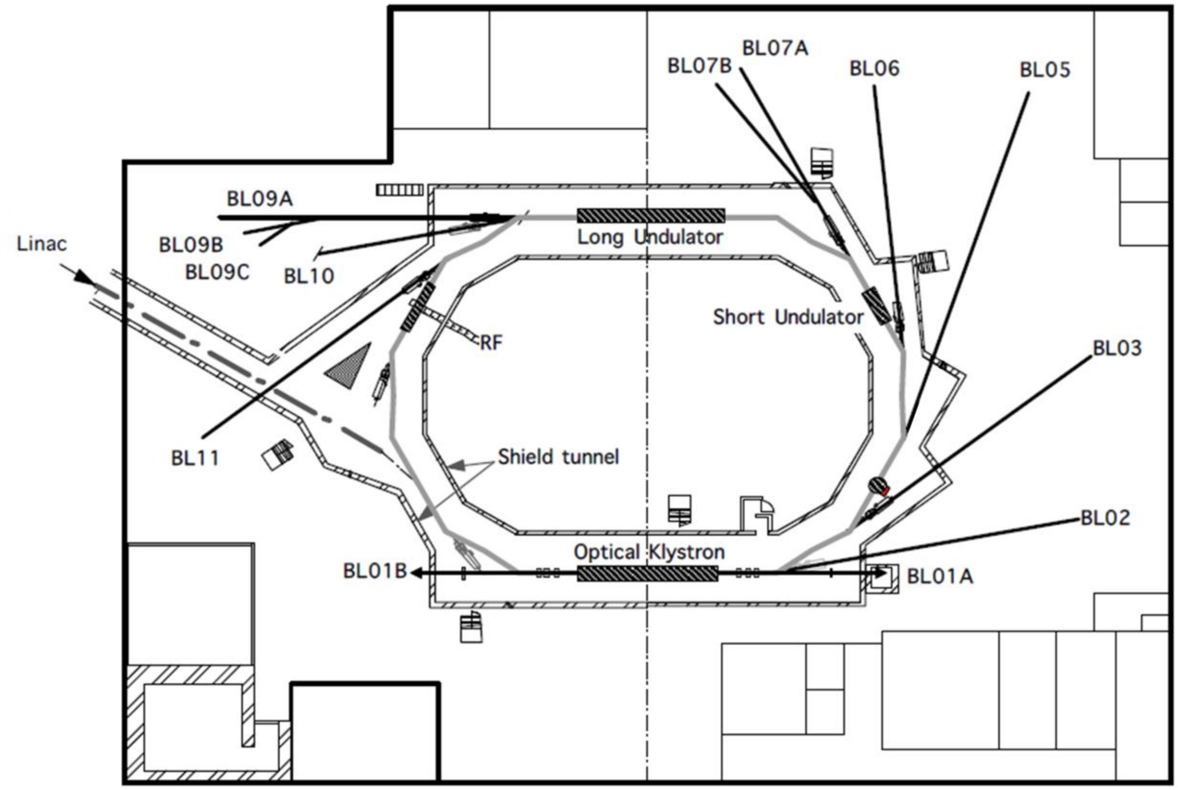

Figure 1. Beamline arrangement in NewSUBARU.

BL01 is a beamline for research and developing new light sources. This beamline is one of two long straight section on NewSUBARU. Optical klystron was installed at this straight section. Upstream side of this beamline (BL01B) is intended to be used for visible and infrared light generated from free electron laser (FEL) or synchrotron radiation (SR). Downstream side of this beamline (BL01A) is used for laser Compton scattering gamma-rays source. 2Gamma-ray beamline hutch just outside of the storage ring tunnel was constructed in 2004 for gamma-ray irradiation experiments. Specification of this gamma-ray sources are listed in Table 1. New gamma-ray irradiation hutch "GACKO" was installed at BL01A. Table 2 shows the specification of “GACKO”.

Table 1. Specification of BL01 gamma beam

CO_2 laser 10.52 µm 5W	Gamma energy : 1.7 - 4 MeV Gamma flux*: 9 ×10^6 γ/s : 6×10^5 γ/s (1.5-1.7 MeV) (with 3mmφ collimator)
Nd laser 1.064 µm / 0.532 µm 5 W	Gamma energy : 17 - 40 MeV Gamma flux*: 7.5 ×10^6 γ/s : 3 ×10^5 γ/s (15-17 MeV) (with 3 mmφ collimator)

*Electron beam energy : 1-1.5 GeV
*Electron beam current : 250 mA
*Gamma-ray beam divergence : 0.5 mrad

Table 2. Specification of “GACKO”

Maximum gamma-ray power	0.33 mW
Maximum gamma-ray energy	1.7 MeV - 73 MeV
CO_2 laser, wavelength/power	10.59 µm / 10W
1-1.7 MeV gamma-ray flux	2×10^7 γ/sec@10W/300mA
Nd:YVO_4 laser, wavelength/power	1.064 µm/ 30W, 0.532 µm/ 20W
10-17 MeV gamma-ray flux	5×10^7 γ/sec@30W/300mA

II. BL02

The LIGA (abbreviated name of Lithogaphic, Galvanoformung and Abformung) process which consists from deep X-ray lithography, electroforming, and molding process is one of the promising candidates for such 3D micofabrication. More than hundreds aspect ratio for microstructure can be attained by the usage of the higher energy X-rays (4-15 keV) from synchrotron radiation (SR) with deeper penetration depth to the photosensitive resist. In this system we have succeeded to enlarge the exposure area up to A4 size and the fabrication dimension from submicron to millimeter by varying the energy of the X-ray source in accordance with the size of desired microparts. Microstructure with high aspect ratio over several hundred will be achieved using the X-rays over 10 keV since high energy X-ray has deep penetration depth to the photo-sensitive resist materials. Whereas, in the case of lithography for low energy X-rays from 1 keV to 2 keV, submicron structures with high aspect ratio will be achieved using the X-rays mask with precise line-width and thinner absorber, since low energy X-rays has low penetration depth. Based on this principle, the beamline for x-ray exposure have constructed with continuous selectivity of X-rays from 100 eV to 15 keV by using the X-ray mirrors (plane and cylindrical mirror) and Be film filters. The horizontal angle of the outgoing SR could be obtained up to 12.5 mrad, which corresponds to the horizontal size of 220 mm (A4 horizontal size) at the exposure position. The second characteristic performance of the beamline is the high efficiency differential pumping system. This was necessary for maintain the vacuum difference between the storage ring ($<10^{-9}$ Pa) and the end-station ($<10^{-9}$ Pa) at which gasses for substrate cooling will be introduced in the exposure apparatus.

The flexibility for the shapes and functions of microstructure will be enlarged by achieving 3D microfabrication process using multi step exposure at various configuration between X-ray mask and substrates.

The relative positions between X-ray mask and substrates, tilt and rotation angle to the SR incident direction can be moved simultaneously during SR exposure using 5 axis stages. The movement of each axis is controlled by the PC in terms of the scanning speeds, scanning length, and repetition number. In order to decrease the heat load of sample substrate suffered during SR irradiation helium introduction and substrate cooling mechanism were also equipped. Specification of spectrometer is listed in Table 3.

Table 3. Specification of the LIGA exposure system

Optics	Plane and cylindrical mirror, Be filters
Exposure energy	0.1 - 2 keV, and 4 – 15 keV
Exposure method	Proximity and multi-step exposure
Wafer size	A4 or 8 inch
Exposure area	230 mm(H) ×300 mm(V)
Exposure environment	< 1 atm (He-gas)

III. BL03

BL03 is a beamline for the developing the next generation lithographic technology so called extreme ultraviolet (EUV) lithography. The extreme ultraviolet lithography (EUVL) is a promise technology for fabricating a fine pattern less than 7-nm node. There are (1) a EUV resist-sensitivity evaluation tools, (2) a VUV reflectometer, and (3) an EUV microscope with Schwarzschild optics. At (1) tool, EUV resist is exposed with SR light of EUV monochromatized by 7 Mo/Si multilayer mirrors. The exposure spectrum of this tool was same as the ASML exposure tools. The monochromator of (2) reflectometer was UV – VUV reflectometer. At EUV lithography, out-of-band radiation (100 – 300 nm) of EUV source degrades image quality. Thus, optics and resist property of out-of-band region was essential to evaluate, for example EUV mask reflectivity, and EUV resist sensitivity. The monochromator specification was shown in Table 4. The EUV microscope (3) has Schwarzschild optics, which were fabricated with collaboration of Dr. Toyoda (Tohoku Univ.). The spatial resolution was quite high of less than 28 nm, which was equal to 7 nm at wafer printing size.

Table 4. VUV monochromator specification

Mount type	Collimate plane grating monochromator
Grating	Plane Grating (1,000 lines/mm)
Energy range	4 - 120 eV (UV ～ VUV)
Resolving power (E/ΔE)	～1000

IV. BL05

BL05 was constructed in response to a demand in the industry, which is enhancement of the analysis ability in the soft x-ray region with the development of nanotechnology. BL05 consists of two branch lines for use in the wide range from 50 eV to 4000 eV. BL05A and BL05B are designed to cover the energy range of 1000-4000 eV and 50-1000 eV, respectively. The incident beam from the bending magnet is provided for two branch lines through different windows of a mask. Therefore, these two branch lines can be employed simultaneously.

However, both beamlines had many problems and did not perform well enough for industrial and advanced analysis. In order to solve these problems, a drastic upgrade was started in 2020.

New BL05A

The constant-deviation monochromator consisting of a demagnifying spherical mirror and a varied-line-spacing plane grating (VLSPG), which can provide high resolution, simple wavelength scanning with fixed slits, was mounted on BL05A. The optical system consists of a first mirror (M0), a second mirror (M1), an entrance slit (S1), a pre-mirror (M2), and three kinds of plane grating (G), an exit slit (S2) and a focusing mirror (M3). The including angle of the monochromator is 175°. Two measurement chambers for XAFS and PES are prepared at the end station of BL05A. XAFS spectra in the total electron yield mode and partial fluorescence yield using a silicon drift detector can be measured in a high vacuum chamber. In addition, photoelectron spectra can be measured using spherical electron analyzer (VG Sienta, R3000) in an ultrahigh-vacuum chamber. The chambers can be replaced by each other. Table 6 shows the specification of the monochromator.

BL05B changed its name to BL05A due to the relocation to BL06, which will be described later.

Table 5. Monochromator specification

Monochromator	Varied-line-spacing plane grating monochromator
Grating	100 lines/mm, 300 lines /mm, 800 lines /mm
Energy range	50 - 1000 eV
Resolution	E/⊿E=3000

V. BL06 (BL05B and BL05C)

BL06 had been constructed for irradiation experiments such as photochemical reaction, SR-CVD, photo-etching, surface modification. BL06 for irradiation experiments was closed due to plans to build a new beamline for XAFS measurement. An X-ray mirror, Golovchenko-type double crystal monochromator, measurement systems and many other beamline components were relocated from former BL05A. The new BL06 will be equipped with two XAFS beamlines, one for XAFS in the 1-5 keV X-ray energy range (BL05B) and the other for XAFS in the 1-10 keV energy range (BL05C). BL05C was first set up to enable tender X-ray XAFS, and then upgraded to enable hard X-ray XAFS in 2022. A Rh-coated collimating mirror with incident/reflected angle of 0.28 degrees was selected for this beamline, which allows the photon energy of 1-10 keV. Table 6 shows the monochromator specification of BL05C.

Table 6. Monochromator specification of BL05C

Monochromator	Double crystal monochromator
Monochromator crystals	Beryl(10-10), KTP(011), quartz(10-10), InSb(111), Ge(111), Si(111), Si(220), Ge(220), Si(311), Ge(311)
Energy range	1 - 10 keV

VI. BL07

This beamline was designed for the development of new materials by SR technology. This beamline consists of two branch lines, which are provided with an incident beam from a 3-m-long undulator by switching the first mirror. One of them is a high photon-flux beamline with a multilayered-mirror monochromator for the study of SR-process (BL07A) and another is a high-resolution beamline with a varied line spacing grating monochromator for the evaluation of nano-structure characteristics by SR-spectroscopy (BL07B). The useful range of emitted photons from 50 to 800 eV is covered at both beamlines. The light source of BL07 is a 3-m length planar undulator, which consists of 29 sets of permanent magnets, a period length of which is 76 mm. The incident beam from the undulator is provided for two branch lines by translational switching of first mirror.

1) BL07A

The multilayered-mirror (MLM) monochromator, which has high reflectivity in the soft X-ray region, was installed at the BL07A. It consists of a switching mirror chamber, a slit chamber, a MLM monochromator, a filter chamber and a reaction chamber. To obtain a large photon flux, we decided to use only first mirror (switching mirror), M0, for focusing. The MLM monochromator is designed to cover an energy range of up to about 800 eV by combination of three kinds of mirror pairs with 4 kinds of filter. The flux deliver by this design is estimated to be between a maximum of 10^{17} photons/s at 95 eV and a minimum 2×10^{14} photons/s at 300 eV for a 500 mA ring current. Table 7 shows the summary of BL07A. In addition, X-ray fluorescence (XRF) apparatus using spherical varied line spacing grating was mounted at the downstream of irradiation chamber. The poly capillary was used to enhance beam-condensing efficiency. Measurement energy range was from 30 eV to 450 eV. This XRF apparatus was expected to utilize the chemical analysis on the light metals, Li and Be, and light elements, B, C and N.

Two novel vacuum chambers were installed in 2019 for the measurement of inverse Compton scattering of soft X-rays. One large chamber with a size of W1120×D820×H610 mm3 was set up 16.7 m downstream of the undulator center. A multi-layer mirror was placed on high precision auto-stages inside this chamber with cooling water circulation. The other chamber was installed 2.6 m upstream of the large mirror chamber, in order to monitor radiated and reflected X-rays.

Table 7. Summary of BL07A.

Energy range (eV)	Multilayer mirror					Filter	
	Material	Spacing	Thickness Ratio	Number of layers	ΔE/E	Material	Thickness
50-60	Mo/Si	20 nm	0.8	20	6.2 %	Al	100 nm
60-95						None	-
90-140	Mo/B_4C	11 nm	0.5	25	3.3 %		
140-194						Ag	100 nm
190-400	Ni/C	5 nm	0.5	60	2.5 %		
400-560						Cr	500 nm
550-800						Ni	500 nm

2) BL07B

The constant-deviation monochromator consisting of a demagnifying spherical mirror and varied line spacing plane grating (VLSPG), which can provide to high resolution, simple wavelength scanning with fixed slits, was mounted on BL07B. The optical system consists of a first mirror (M0), an entrance slit (S1), a pre-mirror (M1), and three kinds of plane grating (G), an exit slit (S2) and two focusing mirrors (M2 and M3). The monochromator is designed to cover the energy range 50-800 eV with three gratings, of which including angle are 168°. The VLSPG has been well known to obtain high resolution in extreme ultraviolet region by diminishing various kinds of aberration. The total resolving power about 3000 can be realized in the whole energy region. Table 8 shows the specification of the monochromator.

Table 8. Monochromator specification

Mount type	Hettrick-Underwood type
Grating G1, G2, G3	Plane VLS (600, 1200, 2400 l/mm)
Energy range	50-150 eV, 150 – 300 eV, 300-800 eV
Resolving power (E/ΔE)	～3000

VII. BL09

A purpose of this beamline is studies on a soft x-ray interferometry or a holographic exposure experiment with making use of highly brilliant and coherent photon beams radiated from 11 m long undulator in NewSUBARU.

BL09 consists of M0 mirror, M1 mirror, G grating and M2 mirror. M0 mirror is used for horizontal deflection and beam convergence, M1 is used for vertical beam convergence at the exit slit, and M2 is used for vertical deflection and beam convergence. A monochromator is constructed by M1 and a plane grating. The maximum acceptance of the undulator beam is 0.64 mrad in horizontal and 0.27 mrad in vertical. The acceptance can be restricted by 4-jaw slits equipped at upstream of the M0 mirror.

1) BL09A

BL09A beamline is used for material analysis: X-ray absorption spectroscopy (XAS) and X-ray photoelectron spectroscopy (XPS). In 2013, X-ray emission spectrometer (XES) was introduced at the end-station of the BL-09A. The energy range and resolving power of the XES system was designed to be about 50-600 eV and 1500, respectively. In 2021, a photoemission electron microscope system has been installed on BL09A.

2) BL09B

BL09B beamline branched from BL09 beamline for the usage of the EUV interference lithography for the evaluation of the exposure characteristics of EUV resist. Coherence length of 1 mm at the resist exposure position was achieved using BL09B beamline. And BL09C beamline branched from BL09B beamline for the usage of the thickness measurement of the carbon contamination originated to the resist outgassing during the EUV exposure. Table 9 shows the specification of the monochromator.

Table 9. Monochromator specification

Mount type	Monk-Gillieson type
Grating	Plane VLS (300, 900, 1200 l/mm)
Energy range	50 – 750 eV
Resolving power (E/ΔE)	～3000

VIII. BL10

BL10 is for EUV reflectometry and soft X-ray analysis. M0 mirror is used for horizontal deflection and beam convergence, M1 is used for vertical beam convergence at the exit slit, and M2 is used for vertical deflection and beam convergence. A monochromator is constructed by M1 and a plane grating. At the beginning, the multilayer reflectivity measurement was carried out at this beamline. The characteristics of this beamline and the result of the Mo/Si multilayer measurement are carried out for the development of the EUV- mask technology.

BL10 utilizes a monochromator of the varied-line-spacing plane grating (VLS-PGM). The line density of the monochromator in central region of the gratings were 600, 1800 and 2,400 lines/mm. The reflectometer has a two-axis vacuum goniometer. One axis carries the sample, which may be a mirror surface at the center of the reflectometer vacuum chamber (θ-motion). The other (φ-motion) carries the detector on a rotating arm. In addition, there are linear motions to translate the sample in two orthogonal directions (x, y). All motors are controlled by computer. The reflectivity result obtained at BL10 has a good agreement with that at LBNL. Table 10 shows the specification the monochromator.

The micro-CSM tool was adapted at the most downstream of the BL10 beamline for the EUV mask defect inspection with coherent-diffraction-imaging method. This too is very effective for the inspection of the actinic patterned mask with phase imaging.

A large reflectometer was installed in a branch line for large EUV optical component including EUV collector mirrors. The reflectometer has a sample stage with y, z, θ, φ, and Tilt axis, which can hold large optical elements with a maximum weight of 50 kg, a diameter of up to 800 mm, and a thickness of 250 mm. The entire sample surface is able to be measured.

Table 10. Monochromator specification

Mount type	Monk-Gillieson type
Grating	Plane VLS (600, 1800, 2400 l/mm)
Energy range	50 – 1,000 eV
Resolving power (E/ΔE)	～1000

IX. BL11

A beam line BL11 is constructed for exposure Hard X-ray Lithography (DXL) in the LIGA (German acronym for Lithographite Galvanoformung and Abformung) process. LIGA process, that utilizes a useful industrial application of SR, is one of the promising technologies for fabrication of extremely tall three-dimensional (3D) microstructures with a large aspect ratio. This process was invented at the Institut Fur Mikrostrukturtechnik (IMT) of the Karlstuhe Nuclear Center (KfK) in 1980. Microstructures with height of over a few hundred μm have been widely applied to various fields such as micro-mechanics, micro-optics, sensor and actuator technology, chemical, medical and biological engineering, and so on. This beam line was designed by the criteria; photon energy ranges from 2 keV to 8 keV, and a density of total irradiated photons $\geq 10^{11}$ photons/cm^2. The BL11 can provide the most suitable photon energy for microfabrication in X-ray lithography, while the BL2 is equipped for fabricating fine pattern submicron-scale structure and microstructure with high aspect ratio by selectivity of X-rays using movable mirror system. That is, LIGA process in NewSUBARU can provide the best 3D microfabrication because the BL11 and BL2 are complementary. The beamline BL11 is consisting of an absorber chamber, a first-mirror chamber (M1), a 4-way slit chamber, a Be and polyimide window chamber, and an exposure chamber. The horizontal angle of the outgoing SR could be obtained up to 17.8 mrad, providing a beam spot size on the exposure stage $\geq 80 \times 10$ mm^2. The micron-scale structure with high aspect ratio will be achieved using the toroidal typed mirror M1 which can produce a parallel collimated beam of X-rays. In addition, the homogeneity of the beam is excellently controlled by a novel adding system.

Using the precision stage in the exposure chamber, the flexibility for the shaped and functions of microstructure will be enlarged by achieving 3D microfabrication process using multi step exposure at various configuration between x-ray mask and substrates. The exposure area of 200 mm × 200 mm is brought to fruition. In order to decrease the heat load of sample substrate suffered during SR irradiation, helium introduction and substrate cooling system were also equipped. The specification of the LIGA exposure system is listed in Table 11.

Table 11. Specification of the LIGA exposure system

Exposure method	Proximity exposure
Wafer size	8 inch
Exposure area	200 mm(H)×200 mm(V)
Exposure environment	< 1atm (He-gas)

Establishment of Research Center for Advanced Synchrotron Radiation Analysis

In order to respond to diverse analysis needs from industries, it is necessary to advance technological development for analyzing beamlines (BLs) of NewSUBARU SR facility to advance integrated and strategic development of analyzing technology. For this reason, the Research Center for Advanced SR Analysis was launched in August 2016. As an organization crossing in university courses, this center is consulted and administered by all members of the LASTI related to analysis, and in collaboration with the SR Nanotechnology Center of Hyogo Prefecture, a wide range of energy from hard X-rays to soft X-rays. We aim to respond to various analysis needs of the area on a one-stop basis.

Acknowledgement

We would like to thank all the staff who work at NewSUBARU synchrotron radiation research facility for their help to describe the update details of the beamlines.

Electron accelerators at NewSUBARU

Satoshi Hashimoto

Laboratory of Advanced Science and Technology for Industry (LASTI), University of Hyogo

Abstract

We report the operational status of two accelerators, the 1.0 GeV electron linear accelerator and the 1.5GeV electron storage ring, at the NewSUBARU synchrotron light facility in FY2022. The report covers a wide range of topics, including research and development of accelerator systems, improvements in beam performance, and aging equipment. We will also introduce free electron laser experiments performed at beamline BL01. In addition, the development and application of Laser Compton Scattered gamma-ray sources will be covered.

1. Introduction

The NewSUBARU synchrotron light facility[1, 2] houses a 1.5 GeV electron storage ring, making it the largest accelerator among universities in Japan. Over the course of more than 25 years, this facility has been utilized not only for fundamental research but also for student education and industrial applications, leveraging its high-quality soft X-rays. Synchrotron radiation science and accelerator science stand out as major focal points of our university.

In FY2020, we successfully constructed a new 1.0 GeV linac dedicated to complementing the NewSUBARU ring. This achievement was made possible with assistance from the SPring-8 accelerator staff[3, 4]. Since FY2022, the storage ring has been in operation with the integration of the new injector[5].

2. Overview of electron accelerators

2.1. 1.0 GeV electron linear accelerator

Figure 1 illustrates the comprehensive configuration of the injection linac, while Table 1 provides an overview of the linear accelerator's performance. An electron beam, produced through a thermal-cathode RF electron gun, is accelerated to 1.0 GeV via a series of stages involving a buncher cavity, S-band, and C-band acceleration tubes.

Table 1. Performance of the new injector linac.

	Require	Measurement
Beam Energy	1.0 GeV	1.0 GeV
Bunch charge	100 pC	100 pC
Normalized emittance	<10 mm-mrad	<10 mm-mrad
Energy spread	<±0.5%	0.1% (FWHM)
Energy stability	-	0.4% (STD)
Bunch length	5ps (FWHM)	<1ps (FWHM)
Injection efficiency	>90%	>90%

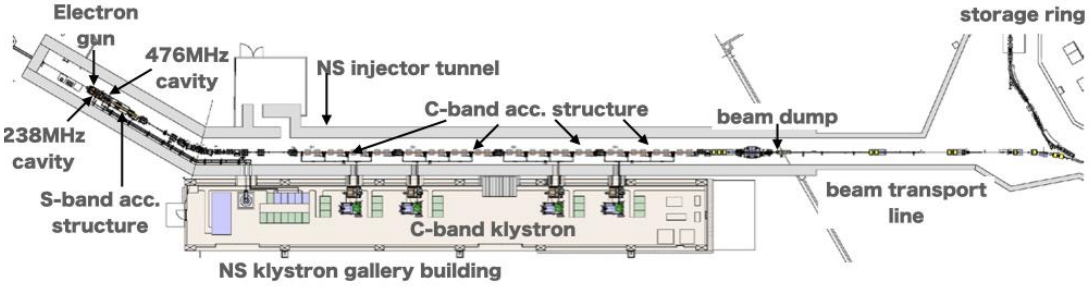

Figure 1. Layout of the new 1.0 GeV electron linear accelerator for the NewSUBARU storage ring.

2.2. 1.5 GeV electron storage ring

The overall arrangement of the ring is depicted in Figure 2. The ring comprises 6 Double-Bend Achromat (DBA) cells featuring inverse bending magnets. Each cell is separated by 6 straight sections, which serve as locations for an injection septum, an accelerating RF cavity, and three undulators.

Two long straight sections of 15 m each, one with a 10.8 m long undulator (LU) and the other with Laser Compton Scattered (LCS) gamma-ray generation and Free Electron Laser (FEL) serves a dual purpose. Our FEL generates ultrashort pulses. Details of the main parameters of the ring are shown in Table 2. In particular, a key feature of this ring is the adjustable stored beam energy in the range of 0.5 to 1.5 GeV.

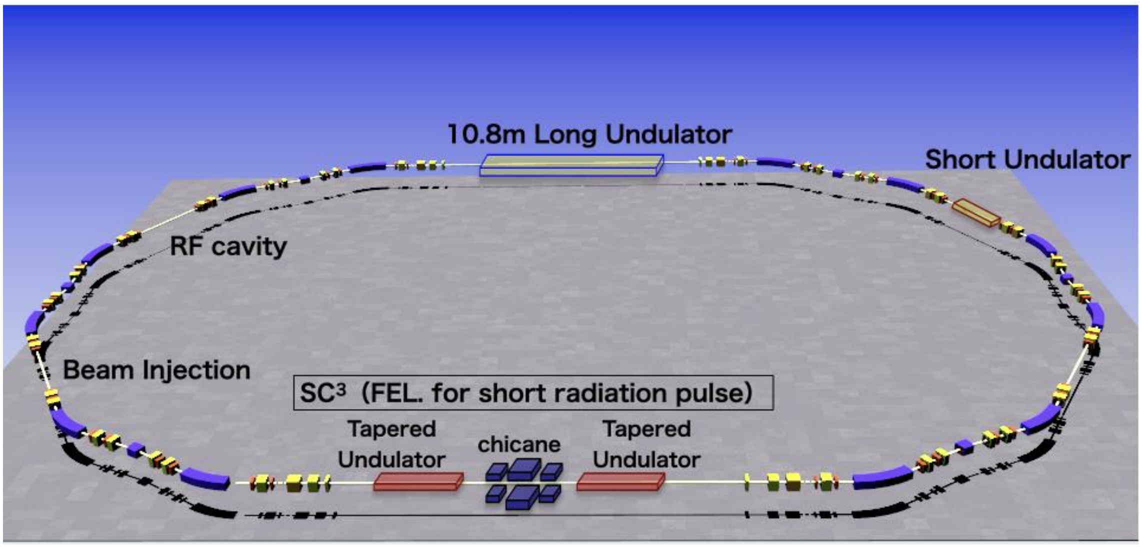

Figure 2. General layout of the NewSUBARU storage ring. Electron beams are injected from the newly-constructed 1.0 GeV linac dedicated to the ring.

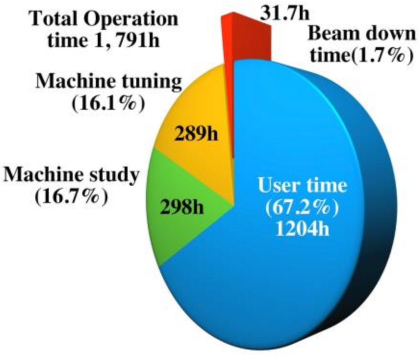

Figure 3. Operation time of NewSUBARU in FY2022.

Table 2. Main parameters of the NewSUBARU storage ting

Circumference	118.73 m
Lattice	DBA + inv. Bends
Injection beam energy	0.5 – 1.0 GeV
Stored beam energy	0.5 – 1.5 GeV
Mac. Stored current	500 mA
Number of bends	12
Radius of curvature	3.217 m
RF frequency	499.955 MHz
Harmonic number	198
Betatron tunes	6.29(H), 2.22 (V)
Number of IDs	3
Radiation loss per turn (@1.0GeV)	33.4 keV
Energy acceptance	±0.85%
Injection repetition rate	1 Hz

3. Operation Status in FY2022

Our facility provides two different modes of operation for user time: 1.0 GeV top-up mode and 1.5 GeV current decay mode. Normal business hours are from 9:00 am to 9:00 pm on weekdays. The weekly schedule designates Mondays for machine research and development (R&D) activities. Tuesday is allocated 1.5 GeV of user time, and Wednesday and Thursday are allocated an additional 1.0 GeV of user time. Friday is specified as 1.0 GeV or 1.5 GeV user time.

Until FY2020, weekday evenings and weekends were available for ancillary machine research and additional user time utilizing special modes such as single-bunch operation and operation with arbitrary electron beam energy. However, from 2021, accelerator operation has been limited to the hours from 9:00 am to 9:00 pm on weekdays. This change is due to outsourcing the operation of the accelerator to a private company.

Figure 3 shows the distribution of machine uptime in FY2022. The cumulative operating time of the machine during this period was 1,791 hours, equivalent to 90% of the operating time in FY2021 excluding beam down time. The term "beam downtime" includes not only periods of mechanical failure, but also beam abort due to issues such as beam instability or mishandling. The total downtime experienced throughout

FY2022 was approximately 32 hours, or 1.7% of total operational hours. Additionally, 587 hours were spent on tuning and machine study activities.

In FY2022, there was concern about a significant reduction in annual operating hours due to soaring electricity costs. However, due to the implementation of subsequent measures, the user time decreased by only 2% compared to the previous year.

- Bringing forward user usage end time (from 21:00 to 19:00)
- Cost reduction by postponing regular inspections of accelerators
- Subsidy from Hyogo Prefecture

4. Machine Trouble

The beam down time in FY2022 was 57 hours. Typical troubles are as follows.

4.1. Failure of additional power supply for inverse bending magnets

In NewSUBARU, the bending magnet power supply is connected in series to the bending magnets and the inverse bending magnets. However, when accelerating the beam, the current flowing through the inverse-bending magnets is insufficient, so an auxiliary power supply for the inverse-bending magnet is connected in parallel. After June 2022, this auxiliary power supply failed, making it impossible to operate at 1.5GeV, and operating at 1.23GeV during acceleration.

Figure 4. Additional Power supply for inverse bending magnets.

4.2. Failure of a power supply for bending magnets

Oscillation of the output current of the bending magnet power supply had occurred about once a year until then, but from April to May 2023, current oscillation occurred frequently and beam abort occurred eight times. It was presumed that it was due to aging, but since the specific cause could not be identified, measures such as cooling the board part inside the power supply with a spot cooler were taken. Oscillation has not occurred since the end of May, but measures to prevent recurrence and replacement of the power supply are being considered.

4.3. Sudden blackout of the power supply of the bending magnet in the beam transport line

About once a year, the power supply of the bending magnet installed in the beam transport system from the injector exit to the ring accelerator suddenly dropped to 0A during operation. In 2022, such a phenomenon

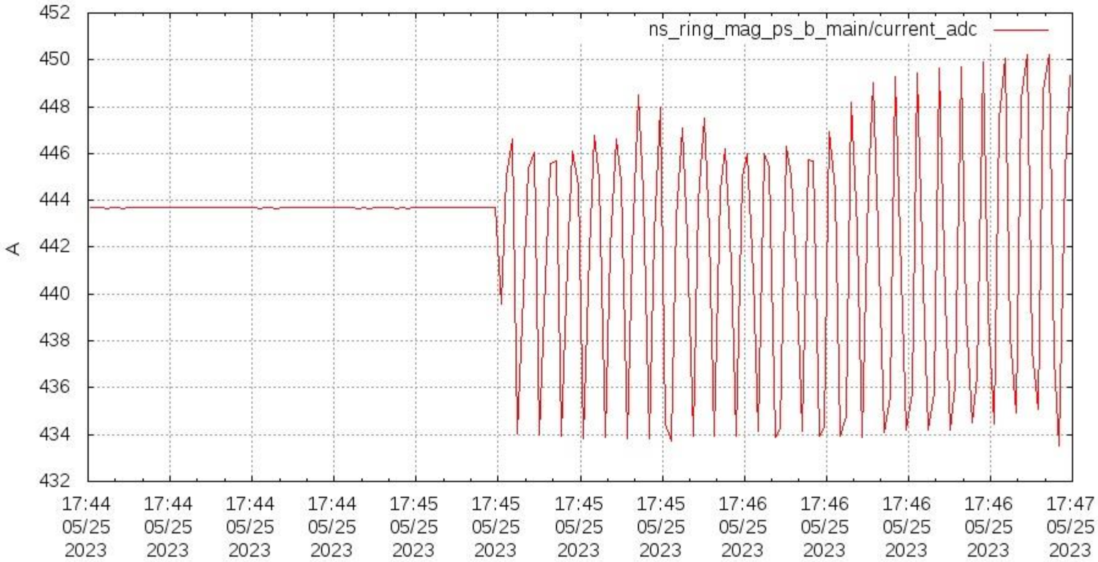

Figure 5. Oscillation of output current of the power supply for bending magnets.

occurred 10 times. There was no abnormality in the power supply inspection, but after replacing the I/O board for remote control of the power supply, such a phenomenon began to occur on rare occasions.

4.4. Failure of magnet power supply for injector

In 2022, three injector electromagnet power supplies failed. Two of them were discovered during tuning of the accelerator and immediately replaced with spare parts and restored. The failure of the remaining one was discovered before the beam ejection in the morning and was replaced with a spare in about 30 minutes, so it is not included in the beam outage time. Of the three failures, two were due to power supply fan failures and one was due to power communication board failures. Regarding the power supply that I had been using for many years, I replaced all the fans after receiving this trouble.

4.5. Vacuum trouble at the beamline BL02

In June 2022, the gate valve between beamline BL02 and the ring accelerator opened due to user error, despite the poor vacuum in the beamline. As a result, a beam abort occurred due to deterioration of the vacuum level of the accelerator. Since the Fast-Closing valve on the beamline side and the gate valve between the accelerator cells automatically closed immediately, the decrease in the degree of vacuum on the accelerator side was minimized. A TSP flash restored the vacuum and he resumed beam operation 2 hours after shutting down the beam.

4.6. Injector RF reflection multi-occurrence

Since mid-2022, two of the four C-band accelerator tubes used in injector linacs have increased RF reflections when boosting to set voltage. It took more than an hour before the start of beam injection in the morning, and the start of user time was sometimes delayed. After July 2022, we lowered the ring energy from 0.98 GeV to 0.95 GeV. This lowered the C-band setting voltage and reduced the frequency of the reflections, but did not completely eliminate the reflections. We are currently optimizing the output waveform of the SLED to prevent reflection, and plan to start operation in the fall of 2023.

5. Machine R&D

5.1. SC3 project (mono-cycle FEL)

We are actively working on the SC3 (Slippage-Controlled Coherent Radiation by Chirped Micro-bunching) project in collaboration with the RIKEN Synchrotron Radiation Center, the Graduate School of Materials Science, University of Hyogo, and LASTI. This effort includes experimental verification of generating ultra short radiation pulses spanning just a few wavelengths. These were achieved at the NewSUBARU facility through the use of arbitrary taper undulators[6], magnetic chicanes, and chirp seed lasers[7]. During FY2022, we

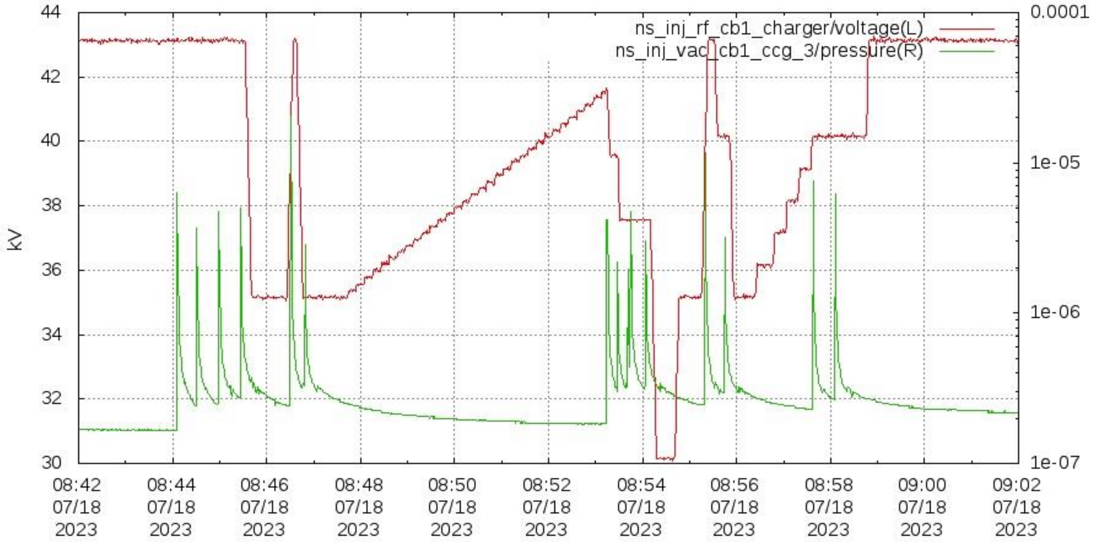

Figure 6. RF power of C-babd klystron and vacuum pressure in accelerating tube.

achieved an important milestone by successfully generating microbunching within a single-electron bunch and subsequently observing coherent radiation[8].

5.2. LCS gamma-ray: development of light source and its applications

BL01, a dedicated light source research and development (R&D) beamline, has served as a platform for various studies utilizing laser Compton scattered (LCS) gamma rays[9-17]. As shown in Figures 7 and 8, this process involves the scattering of incident laser photons in the visible or infrared by high-energy electrons, resulting in the emission of high-energy photons within the gamma-ray spectrum. Figure 9 shows a representative spectrum of LCS gamma photons, showing the results of using a 532 nm wavelength laser in combination with a 1.0 GeV electron beam. Our commitment to enhancing and exploiting gamma-ray sources remains unchanged.

In FY2022, we performed optimization calculations for the incident laser optical system with the aim of increasing the intensity of gamma rays. Optimization of parameters such as waist position and beam diameter of the 532 nm laser wavelength achieved significant enhancement, increasing the measured gamma-ray intensity by about 30%[9].

5.3. Application of machine learning to beam diagnostics

We used machine learning to analyze the frequency spectrum waveforms of electron beam betatron oscillations in real-time[18,19]. By learning in advance using several thousand waveform data, horizontal and vertical peak frequencies can be accurately evaluated from noisy waveforms as well as their reliability. Offline analysis by machine learning was successful, so next is a test using a real beam.

5.4. Other accelerator study

In collaboration with KEK, we initiated the development of a novel beam monitor capable of assessing the tilt of the electron bunch through the electrical processing of the BPM (Beam Position Monitor) signal[20].

Accelerator tuning was performed to facilitate beam injection and accumulation at various low energies. As a result of this effort, we have successfully implanted and accumulated beams in the range of 1.0 to 0.65 GeV while maintaining high injection efficiency and beam intensity. Achieving top-up operation at these versatile energies is important for photon energy tuning of free electron laser (FEL) and laser Compton scattered (LCS) gamma-rays, increasing their applicability and practicality.

6. Summary

NewSUBARU's 1.0-GeV injector accelerator and storage ring in FY2022 went smoothly despite some equipment troubles. We have a lot of experience in operating the new injector. The stable supply of high-quality electron beams from the injector has improved the performance of the storage ring.

Currently, it is difficult to secure the number of operating days in FY2023 due to soaring electricity rates. Nonetheless, our commitment to advancing accelerator capabilities, pioneering new light sources, and expanding industrial support remains unwavering. Our main goal is to be able to consistently provide

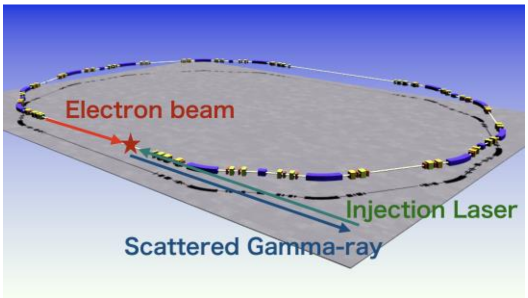

Figure 7. General scheme of Laser Compton Scattering (LCS) gamma-ray generation at BL01.

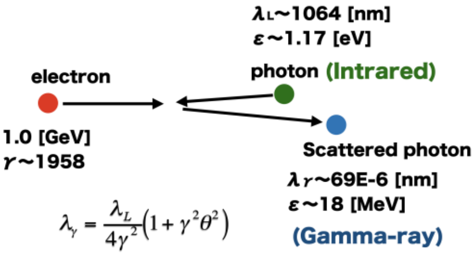

Figure 8. General scheme of LCS gamma-ray generation.

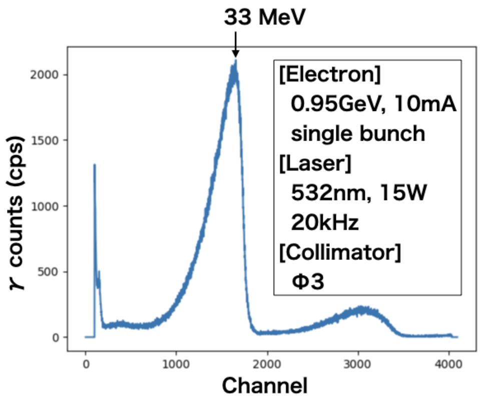

Figire 9. Typical measured LCS gamma-ray spectrum at BL01.

high-quality synchrotron radiation despite these challenges.

Acknowledgement

We extend our heartfelt appreciation to the accelerator personnel at RIKEN SPring-8 center, JASRI, and SES for their invaluable collaboration in facilitating the operation of the injector linac. We also wish to acknowledge Dr. Y. Minagawa, Mr. K. Kajimoto, Mr. H. Hirayama, Mr. S. Nakata, and Mr. A. Nakamura of SES for their dedicated machine operation efforts. Furthermore, we express our profound gratitude to Mr. T. Ushizawa and Dr. T. Sakurai of JASRI for their contributions towards maintaining stable accelerator operations. A special note of thanks goes to Dr. Fujii of Kansai Medical University for his noteworthy contributions to machine learning research. Lastly, our deepest appreciation is reserved for Prof. Miyamoto of Osaka University, whose leadership played a pivotal role in overseeing the construction of BL01.

References

[1] A. Ando, S. Amano, S. Hashimoto, H. Kinosita, S. Miyamoto, T. Mochizuki, M. Niibe, Y. Shoji, M. Terasawa, T. Watanabe and N. Kumagai: *Journal of Synchrotron Radiation* **5**(3) 342-344 (1998).

[2] http://www.lasti.u-hyogo.ac.jp/NS-en

[3] S. Hashimoto: *LASTI Annual Report 2021,* **23**, p.1-5 (2022).

[4] T. Inagaki, T. Fukui, T. Hara, T. Hiraiwa, H. Maesaka, H. Tanaka, T. Asaka, H. Dewa, N. Hosoda, E. Iwai, C. Kondo, T. Magome, T. Ohshima, T. Sakurai, K. Yanagida, S. Inoue, K. Kajimoto, Y. Minagawa, S. Nakata, T. Seno, H. Sumitomo, R. Takesako, S. Tanaka, R. Yamamoto, M. Yoshioka and S. Hashimoto: *International Particle Accelerator Cpnference, IPAC2021, WEPAB039* (2021).

[5] S. Hashimoto, H. Fujii, T. Sakurai, T. Ushizawa, Y. Minagawa, K. Kajimoto, S. Nakata and H. Hirayama: *Proceedings of 19th Annual Meeting of Particle Accelerator Society of Japan*, p.1119 (2022).

[6] T. Tanaka, Y. Kida, R. Kinjo, T. Togashi, H. Tomizawa, S. Hashimoto, S. Miyamoto, S. Okabe and Y. Tanaka: *Journal of Synchrotron Radiation* **28**(2) 404-409 (2021).

[7] Y. Kida, S. Hashimoto, S. Miyamoto, T. Togashi, H. Tomizawa, S. Okabe, A. Gocho, K. Kaneshima, Y. Tanaka and T. Tanaka: *Proceedings of 19th Annual Meeting of Particle Accelerator Society of Japan*, p.75 (2022).

[8] T. Tanaka, Y. Kida, S. Hashimoto, S. Miyamoto, T. Togashi, H. Tomizawa, A. Gocho, K. Kaneshima and Y. Tanaka: *Phy. Rev. Lett., acceptted* (2023).

[9] S. Hashimoto and H. Hirakawa: *LASTI Annual Report 2022,* **24** (2023).

[10] D. Filipescu, I. Gheorghe, K. Stopani, S. Belyshev, S. Hashimoto, S. Miyamoto and H. Utsunomiya: *Nuclear Instruments and Methods in Physics Research Section A: Accelerators, Spectrometers, Detectors and Associated Equipment,* **1047**, p.167885 (2022).

[11] T. Ari-Izumi, I. Gheorghe, D. Filipescu, S. Hashimoto, S. Miyamoto. H. Utsunomiya, *J. Instrum.* **18** T06005 (2023).

[12] T. Sanami, T. Tran, T. Nguyen, H. Yamazaki, T. Itoga, Y. Kirihara, Y. Namito, H. Nakashima, S. Miyamoto, S. Hashimoto and Y. Asano: *Proceedings of 19th Annual Meeting of Particle Accelerator Society of Japan*, p.70 (2022).

[13] T. Sanami, T. K. Tran, H. Yamazaki, T. Itoga, Y. Kirihara, Y. Namito, Y. Sakaki, S. Miyamoto and Y. Asano: *15th international conference on nuclear data for science and technology* (ND2022), EPJ Web of Conferences **284**, 01047 (2023).

[14] T. K. Tran, Y. Sakaki, T. Sanami, H. Yamazaki, Y. Namito, T. Itoga, Y. Kirihara, S. Miyamoto and Y. Asano: *15th international conference on nuclear data for science and technology* (ND2022), EPJ Web of Conferences **284**, 01048 (2023).

[15] T. K. Tuyet, T. Sanami, H and Yamazaki: *14th International Conference on Radiation Shielding and 21st Topical Meeting of the Radiation Protection and Shielding Division*, Seattle, WA September 25–29 (2022).

[16] T. Sanami *et al.*: *LASTI Annual Report 2022,* **24** (2023).

[17] M. Omer *et al.*: *LASTI Annual Report 2022,* **24** (2023).

[18] H. Fujii, K. Watanabe and S. Hashimoto: *Proceedings of 19th Annual Meeting of Particle Accelerator Society of Japan*, p.557 (2022).

[19] H. Fujii *et al.*, *LASTI Annual Report 2022,* **24** (2023).

[20] T. Nakamura *et al.*: *Proceedings of 20th Annual Meeting of Particle Accelerator Society of Japan*, (2023).

Development of Betatron Tune Correction System by Deep Learning Using Loss Function with Quality Filter

Hitoshi Fujii[1], Kousuke Hirose[2], and Satoshi Hashimoto[1]

[1]*Laboratory of Advanced Science and Technology for Industry (LASTI), University of Hyogo*
[2]*Faculty of Engineering, University of Hyogo*

Abstract

In the NewSUBARU synchrotron light facility, real-time observations and analyzes of betatron oscillation spectra are performed for tune correction. Here, the observed spectra are sometimes obscured due to various reasons, and wrong betatron frequencies are estimated from such spectra, in which case the tune correction fails. To avoid this, current tune correction systems use complex algorithms with many parameters to be manually adjusted. However, this system cannot handle various operation modes in NewSUBARU, and when updating devices such as electromagnets, it is necessary to update the parameters of the system from scratch. Therefore, we proposed deep learning using "loss function with quality filter" and developed a new spectral analysis method that is more flexible and accurate than the current systems.

1. Introduction

The electron beam oscillates slightly in the horizontal and vertical directions from the design orbit in the storage ring, which is called betatron oscillation. The number of the oscillations per round of the ring is called "tune". The problem in stabilizing the electron beam is not the betatron oscillation itself, but the tune value. For example, if the tune is an integer, it means that the electron beam rounds exactly the same trajectory every round. In this case, similar to resonance of pendulum, if there is even a small extra magnetic field somewhere in the ring, the electron beam will be affected by the external force in the same direction every round and the amplitude of the betatron oscillation reaches the vacuum chamber. As a result, the lifetime of the electron beam is reduced or, in the worst case, the beam is completely lost (the same problem occurs when the decimal part of the tune is described by a relatively simple fraction such as 1/2, 1/3, etc.). It is impossible to completely remove the extra magnetic field in the storage ring.

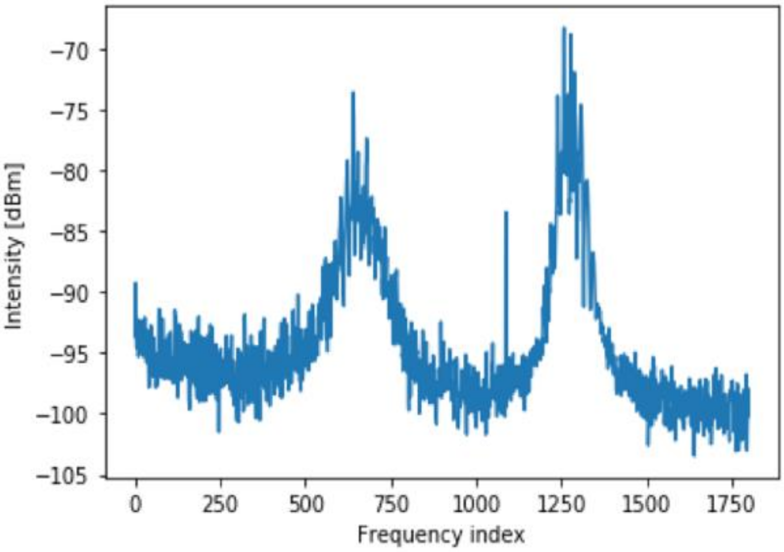

Figure 1. An example of betatron oscillation spectrum. The vertical axis is signal intensity and the horizontal axis is frequency index; frequency is represented by the index number of the array for simplification.

Therefore, in order to stabilize the electron beam, a tune correction system is required to constantly monitor the tune value (that can change) and maintain (previously researched) optimal values.

Figure 1 shows an example of a betatron oscillation spectrum. The two large peaks are the horizontal and vertical components of betatron oscillations, respectively. Tune values are estimated by performing a peak extraction from the spectrum. At this time, it is not always possible to obtain a clear spectrum as shown in Fig. 1, and the quality of spectrum data may deteriorate for some reason (for example, at the time of electron beam injection, acceleration, deceleration, etc.). In such cases, a wrong tune value may be estimated and the system performs a wrong correction, resulting in the loss of the electron beam. Therefore, before performing the tune correction, it is necessary to judge whether the spectrum is sufficiently reliable (high quality) to be used for the correction. In the current correction system, the judgement is made by a complicated algorithm with many thresholds such as the height, half-width and approximate position of the spectral peak. In the system, however, when the outline of the observed spectra changes significantly due to changes in driving conditions or equipment upgrades, all parameters of the system must be readjusted manually.

In this study, we proposed a “loss function with quality filter” for deep learning and developed a more flexible spectral analysis method. With this method, it is possible to simultaneously judge the quality of spectra that can be used for correction and estimate the tune values (peak positions of spectra) by using a single network. There are almost no parameters that need to be manually adjusted.

2. Method

2.1. Definition of Loss Function

Training a network requires a large amount of teacher data which is a set of features (descriptors) and target variables (correct answer values). In many cases, there is only one target variable, but there may be multiple targets. In our case, there are three targets in total: the quality value (reliability or clarity) and the peak positions for horizontal and vertical component of the spectra. The features are the spectral data itself. The spectral data can be collected easily, and all the collected spectra are annotated, i.e., given correct labels of quality values and peak positions[1,2]. The loss function with quality filter is defined as follows:

$$L(t_q, y_q, \boldsymbol{t}, \boldsymbol{y}) = l_q(t_q, y_q) + \alpha t_q l(\boldsymbol{t}, \boldsymbol{y}), \tag{1}$$

$$l_q(t_q, y_q) = -t_q \ln y_q - (1 - t_q) \ln(1 - y_q), \tag{2}$$

where $t_q \in \{0,1\}$ is the correct value of the quality (a binary value of 0: low or 1: high). $y_q \in [0,1]$ is a quality value estimate by network. $l_q(t_q, y_q)$ is called the binary cross-entropy error and is often used as a loss function for binary classification problems. In the present case, $l(\boldsymbol{t}, \boldsymbol{y})$ is appropriate to use

$$l(\boldsymbol{t}, \boldsymbol{y}) = (t_x - y_x)^2 + (t_y - y_y)^2. \tag{3}$$

This is the sum of the residual sum of squares which is used as a loss function of regression problems with multiple target variables. t_x and t_y are the peak positions of the horizontal and vertical components, respectively. y_x and y_y are the estimated values of t_x and t_y respectively. α is a hyperparameter to balance the magnitude of l_q and l. Here, the point is that the second term of L is multiplied by t_q. This works as a filter, i.e., skips learning about $\boldsymbol{t}$ in the case of low-quality ($t_q = 0$) data. As a result, if the quality of the data is so low that it is impossible to annotate $\boldsymbol{t}$ even with the human eye (only $t_q = 0$ is known), it is enough to put dummy values in $\boldsymbol{t}$.

2.2. Definition of Network

Figure 2 shows the network configuration. The basic structure is the same as AlexNet[3] proposed for image recognition, but one-dimensional convolutional layers are used. In addition, the output layer is branched into two, one related to prediction of quality and the other related to prediction of peak positions. In other words, the network for quality prediction is also used for peak position prediction partially. This is more

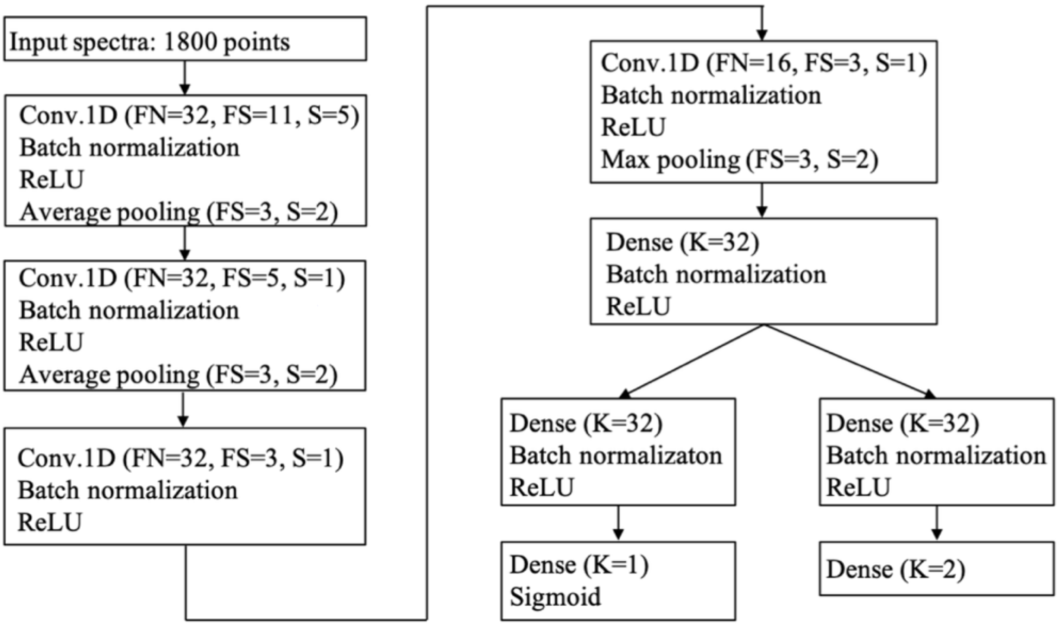

Figure 2. Illustration of the architecture of our network. FN, FS, and S mean the number of filters, filter size, and stride size, respectively. The left-hand side of the output layer gives an estimation value for certainty and the right-hand side gives estimation values for peak positions.

efficient than building two completely independent networks. Also, in general, branching the output layer can be expected to suppress over-learning.

3. Results and Discussion

As a result of testing the above network using actual spectrum data, the success rate for the spectra with quality$t_q = 0$ (ratio of correctly judging the low values as low) was 0.900, and the success rate for the spectra with quality at $t_q = 1$ (ratio of correctly judging the high values as high) was 0.969. The prediction accuracy (RMSE) of the peak positions for the spectra with $t_q = 1$ was 7.189 for the horizontal component and 2.482 for the vertical component. This means that the prediction errors of the peak positions are about 1 % in the given range, and it can be seen that the peaks can be extracted with considerable accuracy. The details of the results are in reference 1.

4. Conclusion

We developed a new spectra analysis method by using deep learning with loss function with quality filter. This method shows that even with a relatively shallow network, it is possible to simultaneously predict the quality and peak positions from spectra with high accuracy. By incorporating this network into the current tune-correction system, it is expected that a more flexible system can be constructed.

References

[1] H. Fujii, K. Watanabe, and S. Hashimoto: *PASJ2022*, WEP019 (2022).
[2] https://github.com/Hitoshi-FUJII/GFit.
[3] A. Krizhevsky, I. Sutskever, and G. E. Hinton: *Communication of the ACM* **60** (6), 84–90 (2017).

Increased LCS γ-ray flux by optimizing laser optics at BL01

Satoshi Hashimoto and Haruto Hirakawa

Laboratory of Advanced Science and Technology for Industry (LASTI), University of Hyogo

Abstract

The NewSUBARU light source R&D beamline BL01 is one of the few Laser Compton Scattered (LCS) gamma-ray facilities in the world, capable of producing gamma-rays of excellent performance. Increased gamma-ray intensity is important for users. By optimizing the laser optical system, we succeeded in increasing the number of gamma-ray photons by about 30%.

1. Introduction

LCS gamma-rays have excellent properties such as energy tunability, high directivity, quasi-monochromaticity, and polarization[1,2]. BL01 generates gamma-rays by colliding incident laser photons head-on with relativistic electrons orbiting within a storage ring. For users[3-8], increasing the intensity of gamma-rays (the number of photons) has major benefits, such as shortening experiment time and improving the signal-to-noise ratio. One way to solve this problem is to optimize the laser optics. By focusing the laser beam to a small radius at the right location, efficient collisions between electrons and laser photons occur. Figure 1 shows the profiles of three lasers that have been in use for many years. It can be seen that the laser waist size is large due to long distance transmission and the waist position of the laser does not match that of the electron beam. We have optimized the optics of the Talon laser (532 nm) and succeeded in improving the measured gamma-ray intensity by about 30%. This report describes the details.

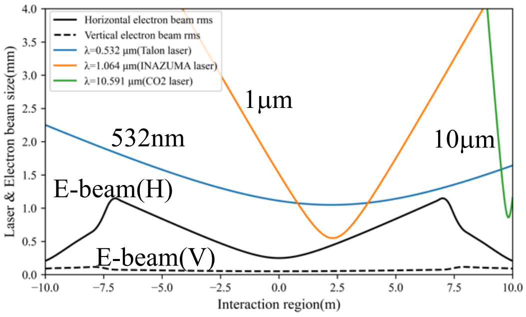

Figure 1. Horizontal and vertical elcctron beam radius and beam radius of three lasers used at BL01.

2. Optimization of laser optics

2.1. Optimization calculation

Optimization calculations for laser optics were performed using one divergent lens and one convergent lens in the tunnel. For calculations, we used a Python code created by Hirakawa based on Gaussian optical theory. The beam portion exceeding the aperture of the viewport or optical element on the optical path was treated as a loss. Table 1 and Fig. 2 show the results of minimizing the beam waist and designing the waist position to be in the center of the straight section. Before optimization (Fig.2-a), the beam waist was relatively large, and the waist position was approximately 2.3 m away from the center of the straight section. As shown in Fig.2-b, the beam waist is narrowed down by optimization using two lenses, and the waist position coincides with the center of the straight section.

2.2. Estimation of gamma-ray flux

The number of LCS gamma-ray photons N_γ is expressed by the following equation[2].

$$N_\gamma = c(1+\beta)\frac{I}{e\upsilon}\frac{P}{E_p c}\sigma_{tot}\int_z L(z)dz \tag{1}$$

where c is the speed of light, β is the normalized electron velocity, I the stored current value, e the elementary charge, υ the electron velocity, P the incident laser power, E_p the incident photon energy, and σ_{tot} the scattering cross section. L(z) represents the degree of overlap between the incident laser and the electron beam, and is expressed by the following equation[2].

$$L(z) = \frac{1}{2\pi\sqrt{\sigma_x(z)^2 + w(z)^2}\sqrt{\sigma_y(z)^2 + w(z)^2}} \qquad (2)$$

where $\sigma_x(z)$ and $\sigma_y(z)$ are the horizontal and vertical sizes of the electron beam, and $w(z)$ the beam size of the incident laser. The effect of laser optics concerns only the integral term in eq. (2). Fig. 3 shows the laser radius and L function in the straight section of the storage ring. The gamma-ray intensity can be evaluated using the value obtained by integrating the L function over the laser pulse width (30 ns) centered on the position where the L function was maximum. The calculation results showed that by optimizing the optics, the gamma-ray intensity could be approximately doubled.

Table 1(a). Talon laser optics parameter before optimization.

Lens 1	type	convergent
	Focal length [m]	5
	Position [m]	7.152
Laser waist [mm]		1.04
Laser waist pos.[m]		20.05
E-beam waist pos. [m]		22.41

Table 1(b). Talon laser optics parameter after optimization.

Lens 1	type	divergent
	Focal length [m]	-0.2
	Position [m]	6.84
Lens 2	type	convergent
	Focal length [m]	0.5
	Position [m]	7.144
Laser waist [mm]		0.46
Laser waist pos.[m]		22.03
E-beam waist pos. [m]		22.41

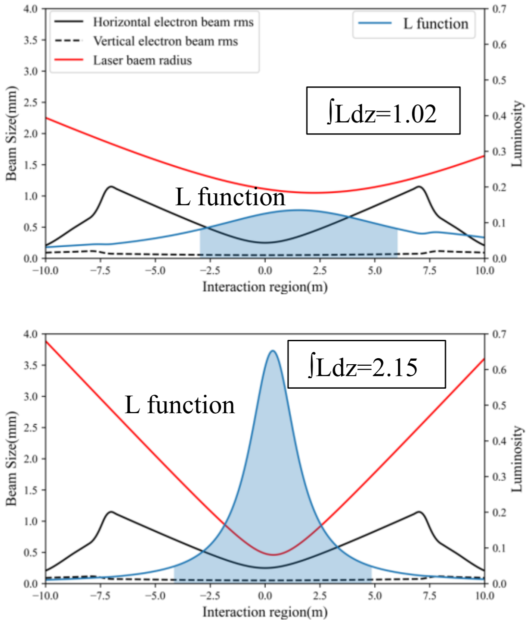

Figure 3. Overlap function before (upper) and after (lower) optimization of laser optics.

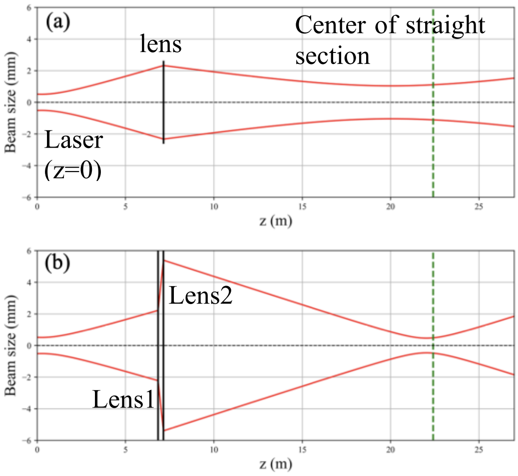

Figure 2. Laser beam radius (a) before and (b) after the optics optimization. Laser wavelength is 532 nm. Laser is located at z=0. Dotted line denotes the center of the straighr section og the ring.

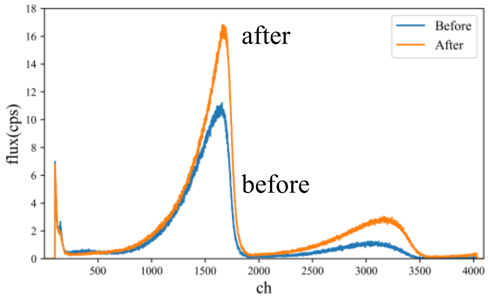

Figure 4. Measured gamma-ray spectra bedore (blue) and after (orange) the optics optimizarion.

Table 2. Typical parameters at γ-ray measurement

[Electron]	0.95 GeV, 10 mA, Sigle bunch
[Laser]	532 nm, 15 W, 20 kHz
[Collimator]	φ3 mm

3. Measurement of increased gamma-ray flux

The number of gamma-ray photons per second was measured using a Ge detector and a multichannel analyzer. Typical parameters during measurement are shown in Table 2. Fig. 4 shows the measured spectra of gamma-rays before and after the optimization of the optical system. It can be seen that the number of gamma photons is improved by about 30% despite the same stored current and laser power.

The measured gamma-ray photon increase was smaller than the calculated value. This may be due to insufficient precision in laser beam alignment. In calculating the L function, it is assumed that the electron beam orbit and the incident laser optical axis are perfectly aligned. However, in reality it is very difficult to match the two beam axes. To solve this problem, we are preparing to remotely control the optical elements inside the shield tunnel, which have been difficult to adjust.

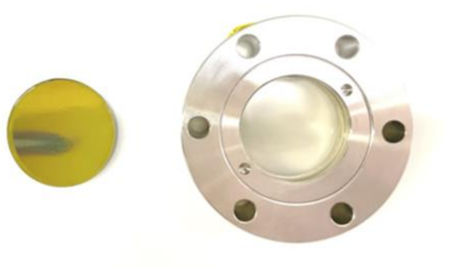

Figure 5. Damaged Ag-coat Si mirror in vacuum (left) and vaciim viewport (right) for Talon laser.

Another cause is damage to the silver-coated mirror in vacuum and the vacuum viewport for laser incidence due to synchrotron radiation. Figure 5 shows the Talon laser mirror and vacuum window that were replaced in August 2023. Damage caused by synchrotron radiation is clearly visible on the Si mirror surface. Clouding was also observed at the same location inside the vacuum window. The data shown in Fig. 4 was measured with the damage shown in Fig. 5. The experiment, which will resume this fall, will use new optical elements, so a larger gamma-ray flux is expected.

4 Summary

By optimizing the LCS gamma-ray laser optical system, we succeeded in increasing the number of gamma-ray photons by approximately 30%. Although further improvement could be expected from the calculation point of view, it is thought that the accuracy of the optical axis alignment and dirt on the vacuum mirror and vacuum window were the factors. By improving these in the future, we aim to further improve the LCS gamma ray intensity.

Acknowledgement

We are deeply grateful to Mr. H. Hirayama, Mr. S. Nakata, Mr. A. Nakamura, and Dr. Y. Minagawa of SES for their efforts in BL operation. We would also like to thank Mr. T. Ushizawa and Dr. T. Sakurai of JASRI for their great contributions in maintaining the safety interlock system. Finally, we would like to express my deep gratitude to Prof. Miyamoto of Osaka University, who played a central role in overseeing the construction of BL01.

References

[1] D. Filipescu, I. Gheorghe, K. Stopani, S. Belyshev, S. Hashimoto, S. Miyamoto and H. Utsunomiya: *Nuclear Instruments and Methods in Physics Research Section A: Accelerators, Spectrometers, Detectors and Associated Equipment,* **1047**, p.167885 (2022).

[2] T. Ari-Izumi, I. Gheorghe, D. Filipescu, S. Hashimoto, S. Miyamoto. H and Utsunomiya: *J. Instrum.* **18** T06005 (2023).

[3] T. Sanami, T. Tran, T. Nguyen, H. Yamazaki, T. Itoga, Y. Kirihara, Y. Namito, H. Nakashima, S. Miyamoto, S. Hashimoto and Y. Asano: *Proceedings of 19th Annual Meeting of Particle Accelerator Society of Japan*, p.70 (2022).

[4] T. Sanami, T. K. Tran, H. Yamazaki, T. Itoga, Y. Kirihara, Y. Namito, Y. Sakaki, S. Miyamoto and Y. Asano: *15th international conference on nuclear data for science and technology* (ND2022), EPJ Web of Conferences **284**, 01047 (2023).

[5] T. K. Tran, Y. Sakaki, T. Sanami, H. Yamazaki, Y. Namito, T. Itoga, Y. Kirihara, S. Miyamoto and Y. Asano: *15th international conference on nuclear data for science and technology* (ND2022), EPJ Web of Conferences **284**, 01048 (2023).

[6] T. K. Tuyet, T. Sanami, H and Yamazaki: *14th International Conference on Radiation Shielding and 21st Topical Meeting of the Radiation Protection and Shielding Division*, Seattle, WA September 25–29 (2022).

[7] T. Sanami *et al.*: *LASTI Annual Report 2022,* **24** (2023).

[8] M. Omer *et al.*: *LASTI Annual Report 2022,* **24** (2023).

Cross section asymmetry of polarized γ-ray elastic scattering

M. Omer[1], T. Shizuma[2], M. Koizumi[1], R. Hajima[2], S. Hashimoto[3], and S. Miyamoto[4]

[1]Japan Atomic Energy Agency
[2]National Institutes for Quantum Science and Technology
[3]Laboratory of Advanced Science and Technology for Industry (LASTI), University of Hyogo
[4]Institute of Laser Engineering, Osaka University

Abstract

Nondestructive elemental analysis is highly valued in many fields, such as archeology, paleontology, space sciences, nuclear security, and nuclear nonproliferation. These fields usually impose estimating the elemental composition of bulk, large, and inhomogeneous samples nondestructively. Common elemental analysis techniques such as X-ray fluorescence (XRF) may fail in such situations due to the self-absorption of low energy X-rays within thin layers of the sample. In the present study, we propose a novel nondestructive method that may be useful in distinguishing the elemental composition of a given sample based on the elastic scattering of linearly polarized and high-energy γ-rays. Linear polarization of γ-rays causes *asymmetry* of the elastic scattering cross sections with respect to the polarization plane of the incident γ-rays. At specific γ-ray energies and scattering angles, the asymmetry ratio, *R*, of the cross sections in two orthogonal planes is characteristic of each element. Therefore, we anticipate that *R* may be considered as a spectroscopic quantity that can be measured using in-beam γ-ray spectroscopy.

1. Introduction

Elastic scattering of polarized γ-rays by atoms is a complicated interaction comprising many scattering processes such as Rayleigh scattering, nuclear Thomson scattering, and scattering by the strong Coulomb field around the nucleus, known as Delbrück scattering. All of these scattering processes manifest the interactions of γ-rays with charge collections (electrons and nucleus) and their electric field. Theoretical calculations of the scattering amplitudes have been performed and are available for each process[1-4]. Some of the scattering amplitudes, such as nuclear Thomson, are proportional to Z^2, where Z is the atomic number. Other scattering amplitudes, such as Delbrück amplitudes, are proportional to higher orders of *Z*. Thus, the differential cross section of the elastic scattering interaction ($d\sigma$) is, in principle, a unique fingerprint of each element. However, $d\sigma$ is a superposition of the scattering amplitudes of all processes and must be added coherently. At certain conditions, the superposition of the scattering amplitudes results in a considerable asymmetry in the angular distribution of the scattered γ-rays. Figure 1 shows an example of such asymmetry for lead and tantalum elements. This asymmetry may be used in identifying the element under consideration.

Furthermore, the asymmetry of the elastic scattering cross section may be employed to isolate Delbrück scattering contribution by a precise selection of scattering conditions and photon energy[5]. Experimental measurement of Delbrück scattering will provide a unique test of the nonlinear aspects of the quantum electrodynamics[6]. In the past, elastic scattering experiments using linearly polarized γ-rays could not be conducted due to the unavailability of perfectly polarized γ-rays. However, Laser Compton Scattering (LCS) γ-ray sources provide such polarized γ-rays. An example of these LCS sources is the γ-ray beamline (BL01) at the NewSUBARU facility.

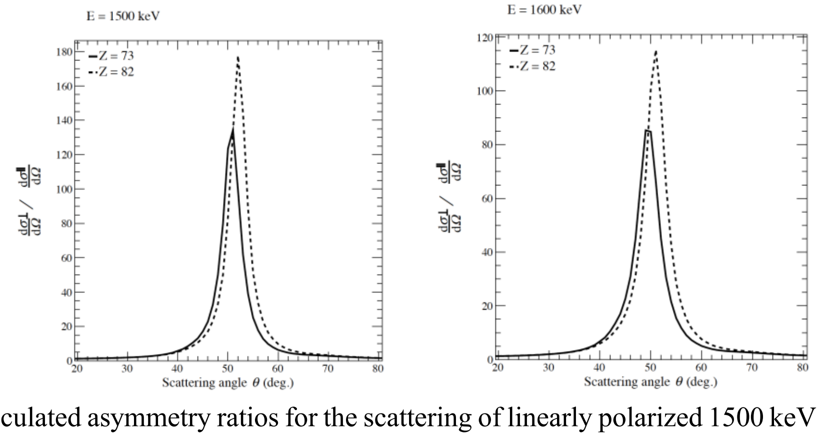

Figure 1. The calculated asymmetry ratios for the scattering of linearly polarized 1500 keV (left) and 1600 keV (right) γ-rays by tantalum and lead atoms.

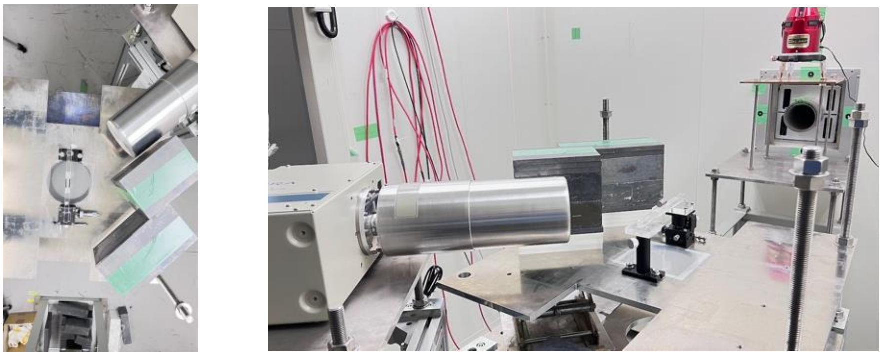

Figure 2. Experimental setup for the elastic scattering experiment of linearly polarized γ-rays, top view (left) and side view (right).

2. Experimental Methods

2.1. Photon scattering measurement

A $20\times8^{\phi}$ mm cylindrical Ta target was irradiated by linearly polarized γ-rays generated by laser Compton scattering at the NewSUBARU facility. Approximately 5-W CO$_2$ linearly polarized laser beam was allowed to collide with 0.95-GeV electrons. The generated γ-rays are linearly polarized with a maximum energy of $1.62^{+0.02}_{-0.18}$ MeV. The elastically scattered γ-rays were measured using a 140% high purity germanium detector positioned horizontally at 15 cm from the center of the target and at 45° in the horizontal direction, as shown in Figure 2. The γ-rays' polarization plane was controlled by a couple of CO$_2$ laser polarizers as a surrogate of half-wave plates. The γ-ray beam flux and profile were measured by moving the HPGe detector in the beam. Furthermore, the γ-ray beam flux was continuously monitored during the measurement by a large NaI detector. The estimated flux of the γ-ray beam was approximately 5.7×10^{4} γ/s in the case of vertically polarized γ-rays. However, the flux of the horizontally polarized γ-ray dropped to approximately one fifth of the value of the vertically polarized flux. This reduction in the flux originates from the intensity loss of the laser beam due to the rotation of the polarization plane.

2.2. Monte Carlo simulation of the beam profile

Accurate estimation of the γ-ray beam profile is required to extract the elastic scattering cross section. We performed Monte Carlo simulations to obtain the γ-ray beam profiles using the LCS simulation models developed[7,8] in the Geant4 simulation toolkit[9]. The γ-ray beam profiles calculated by the simulation are shown in Figure 3 for the horizontal and vertical polarization cases. The measured γ-ray profiles for the two photon polarization states are also shown in Figure 3. Except for the drop in the intensity of the γ-ray beam, there is no observed difference between the beam profiles due to polarization planes.

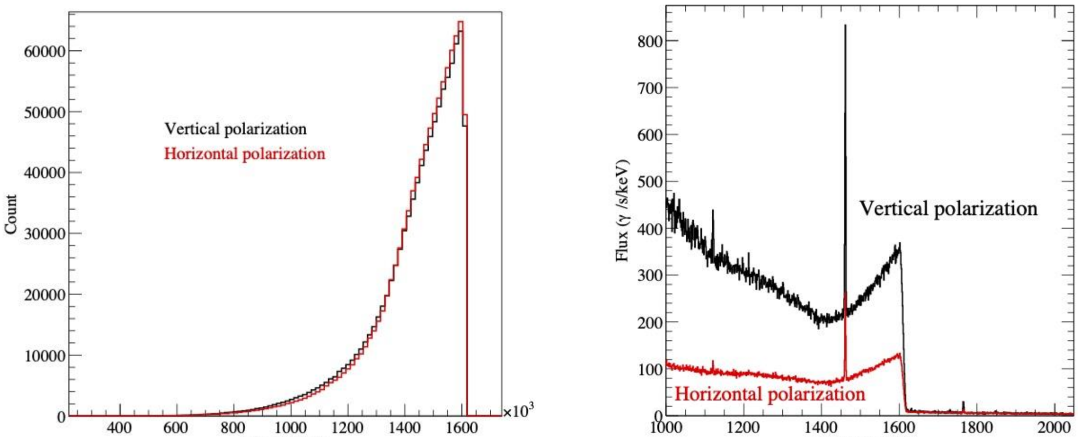

Figure 3. The simulated and measured LCS γ-ray beam profiles for the vertical and horizontal linear polarization states.

3. Results and Discussion

The γ-ray spectra of the elastically scattered photons when the polarization is perpendicular (vertical) and parallel (horizontal) to the scattering plane are shown in Figure 4. The spectra are normalized to the flux of the γ-ray beam measured vertically. Although the statistics of the measurement are not high, there is an observed difference between the two measurements, which may indicate that there is a possible asymmetry in the angular distribution of elastic scattering of polarized γ-rays. These results reveal that the asymmetry in the elastic scattering of γ-rays with respect to the polarization direction of the incident photon could be observed for tantalum atoms. However, much more γ-ray beam flux is required to evaluate the asymmetry due to the polarization of γ-rays.

It should be noted that the spectra shown in Figure 4 represent the average of the elastic scattering cross section over the energy distribution and the angular spread of the detector used in the measurement. The energy distribution spans approximately 100 keV, from 1500 to 1600 keV, while the angular spread of the detector is approximately 30°. As shown in Figure 1, the asymmetry is maximum at 51° and 48° for the energies of 1500 keV and 1600 keV, respectively. However, the asymmetry drops significantly far from these two scattering angles. Therefore, we only observe a low asymmetry ratio due to the energy and angular spreading of the γ-ray beam and scattering angle. In the future, higher γ-ray beam flux will enable a measurement with a much lower angular spread, which may provide a more accurate measurement of the asymmetry ratio.

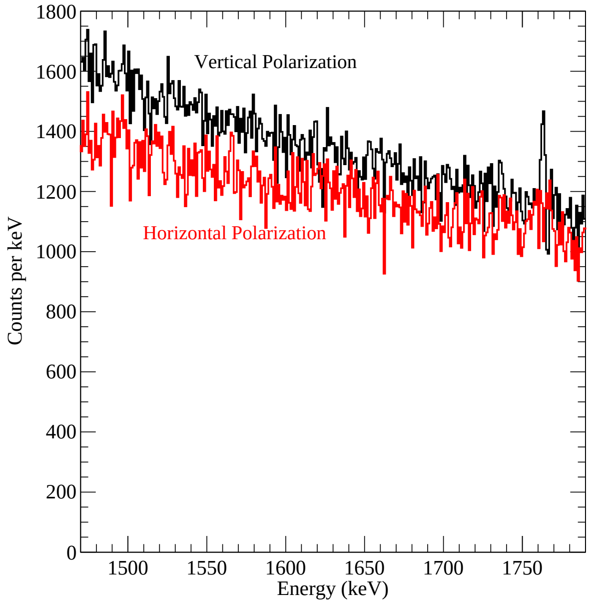

Figure 4. Results of the elastic scattering of linearly polarized γ-rays by Ta target.

4. Conclusion

Asymmetry of the elastic scattering cross section due to linear polarization of γ-rays could be measured for the Ta target at 1.62 MeV. Statistical uncertainty can be improved by increasing the detection efficiency and enhancing the γ-ray beam flux.

Acknowledgement

This work is a contribution of the Japan Atomic Energy Agency (JAEA) to the International Atomic Energy Agency (IAEA) under the agreement of the coordinated research program (CRP), J02015 (Facilitation of Safe and Secure Trade Using Nuclear Detection Technology - Detection of RN and Other Contraband).

References

[1] M. Omer, and R. Hajima: *New J. Phys.*, **21** (11), 113006 (2019).
[2] M. Omer, and R. Hajima: *Nucl. Instrum. Methods Phys. Res. B*, **405**, 43-49 (2017).
[3] L. Kissel: *Radiat. Phys. Chem.*, **59** (2), 185-200 (2000).
[4] H. Falkenberg et al.: *At. Data Nucl. Data Tables*, **50** (1), 1-27 (1992).
[5] J. K. Koga and T. Hayakawa: *Phys. Rev. Lett.*, **118**, 204801 (2017).
[6] J. Sommerfeldt, V. A. Yerokhin, Th. Stöhlker, and A. Surzhykov: *Phys. Rev. Lett.* **131**, 061601 (2023).
[7] R. Hajima: *Nucl. Instrum. Methods Phys. Res., Sect. A*, **985**, 164655 (2021).
[8] Gianfranco Paternò, Paolo Cardarelli, Matteo Bianchini, Angelo Taibi, Illya Drebot, Vittoria Petrillo, and Ryoichi Hajima: *Phys. Rev. Accel. Beams* **25**, 084601 (2022).
[9] S. Agostinelli, *et al.*: *Nucl. Instrum. Methods Phys. Res., Sect. A*, **506** (3), 250–303 (2003).

Implementation of SERS active structures using boehmite in microfluidic devices

Shunya Saegusa[1], Masayuki Naya[2], Takao Fukuoka[1], Sho Amano[1], Yuichi Utsumi[1], Akinobu Yamaguchi[1]

[1]*Laboratory of Advanced Science and Technology for Industry (LASTI), University of Hyogo*
[2]*Faculty of Science and Technology, Keio University*

Abstract

Surface-enhanced Raman scattering (SERS) is high sensitivity, label-free, and suitability for long-term measurement. So, this measurement is expected to be applied to real-time measurements in bioanalysis and environmental analysis. Especially, gold nanofève (GNF)-SERS structure deposited on a boehmite substrate is capable to have high-sensitivity and high-resolution measurements in a wide area. We improved the adhesion of the GNF-SERS active pattern by magnetron sputtering and integrated this sensor into a microfluidic system. To evaluate the performance of the system, 4, 4'-Bypiridine (4bpy) was used for SERS measurement in the microchannel. This study shows that our microfluidic systems with the GNF-SERS active patterned area have the adequate potential for application and development in environmental analysis.

1. Introduction

Surface Enhanced Raman Scattering (SERS) is a spectroscopic method that enhances weak Raman signals by the enhancement of the electric field on the noble metal surface by Local Surface Plasmon Resonance (LSPR), and enables detection of single molecules[1-8]. SERS is characterized by its high sensitivity and label-free measurement, and is also suitable for measurements that take a long time because it is less affected by light fading than the fluorescence method. Because of the above features and the ability to measure samples in water, SERS has been applied mainly to molecular imaging for bioanalysis [2,3]. However, SERS active structures have the disadvantage that they are difficult to fabricate extensively on substrates such as glass. In this study, we have focused on an easy method to fabricate SERS-active structures of gold nanofibers (GNFs) using the boehmite structure, which is an aluminum hydroxide [6-8]. The GNF structures can be fabricated to produce stronger localized electric field enhancement. This method can be used to construct nanoscale noble metal gap structures with high-sensitivity and high-resolution measurement over large areas [6-8]. The conventional method of fabricating noble metal layers using electron beam oblique deposition has high reproducibility and high performance, but has problems in terms of adhesion and stacking area [7,8]. Therefore, we changed the noble metal layer fabrication method from electron beam deposition to magnetron sputtering to investigate the SERS activity sensitivity and to evaluate the distance dependence of the SERS activity from the substrate edge [6]. In this paper, SERS structures were successfully implemented in a microfluidic system [9] by patterning and fabricating them in the desired position and shape based on the above methods. In order to evaluate the performance and characteristics of the microfluidic system, experiments were conducted to see if the detection intensity changes with the time and concentration of specimen flow. If the GNF-SERS structure, which enables single-molecule detection by spectroscopic methods, can be patterned at a desired position and fabricated into a microfluidic system, it is expected to be developed into a molecular imaging system that can measure molecules for a long time, and applied to environmental analysis and drug screening.

2. Experimental

2.1. GNF-SERS structure fabrication method

The GNF-SERS structure was fabricated through a two-step process of boehmite formation on the glass slide surface and oblique sputtering of gold. The specific processes are as follows.

1) Boehmite formation

Formation of an Al layer of 84 nm on a glass slide using magnetron sputtering. The glass substrate is immersed in deionized water heated to 100 ºC and heated for 10 minutes to progress the Al hydroxylation reaction.

2) Diagonal sputtering of gold

As shown in Figure 1, for GNF structure fabrication, the boehmite substrate is tilted 10 degrees and sputtered with about 60 nm of Cr/Au while covered with a cover. The reason for covering the substrate in step 2) is to limit the deposition direction. In addition, we limited the location of the SERS structure formation using a metal mask.

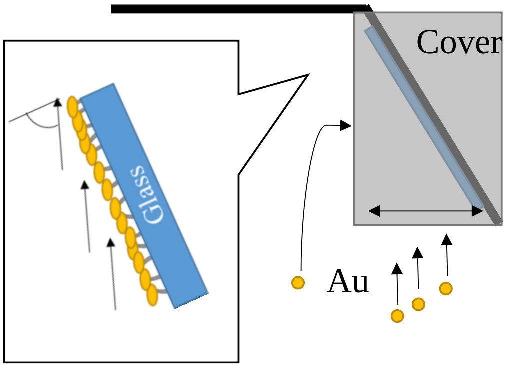

Figure 3. Schematic diagram of diagonal sputtering of gold.

2.2. Fabrication of flow channel structure

Polydimerthylsiloxane (PDMS) was used as a component material for microfluidic devices. PDMS can be transferred to micron-order structures by molding with high accuracy and can be easily sealed by surface treatment with high adhesion to glass and other materials[9].The mold master for molding was made of resin and printed using a 3D printer as shown in Figure 2. The mold was designed to allow SERS measurement while mixing two liquids. PDMS precursor (10:1 liquid mixture of PDMS monomer and cross-linker) was poured onto the prepared master, and heated on a hot plate at 100°C for 30 minutes. Finally, a UV ozone cleaner was used to perform a 5-minute plasma treatment on the bonding surface of the SERS substrate and channel structure before bonding.

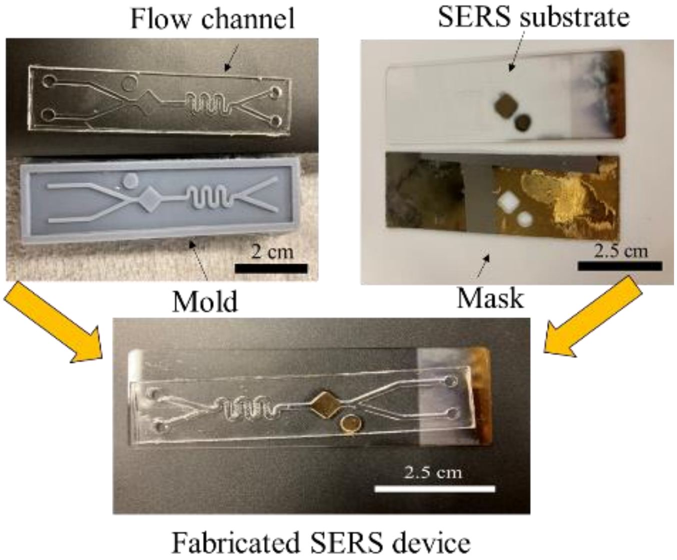

Figure 2. Fabrication of SERS device.

2.3. Fluid Measurement

SERS measurement was attempted using the fabricated microfluidic device. The measurement system is shown in Figure 3, in which pure water and 4,4'-Bipyridine (4bpy) were used as the sample. The measurement method was as follows: 4bpy and pure water were mixed and pumped through a syringe, and a Raman spectroscopy module was used to perform SERS measurements by irradiating a laser beam.

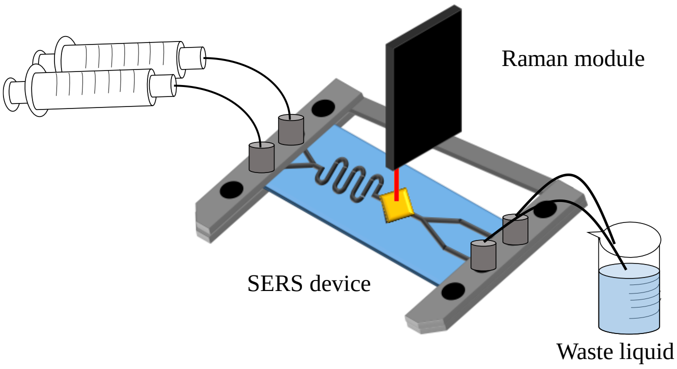

Figure 3. Schematic diagram of fluid measurement system.

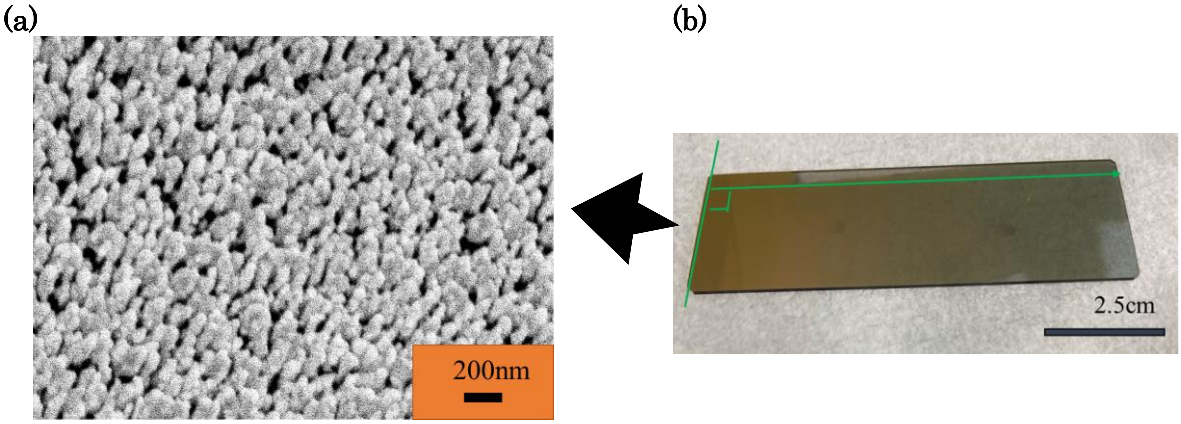

Figure 4. SERS substrate (a) SERS image, (b) Optical photograph.

3. Results and Discussion

3.1. Fabricated SERS device

The fabricated SERS structure is shown in Figure 4 (a), confirming the formation of the GNF-SERS structure. (4bpy) from our previous study up to 100 nM, confirming that the sensitivity is sufficient for application [6]. When the SERS structure is formed on the entire surface of a glass slide, the film thickness is uneven as shown in Figure 4 (b), but SERS activity can be realized in 20 x 20 mm^2 .[6] The structure fabricated using a metal mask made of an Al thin film (0.1 mm) is shown in Figure 6. The transfer was successful, and the increased glass surface area is expected to improve adhesion to the PDMS and prevent water leakage.

3.2. Fabricated SERS device

4bpy (20 μM) and pure water were each pumped at a flow rate of 0.1 mL/min for 40 min. After 40 min of pumping, the pumping was stopped for 10 min. Figure 5 shows the results of the pumping. Figure 6 shows the change in peak intensity at 1614 cm^{-1}. The intensity of the peak at 1614 cm^{-1} increased as the flow rate was changed, and equilibrium was reached in about 15 minutes after SERS was reached. This indicates that sample molecules accumulate. Therefore, if the sample molecules are adsorbable on the SERS substrate, they can be detected at any low concentration if the flow is continued for an extended period of time. The fact that the Raman intensity is maintained even after the fluid has been flowing for more than one hour indicates that

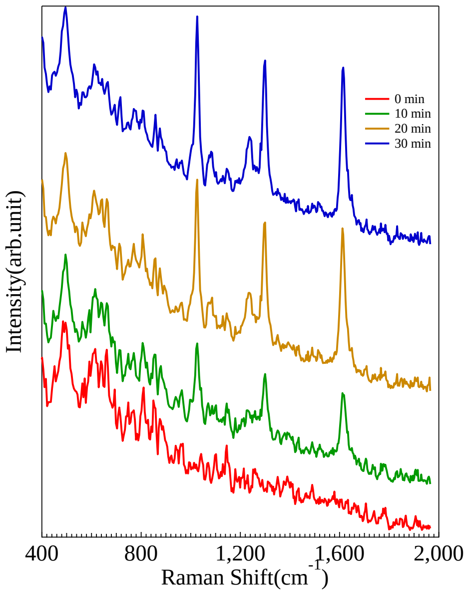

Figure 5. Change in Raman spectra.

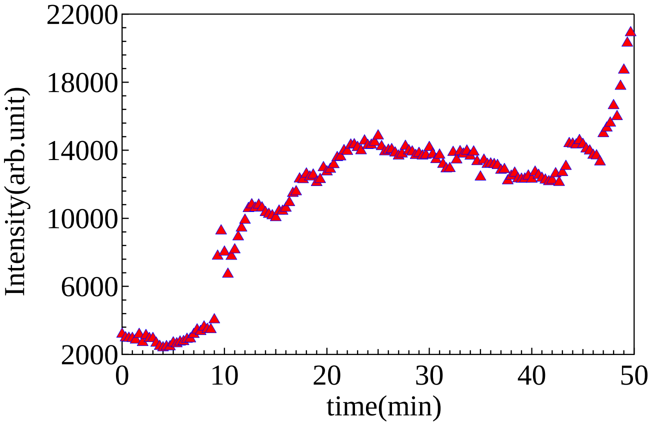

Figure 6. Change in peak intensity (1618 cm^{-1}).

the SERS structure can be used for long-term experiments. In addition, an increase in intensity was observed after the syringe pump was stopped. This may be due to the decrease in flow rate, which reduced the amount of 4bpy detached by the flow and caused more 4bpy to adhere to the electric field enhancement area. Based on the above, we believe that it is possible to develop analytical devices for long-term bioanalysis and environmental analysis by verifying the relationship between the change in saturation intensity with flow rate and the arrival time of saturation intensity with concentration.

4. Conclusion

In this study, we implemented GNF-SERS with a Boehmite substrate in a microfluidic device and attempted to measure SERS of fluids. As a result, we succeeded in measuring a fluid of 4bpy equivalent to 10 μM. It was found that the intensity saturated as the sample molecules accumulated and became more numerous than in the electric field enhancement area when the fluid continued to flow for a long period of time. The fact that SERS activity was always shown during the one-hour long experiment suggests the possibility of application to real-time measurements in bioanalysis and environmental analysis.

Acknowledgement

This research and development were supported by Grant-in-Aid for Scientific Research (22H01920), Tokyo Ohka Foundation for Science and Technology, and Hyogo Science and Technology Association. We would like to express our deepest gratitude to the following organizations.

References

[1] K. Kneipp, Y. Wang, H. Kneipp, L. T. Perelman, I. Itzkan, R. R. Dasari, and M. S. Feld: *Phys. Rev. Lett.*, **78**, 1667 (1997).

[2] C. Zong, M. Xu, L. Xu, T. Wei, X. Ma, X. Zheng, R. Hu, and B. Ren: *Chem. Rev.*, **118**, 4946−4980 (2018).

[3] H. Wei, S. M. H. Abtahi, and P. J. Vikesland: *Environ. Sci.: Nano*, **2**, 120 (2015).

[4] A. Yamaguchi, T. Fukuoka, R. Hara, K. Kuroda, R. Takahashi and Y. Utsumi: *RSC Adv.*, **5**, 73194 (2015).

[5] N. Chen, T. Xiao, Z. Luo, Y. Kitahama, K. Hiramatsu, N Kishimoto, T. Itoh, Z Cheng, and K. Goda: *Nat. Comm.*, **11**, 4772 (2020).

[6] T. Tanaka, S. Saegusa, M. Naya, T. Fukuoka, S. Amano, Y. Utsumi, A. Yamaguchi: *J. Photopolymer Sci. Technol.*, **35.3**, 249-253, (2022).

[7] S. Saegusa et al.: *IEEJ Trans. E* **143(6)**, 120-125. (2023).

[8] M. Shiota, M. Naya, T. Yamamoto, T. Hishiki, T. Tani, H. Takahashi, A. Kubo, D. Koike, M. Itoh, M. Ohmura, Y. Kabe, Y. Sugiura, N. Hiraoka, T Morikawa, K. Takubo, K. Suina, H. Nagashima, O. Sampetrean, O. Nagano, H. Saya, S Yamazoe, H. Watanabe and M. Suematsu: *Nat. Comm.*, 9, 1561, (2018).

[9] S. Yamazoe, M. Naya, M. Shiota, T. Morikawa, A. Kubo, T. Tani, T. Hishiki, T. Horiuchi, M. Suematsu, and M. Kajimura: *ACS Nano*, **8**, 6, 5622–5632, (2014).

[10] K. Gale, A. R. Jafek, C. J. Lambert, B. L. Goenner, H. Moghimifam, U. C. Nze and S. K. Kamarapu: *Inventions*, **3**, 60 (2018)

Study of Dihedral-Corner-Reflector-Array Fabrication Process Using Soft X-ray Deep X-ray Lithography

Taki Watanabe[1], Sho Amano[1], Shinya Izawa[1], Satoshi Maekawa[2], Keisuke Yoshiki[3], Akinobu Yamaguchi[1], and Yuichi Utsumi[1]

[1]Laboratory of Advanced Science and Technology for Industry (LASTI), University of Hyogo
[2]Parity Innovations Co. Ltd.
[3]Institute for Research Promotion and Collaboration

Abstract

We fabricated sectoral-pillar structures for Dihedral Corner Reflector Array (DCRA) using Deep X-ray Lithography (DXRL) in New SUBARU Synchrotron Radiation Facility. We studied process conditions such as a start timing of development after exposure and development temperature. We succeeded in fabricating a structure without of micro-cracks on sidewalls of the pillar and in demonstration of floating image using the fabricated DCRA.

1. Introduction

In recent years with the COVID-19, demand for non-contact terminal operation to avoid contact infection, has increased. To realize non-contact operation, a visible floating image and a sensor-based operation system are required. A Dihedral Corner Reflector Array (DCRA), which consists of two right-angle plane mirrors to generate floating image in the air, was proposed[1-4].

Fig. 1(a) shows the principle of DCRA. In a DCR the total reflections of a light-ray occur by two mirrors. Fig. 1(b) shows a path of light in XY plane of the DCR. When the angle of incidence is θ, the light from a source is reflected and returns to the source with an angle of 180° according to Equation (1)[3]. In three dimensions, the light from the source does not return to the source but reaches a symmetry point for the DCRA device face. This point is an observation point (Fig. 1(a)).

$$2\theta+2(\pi/2-\theta)=\pi \tag{1}$$

By mounting many DCRs perpendicularly to a substrate, the real image can be formed at the observation point. The image sharpness is determined by surface clearness and right-angle accuracy of the DCR walls. However, it is not easy to produce such a microstructure with high precision by conventional machining. Therefore, we propose the use of DXRL technology for DCRA production. DXRL has several advantages: it is easy to fabricate microstructures with high aspect ratio, mirror surfaces can be machined with high precision, and it is a mass-production technology that can reduce costs[5-15]. Furthermore, by changing the pattern of the X-ray mask, desired cross-sectional shapes can be easily created. DCR shapes created previously were limited to square pillars or holes[1, 3]. In such shapes, the other two faces that do not contribute to required imaging may produce ghost. Therefore, in this study, we developed prototype pillar structures with a sectoral cross section as shown in Fig. 2 by DXRL, in which all surfaces except the two corner reflectors are curved. Shown in Fig. 2 is an X-ray mask used in DXRL.

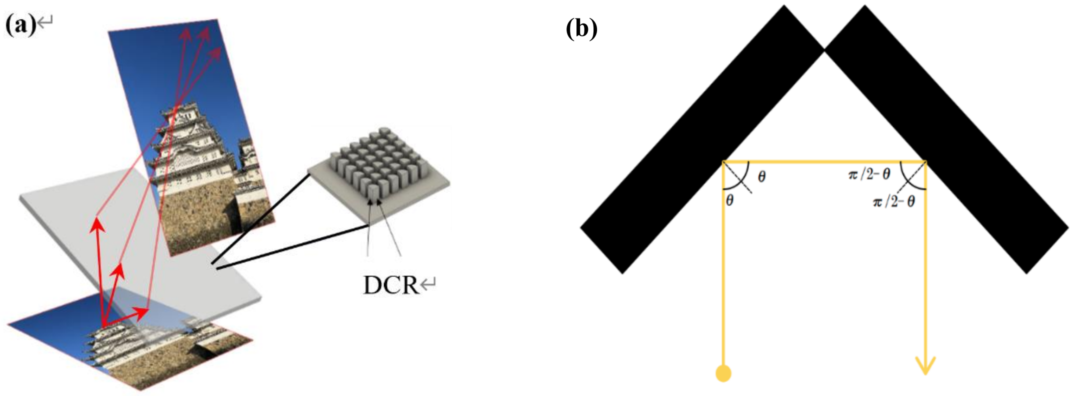

Figure 1. (a) Principle of DCRA, (b) Trajectory of the ray.

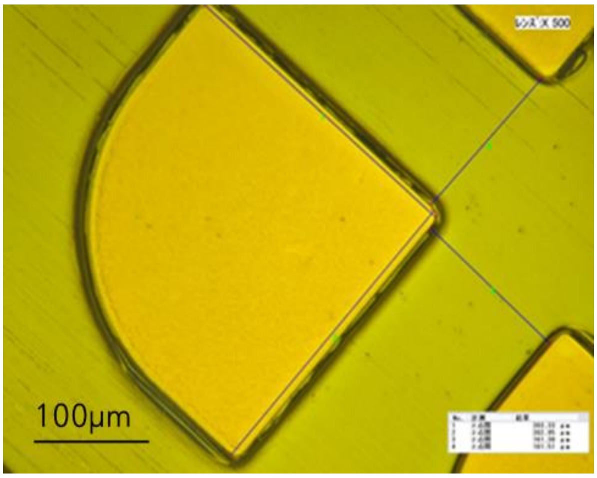

Figure 2. Unique sectoral shaped x-ray mask.

2. Experimental

Exposure experiments were carried out in the NewSUBARU synchrotron radiation facility in the University of Hyogo. There are two modes of electron storage energy, 1.0 GeV and 1.5 GeV, but in this study, we used the 1.5 GeV mode, which has higher X-ray energy and allows deeper processing. In BL11, synchrotron radiation X-rays are passedthrough a toroidal mirror and two Be filters to cut off energy components below 2 KeV. The spectrum at the exposure plane is shown in Fig. 3(a). The X- ray energy range is 3KeV-8KeV, with a peak of approximately 6KeV. The beam pattern is shown in Fig. 3(b) and the beam is highly paralleled with a divergence of 278 µrad in the horizontal direction and 14 µrad in the vertical direction[7].

In this study, PMMA (CLAREX Precision Sheet, Nitto Jushi Kogyo Co., Ltd) pillar structures are tested. The critical angle of PMMA was calculated to be 42.2° from Snell's law, and the aspect ratio should be 2 to realize a two-times reflections in DCR. The smaller DCR size causes the higher space-resolution, but the image becomes darker because of diffraction, so there is an optimum size. There is an optimum DCR pitch for a focal distance. Based on the above, we determined the dimensions of the device to be fabricated in this study as shown in Table 1.

We used GG developer solution for the development and developed the PMMA samples for 24 hours. The ingredients of the developer are shown in Table 2. The development temperature and the elapsed time to start development were changed and their optimum conditions were researched.

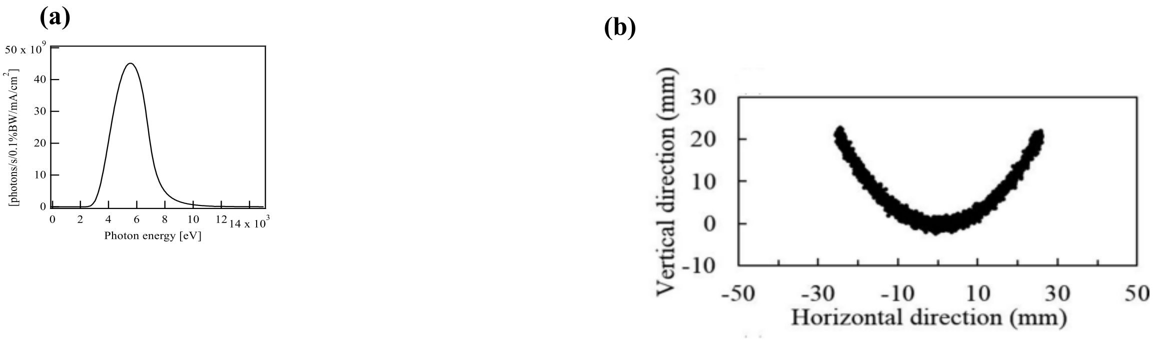

Figure 3. (a) Photon intensity distribution as a function of photon energy at the beamline BL11, (b) beam shape[7].

Table 1. Target values and Measurements of each dimension of the DCR (parameters are defined in Fig. 6).

		target value	measurements
X wall	Upper distance [μm]	300	301.6
	Lower distance [μm]	300	303.5
	Upper side length [μm]	175	174.7
	Lower side length [μm]	175	171
	Verticality [mrad]	0	1.72
Y wall	Upper distance [μm]	300	291.9
	Lower distance [μm]	300	306.4
	Upper side length [μm]	175	186
	Lower side length [μm]	175	171.5
	Verticality [mrad]	0	13.1
	Average height [μm]	600	553

Table 2. Ingredients of the GG developer.

Ingredient	Vol%
2-(2-n-butoxy-ethoxy)ethanol	60
Tetrahydro-1, 4-oxazine	20
2-amino-ethanol-1	5
D. I. Water	15

3. Results and Discussion

We succeeded in fabricating a DCRA without micro-cracks on the pillar wall surface in the optimized development condition. The unique sectoral shaped DCRA fabricated is shown in Fig. 4. The exposure dose was 150 J/cm^2. The developing conditions at this time were a developing solution temperature of 37.8°C and an elapsed time to start development of 15 minutes.

Using this DCRA, we observed a floating image as shown in Fig. 5. The DCRA size was 2 cm square.

The scale parameters of each part of DCRA are defined as shown in Fig. 6. The target dimensions and measured values of the fabricated DCRA are summarized in Table 1. Although the floating image was successfully formed using the fabricated new DCRA, there is still a problem to be solved to obtain clearer image. It is the verticality of the DCR pillar is poor. In Table 1, the verticality is clearly worse on the Y wall than on the X wall. We consider this cause is due to thermal inhomogeneous by X-ray beam scanning. Since the X wall is perpendicular to the beam scan direction, similar thermal mass is given simultaneously, but since the Y wall is parallel, a continuous distribution of thermal mass is created.

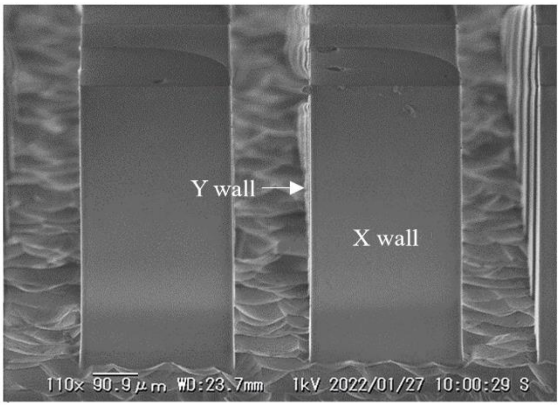

Figure 4. The unique sectoral shaped DCRA fabricated.

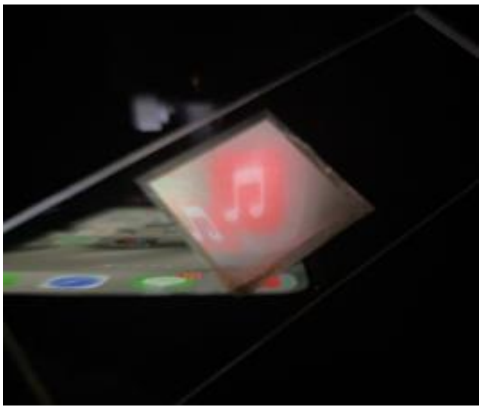

Figure 5. Floating image formed using the fabricated DCRA.

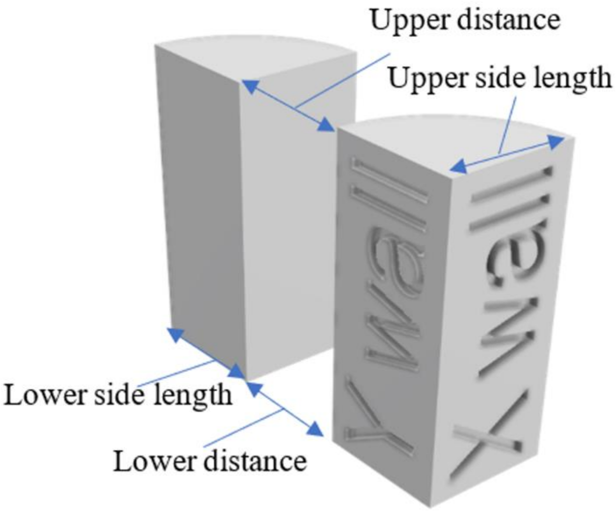

Figure 6. Scale parameters of each part of DCRA.

4. Conclusion

In this study, we fabricated a new DCRA device that can generate a floating image in the air. In conventional square DCRA, two surfaces that do not contribute to image formation may cause the generation of ghost images. Therefore, we fabricated a unique sectoral-pillar DCRA that is expected to generate less ghost. For this micro-fabrication, we studied the PMMA fabrication process by DXRL at a BL11 in NewSUBARU. By trying various development conditions, we found the condition under which micro-cracks on the pillar wall were not observed. Using the DCRA fabricated, floating imaging was observed. However, the verticality of the pillar still needs improvement. We will improve the exposure and development process in order to establish a DCRA processing by DXRL.

References

[1] A. Yamaguchi, S. Maekawa, T. Yamane, I. Okada, Y. Utsumi: *Transactions of The Japan Institute of Electronics Packaging.* **8**, 23 (2015).
[2] D. Miyazaki, N. Hirano, Y. Maeda, S. Yamamoto, T. Mukai, S. Maekawa: *Applied Optic.* **52**, A282 (2013).
[3] J. G. Korvink, S. Haf, S. Maekawa: *Nanotech Japan Bulletin.* **7**, No.4 (2014).
[4] S. Maekawa, Y. Hirai, O. Matoba: *Proc. SPIE.* 63920E (2006).
[5] Meyer: *LIGA and its Applications,* (2009).
[6] Y. Utsumi, T. Kishimoto, T. Hattori, H. Hara: *Jpn. J. Appl. Phys*. **44**, 550 (2005).
[7] M. Takeuchi, A. Yamaguchi, Y. Utsumi: *J. Synchrotron Rad*. **26**, 528 (2019).
[8] W. Ehrfeld, V. Hessel, H. Lowe, Ch. Schulz, L. Weber: *Microsystem technologies.* **5**, 105 (1999).
[9] F. Perennes, B. Marmiroli, M. Matteucci, M. Tormen, L. Vaccari, E. Di. Fabrizio: *J. Micromech. Microeng.* **16,** 473 (2006).
[10] F. Karlsruhe: *Sensors and materials*, **10,** 363 (1998).
[11] V. Saile, U. Wallrabe, O. tabata, J. G. Korvink: *LIGA and Its Applications*, Wiley-VCH Verlag GmbH & Co. KGaA. **51** (2008).
[12] S. Lemke, P. Goettert, I. Rudolph, J. Goettert, B. Lochel: *Proceedings MNE Conference.* (2013).
[13] G. Feiertag, W. Ehrfeld, H. Freimuth, H. Kolle, H. Lehr, M. Schmidt, M. M. Sigalas, C. M. Soukouli, G. Kiriakidis, T. Pedersen, J. Kuhl, W. Koenig: *Appl. Phys. Lett.* **70**, 1441 (1997).
[14] B. Lai, D. C. Mancini, W. Yun, E. Gluskin: *Microlithography and Metrology in Micromachining.* **2**, (1996).
[15] H. Scheunemann, B. Loechela, L. Jiana, D. Schondelmaier, Y. M. Desta, J. Goettert, *Smart Sensors, Actuators, and MEMS.* (2003).

Upgrading to expand available X-ray energy range for energy device analysis in BL05C, the NewSUBARU

Koji Nakanishi

Laboratory of Advanced Science and Technology for Industry (LASTI), University of Hyogo

Abstract

BL05C of the NewSUBARU synchrotron radiation facility, University of Hyogo (NS-BL05C) is capable of performing XAS measurements of soft/tender X-rays in the 1-4 keV energy range, which has been used for reaction mechanism analysis and degradation analysis of various energy devices (e.g., next-generation lithium-ion batteries, innovative secondary batteries, fuel cells, and water electrolysis devices). However, due to its available X-ray energy range, XAS measurement of 3d transition metals, which are contained as a major component in electrode active materials, has not been possible so far. The hard X-ray XAS spectra of the K-edge of 3d transition metals obtained at NS-BL05C are highly accurate and have been used in industrial applications such as energy devices, The hard X-ray XAS spectra of 3d transition metal K-edge obtained at NS-BL05C are found to be very accurate and useful for the analysis of real industrial samples such as energy devices.

1. Introduction

BL05C of the NewSUBARU synchrotron radiation facility (NS-BL05C) is a relocated, refurbished, and upgraded beamline from the former BL05A, where soft/tender X-rays were available[1]. It has been in operation since FY2021 to contribute to industrial analysis, especially to the analysis of energy devices such as lithium-ion secondary batteries (LIBs), next-generation LIBs, innovative secondary batteries, fuel cells, water electrolysis technology, and methanation technology. NS-BL05C is capable of X-ray absorption spectroscopy (XAS) measurements using soft and tender X-rays in the 1-4 keV range, and has been used for industrial analysis of lithium-ion secondary batteries (LIBs)[2] and next-generation LIBs as well as semiconductor-related products and glass-related products. The elements and X-ray absorption edges that can be analyzed at NS-BL05C are mainly the *K* absorption edge (K-edge) of period third periodic elements

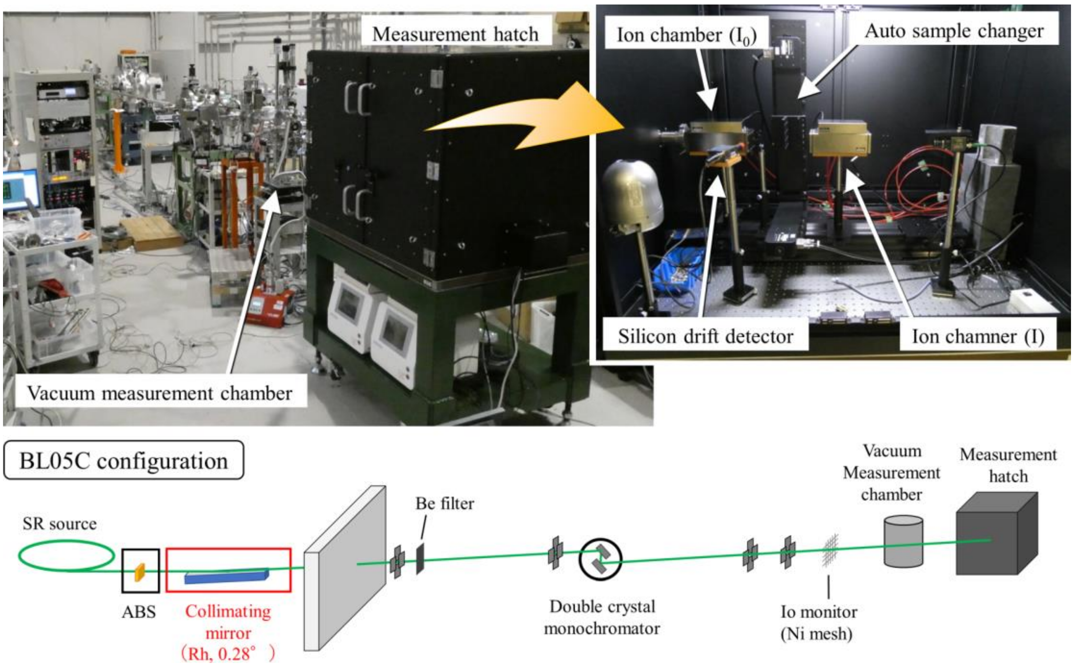

Figure 1. Configuration of NS-BL05C.

(e.g., Mg, Al, Si, P, S, Cl, etc.) and the *L* absorption edge of fifth periodic elements (e.g., Sr, Zr, Nb, Mo, Ru, Rh, Pd, Ag, etc.). However, these elements and X-ray absorption edges alone are not satisfactory for the analysis of a wide variety of energy devices, and more elements were expected to be included in XAS measurements. For XAS measurements, it is essential to extend the incident X-ray energy available at the beamline to cover more elements and X-ray absorption edges to be measured. The K-edge of 3*d* transition metals (TMs) is located in the hard X-ray region above 4 keV, and it is very important for the beamline upgrading strategy to be able to measure them because they are found in many industrial samples.

Therefore, NS-BL05C was upgraded to be able to use hard X-rays above 4 keV by replacing the optical system and installing a measurement hutch and a new detection system. Since the New SUBARU is a synchrotron radiation facility specializing in the use of soft X-rays, there has been no beamline available for hard X-rays with spectroscopy. The upgrade of NS-BL05C was challenging because there were no beamlines that could be referenced. The hard X-ray XAS spectra obtained as a result of this upgrade are described below.

2. Experimental details

All XAS measurements were performed at NS-BL05C. It mainly consists of a collimating mirror, a Golovchenko-type double crystal monochromator (DCM), an X-ray intensity monitor (I_0 monitor), and various optical apertures and slits. In addition, a vacuum measurement chamber and a load-lock chamber for sample introduction without air exposure are available for soft X-ray XAS, as well as a measurement hatch for hard X-ray XAS shown in Fig. 1. In order to obtain 1-10 keV monochromatic X-rays, Beryl(10-10), KTP(011), quartz(10-10), InSb(111), Si(111), Ge(111), Si(220), Ge(220), Si(311), Ge(311) are prepared for the DCM and are exchanged depending on measurement conditions.

All powder samples were pelletized by mixing with boron nitride powder. All XAS spectra were obtained by the transmission mode. To evaluate the XAS spectra observed at NS-BL05C, those observed at BL14B2 of the SPring-8 (SP8-BL14B2)[3] were used as reference spectra.

3. Results and Discussion

Figure 2 shows the V K-edge XAS spectra, EXAFS oscillations, and the Fourier transform of k^2-weighted EXAFS spectrum (radial distribution function) of V_2O_5 observed at NewSUBARU BL05C and SP8-BL14B2 for comparison[4]. The spectra of V_2O_5 observed at SP8-BL14B2 are also shown for comparison in Fig. 2. A comparison of both spectra shows that they are in very good agreement. One slight difference is that the pre-edge peak is slightly higher in the XANES spectrum for SP8. This is presumably due to the slightly higher

Table 1. XAS conditions of observed and referenced V K-edge XAS spectra for V_2O_5.

Facility / Beamline	Crystals	Scan	Range	Points	dwell	Total time
NewSUBARU / BL05C	Ge(220)	Step	5400 – 6400 eV	476	0.1 s	20 min.
SPring-8 / BL14B2 [3]	Si(111)	Quick	5140 – 6970 eV	4238	0.1 s	8 min.

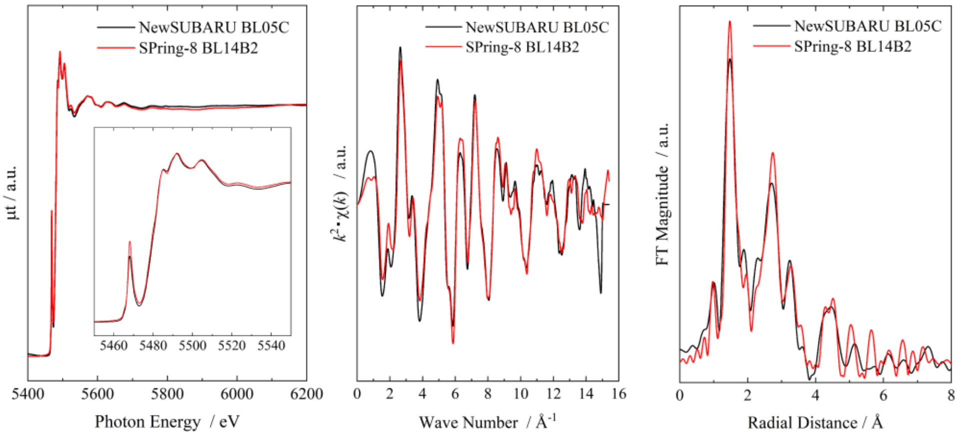

Figure 2. V K-edge XAS spectra, EXAFS oscillation, and the radial distribution functions for V_2O_5. XAS data of "SPring-8 BL14B2" is referenced from MDR XAFS Database[3].

resolution of SP8-BL14B2. This difference in resolution may possibly be due to differences in the

Table 2. XAS conditions of observed and referenced Mn, Co, Ni K-edge XAS spectra for $LiMn_{0.33}Co_{0.33}Ni_{0.33}O_2$.

Facility Beamline	Crystals	Scan	Edge	Range	Points	dwell	Total time
NewSUBARU (NS) BL05C	Ge(311)	Step	Mn	6433 – 7377 eV	409	1 s	16 min.
			Co	7576 – 8370 eV	414	1 s	16 min.
			Ni	8172 – 9164 eV	519	1 s	21 min.
SPring-8 (SP8) BL14B2 [4, 5]	Si(111)	Quick	Mn, Co	6204 – 8046 eV	4262	0.05 s	4 min.
			Co, Ni	7379 – 9224 eV	4462	0.05 s	4 min.

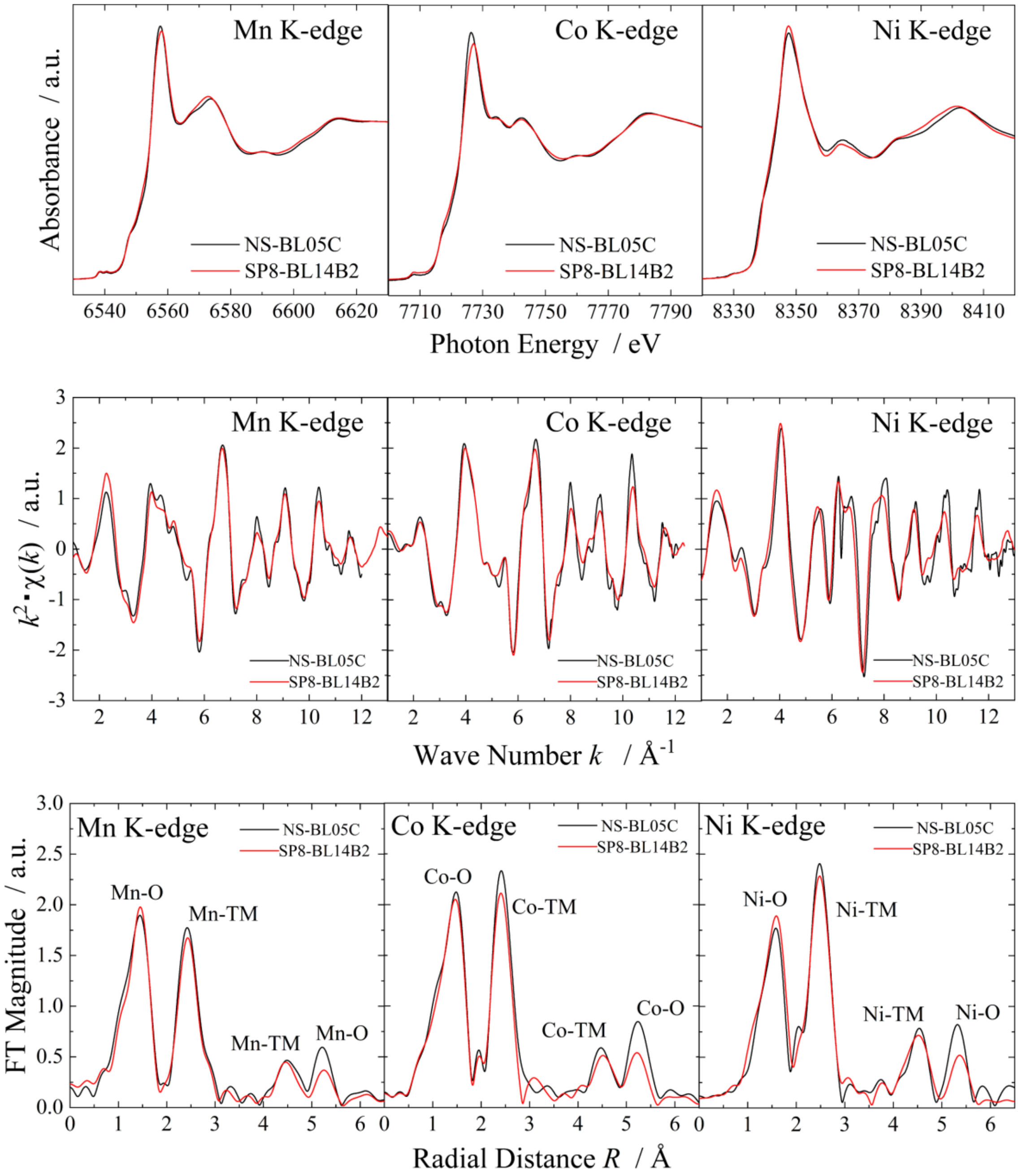

Figure 3. Mn, Co, Ni K-edge XAS spectra, EXAFS oscillation, and the radial distribution functions for $LiMn_{0.33}Co_{0.33}Ni_{0.33}O_2$. XAS data of “SP8 BL14B2” is referenced from MDR XAFS Database[4, 5].

crystallinity of the V_2O_5 reagents used in each measurement. Regarding EXAFS vibrations, the SP8-BL14B2 spectrum shows oscillation structures even at k > 16 Å, whereas the NS BL05C spectrum shows a disturbance of the oscillation structures around k = 14.5 Å. This directly indicates the accuracy of the spectrum, indicating that SP8-BL14B2 has higher measurement accuracy. Regarding the radial distribution function, again, good agreement is observed between the two, but the peak resolution appears to be higher for SP8-BL14B2 due to the accuracy of the EXAFS vibrational structure. These results suggest that the XAS spectrum of NS BL05C is slightly less accurate than that of SPring-8 BL14B2 in the range of 5-6 keV where the V K-edge exists, but it is still effective enough for the analysis of actual industrial samples.

Figure 3 shows the Mn, Co, Ni K-edge XAS spectra, EXAFS oscillations, and the radial distribution functions of $LiMn_{0.33}Co_{0.33}Ni_{0.33}O_2$ observed at NS-BL05C and SP8-BL14B2 for comparison. $LiMn_{0.33}Co_{0.33}Ni_{0.33}O_2$ is known to be a typical positive electrode material in present practical LIBs. With respect to the XANES spectra in Fig. 3, the shapes of the two are almost identical, but the slight discrepancy is thought to be due to the stoichiometric ratio and crystallinity of $LiMn_{0.33}Co_{0.33}Ni_{0.33}O_2$ used in the measurements, as well as impurities in the $LiMn_{0.33}Co_{0.33}Ni_{0.33}O_2$. Regarding the EXAFS vibrations and radial distribution functions, the characteristics of the two are almost identical. This result indicates that the XAS spectra obtained at NS-BL05C are sufficient for LIB analysis.

4. Conclusion

In order to expand the range of target elements for XAS measurements at NS-BL05C, which is capable of soft X-ray and tender X-ray XAS at 1-4 keV, the optics were replaced and a new measurement hutch was installed. This has made it possible to use hard X-rays in the energy range of 4-10 keV. The K-edges of 3*d* TMs in this energy range was measured and evaluated. As a result, it was found that the XAS spectra were equivalent to those observed at SP8-BL14B2.

Comparing the differences in the measurement conditions between NS-BL05C and SP8-BL14B2, it could be seen that the measurement times differ significantly. In other words, NS-BL05 is effective enough for the measurement of the equilibrium state, but for the measurement of one spectrum in a short time, as in the *operando* measurement, the measurement time needs to be shortened. To solve this problem, we are planning to introduce a quick-scan system at NS-BL05C in the future.

Acknowledgement

A part of this study was supported financially by the NEDO RISING3 project.

References

[1] K. Nakanishi: *LASTI Annual Report* **23** (2022) 27.

[2] K. Nakanishi, T. Mori, H. Ohzono, K. Kanda, S. Suzuki: *Adv. X-Ray. Chem. Anal., Japan.* **54** (2023) 185.

[3] XAFS spectrum of Vanadium(V) oxide: "https://mdr.nims.go.jp/concern/datasets/z890rw79s", MDR XAFS Database, National Institute for Materials Science, Japan.

[4] XAFS spectrum of Lithium nickel manganese cobalt oxide: "https://mdr.nims.go.jp/concern/datasets/s7526f74k", MDR XAFS Database, National Institute for Materials Science, Japan.

[5] XAFS spectrum of Lithium nickel manganese cobalt oxide: "https://mdr.nims.go.jp/concern/datasets/8049g725n", MDR XAFS Database, National Institute for Materials Science, Japan.

Selective excitation of Si-H-DLC Films using BL07A for Monochromatized Soft X-ray Irradiation

Tomohiro Mishima[1], Koji Nakanishi[1], Masahito Niibe[1], and Kazuhiro Kanda[1]

[1]*Laboratory of Advanced Science and Technology for Industry (LASTI), University of Hyogo*

Abstract

Highly hydrogenated diamond-like carbon film containing Si (Si-H-DLC) films were irradiated with monochromatized soft X-ray using BL07A, to clarify the photochemical reaction due to soft X-ray irradiation on Si-H-DLC films. The irradiation of soft X-ray of 155 eV was found to oxidize the Si-H-DLC film surface, on the other hand, the chemical state in the bulk of the film was unchanged. The irradiation of soft X-ray of 290 eV showed almost no change in chemical state of both the surface and the bulk. As a result, the soft X-ray irradiation effect on the Si-H-DLC films was found to be dependent on the incident light energy.

1. Introduction

The energy of the inner-shell electrons depends on the element, which varies greatly from element to element, allowing selective excitation. The K-shell energies of elements in the second and third periods are in the soft X-ray region. BL07A is a beamline constructed to irradiate samples with high-brightness monochromatized soft X-rays by the combination of undulator and multilayer mirror monochromator[1].

Diamond-like carbon film (DLC film) is an amorphous carbon film consisting of carbon atoms with sp^2 hybridized orbitals, carbon atoms with sp^3 hybridized orbitals, and hydrogen atoms. DLC films have various excellent properties such as high hardness, low coefficient of friction, and gas barrier property, and are used in a wide field of industries. Highly hydrogenated DLC (H-DLC) films, which contain more than 40 at. % hydrogen, maintain a low coefficient of friction even in a vacuum, and are therefore attracting attention as solid lubricants for use in artificial satellites[2]. However soft X-rays penetrate in a vacuum such as outer space unlike in the atmosphere. Therefore, it is necessary to investigate the soft X-ray resistance of H-DLC films to use these films safely in space. Our group has been studying the effect of soft X-ray irradiation on H-DLC films[3]. We have previously reported that H-DLC films exhibited volume loss and hydrogen desorption upon soft X-ray irradiation[3]. In addition, we reported that H-DLC films containing Si (Si-H-DLC films) exhibited suppression of hydrogen desorption upon soft X-ray irradiation[4]. To elucidate the soft X-ray irradiation effect on Si-H-DLC films more deeply, it is necessary to irradiate monochromatized soft X-rays to the Si-H-DLC films and to clarify the energy dependence of the structural change process of the Si-H-DLC films.

In this study, Si-H-DLC films were irradiated with monochromatized soft X-rays at different energies, and the chemical state changes of the films were discussed from the measurement of Si K-edge X-ray absorption near edge structure (XANES) spectra.

2. Experimental

Irradiation experiments of synchrotron radiation were performed at BL07A, which has an undulator as a light source and a multilayer mirror monochromator to provide high-brightness monochromatic light, in the NewSUBARU synchrotron radiation facility[1]. The undulator of BL07 is a 3 m short planner type undulator consisting of 28 cycles of permanent magnets with a period length of 76 mm. The multilayer mirror monochromator of BL07A is suitable for cutting out one harmonic of undulator light[5]. By using a undulator and a multilayer mirror monochromator, a sample at the irradiation chamber of BL07A can be irradiated with about 10^{14} photons/cm^2 between 50 eV ~ 400 eV and about 10^{13} photons/cm^2 between 400 eV ~ 800 eV[6].

Si-H-DLC films (thickness: 522 nm, composition ratio: Si 40%, H 20%) were deposited on Si substrates by plasma enhanced CVD. In this experiment, the samples were irradiated at 155 eV (photon flux density: 5.37×10^{11} photons/cm^2), which corresponds to the L absorption edge of Si, and at 290 eV (photon flux density: 1.05×10^{13} photons/cm^2), which corresponds to the K absorption edge of C. Si K-edge XANES measurements were performed at BL05C in the NewSUBARU synchrotron radiation facility. The light source of BL05C is a bending magnet and a double crystal monochromator is equipped.

3. Results and Discussion

The Si K-edge XANES spectra of the Si-H-DLC films recorded with the total electron yield method and the

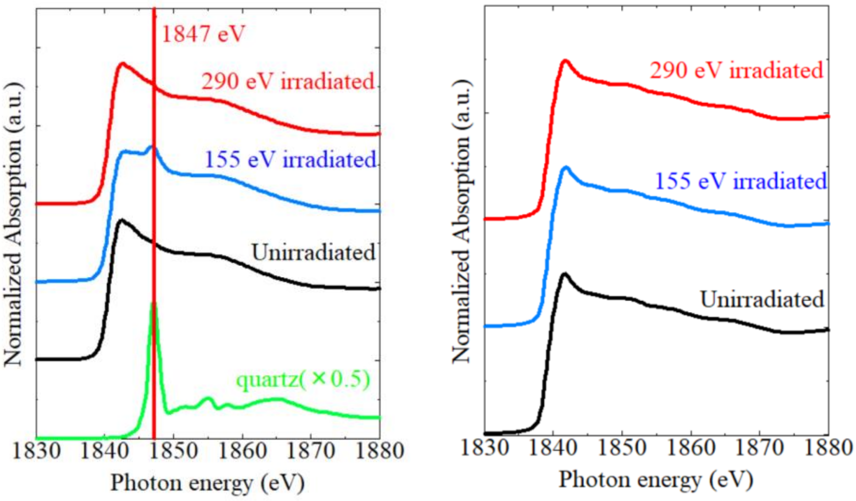

Figure 1. Si K-edge XANES spectra recorded with the total electron yield (left) and the partial fluorescence yield (right).

partial fluorescence yield method were depicted in Figures 1. The absorption spectrum with the total electron yield method provides information on the surface of the sample, on the other hand, that of the partial fluorescence yield method provides information on the bulk of the sample. In Figure 1, the black line is the spectrum of the unirradiated sample, the blue line is the spectrum of the sample irradiated with 155 eV soft X-ray, and the red line is the spectrum of the sample irradiated with 290 eV soft X-ray. The green line is the spectrum of quartz as a reference, which is multiplied by 0.5 on the vertical axis. By comparing the shape of each spectrum, it was found that only in the spectrum of the sample irradiated with 155 eV soft X-ray has a new peak at 1847 eV. The position of this peak at 1847 eV is consistent with that of the quartz. Therefore, the change in the spectrum of the sample irradiated with soft X-rays at 155 eV can be attributed to the oxidation of silicon. By comparing the shape of each spectrum recorded by the partial fluorescence yield, it was found that there was no significant change. It showed that the interior of the film was not changed of chemical state by soft X-ray irradiation. Therefore, silicon oxidation is considerable to limit in the surface of the Si-H-DLC film.

These results suggest that the irradiating of 155 eV soft X-ray mainly excited the L-shell electrons of Si on the Si-H-DLC film surface, and the Si-C and Si-H bonds were broken, producing Si dangling bonds. And then recombined with oxygen in the vacuum chamber or in the air after remove from the vacuum chamber. The soft X-ray irradiation at 290 eV did not cause the aforementioned reaction, indicating that the soft X-ray irradiation of the Si-H-DLC film was dependent on the incident light energy.

4. Conclusion

By irradiating Si-H-DLC films with monochromatized soft X-rays of different energies and comparing XANES spectra, we found that the soft X-ray irradiation effect on Si-H-DLC films was dependent on the incident light energy. In addition, we found that Si-H-DLC films react with 155 eV soft X-ray irradiation, which is less photon flux density than 290 eV soft X-ray irradiation. BL07A proved useful for studying selective excitation reactions in the soft X-ray region.

References

[1] K. Kanda, Y. Haruyama, M. Fujisawa, S. Matsui: *Nucl. Instrum. Meth. A*. **467-468**, 500-503 (2001).

[2] C. Donnet, M. Belin, J.C. Augé, J.M. Martin, A. Grill, and V. Patel: *Surf. Coat. Technol.* **68-69**, 626 (1994).

[3] K. Kanda, K. Yokota, M. Tagawa, M. Tode, Y. Teraoka, S. Matsui: J. Appl. Phys. **50**, 055801 (2011).

[4] K. Kanda, R. Imai, S. Tanaka, S. Suzuki, M. Niibe, T. Hasegawa, T. Suzuki, H. Akasaka: *Materials*. **14**, 924 (2021).

[5] M. Okui, A. Shimoguchi, N. Yato, N. Murayama, I. Kikuchi, I. Tsuboki, K. Kanda: *Journal of Physics*. **2380**, 012054 (2022).

[6] S. Tanaka, S. Suzuki, T. Mishima, K. Kanda: *J. Synchrotron Rad.* **28**, 618-623 (2021).

Magnetic field correction of NewSUBARU short undulator (SU) and creation of peak energy prediction program with gap table

Tomohiro Mishima[1], and Kazuhiro Kanda[1]

[1]Laboratory of Advanced Science and Technology for Industry (LASTI), University of Hyogo

Abstract

The actual magnetic field strength of the BL07 undulator was determined from the analysis on undulator spectrum measured at BL07B and the actual electron storage energy at 1.0 GeV operation. Using the determined magnetic field strength, the program to predict the energy of the harmonic light from the undulator gap length at both 1.0 GeV and 1.5 GeV operation has been created. This program was already used by BL07A users for experiments.

1. Introduction

BL07A is a beamline designed to create functional materials by surface modification using soft X-ray irradiation.[1] At BL07, the light supplied from undulator is introduced into BL07A and BL07B by a switching mirror. The undulator of BL07 is a 3 m short planar type undulator (SU) consisting of 28 cycles of permanent magnets with a period length of 76 mm. BL07A is equipped with a multilayer mirror monochromator for monochromatic light irradiation, which is suitable for cutting out one harmonic of undulator light.[2] By using an undulator and a multilayer mirror monochromator, a sample at the irradiation position of BL07A can be irradiated with about 10^{14} photons/cm^2 between 50 eV ~ 400 eV and about 10^{13} photons/cm^2 between 400 eV ~ 800 eV.[3] On the other hand, multilayer mirror monochromator is low energy resolution, because it can provide high-brightness light. Therefore, the exact spectral wavelength cannot be determined at this beamline, and the energy of each harmonic of the undulator light must be predicted from the undulator gap.

The high-resolution spectra can be measured at BL07B, which is mounted a grating monochromator and undulator light is supplied from the same SU as BL07A. We developed a program to calculate the undulator light energy from the undulator gap length for 1.0 GeV and 1.5 GeV operation, using undulation spectra measured at BL07B, which Dr. Yuichi Haruyama provided us.

2. Undulator Principle

Consider the following magnetic field with sin-type variation in the vertical direction as the periodic static magnetic field of an undulator, and consider the motion of electrons incident in the z-axis direction.[4]

$$\boldsymbol{H} = -\boldsymbol{e_y} H_0 sin\left(\frac{2\pi z}{\lambda_u}\right) \tag{1}$$

(e_y : unit vector along y-axis H_0 : strongest magnetic field in y-axis direction)

Solving the equation of motion (2) for an electron in a magnetic field in equation (1) yields (3), (4) as the solution for electron β and position r.

$$\frac{d\boldsymbol{p}}{dt} = -e\boldsymbol{\beta} \times \boldsymbol{H} \tag{2}$$

($p = \gamma m\boldsymbol{v} = \gamma mc\boldsymbol{\beta}$ γ : Lorenz factor)

$$\boldsymbol{\beta} = \boldsymbol{e}_x \frac{K\beta}{\gamma} cos(\omega 0t') + \boldsymbol{e}_z \beta \left[1 - \frac{K^2}{4\gamma^2} - \frac{K^2 cos(2\omega 0t')}{4\gamma^2}\right] \tag{3}$$

$$\boldsymbol{r} = \boldsymbol{e}_x \frac{K\lambda_u}{2\pi\gamma} sin(\omega 0t') + \boldsymbol{e}_z \left[\left\{1 - \frac{K^2}{4\gamma^2}\right\}\beta ct' - \frac{K^2\lambda^u sin(2\omega 0t')}{16\pi\gamma^2}\right] \tag{4}$$

(e_x : unit vector along x-axis, e_z : unit vector along z-axis)

$(\omega_0 = 2\pi c\beta \frac{1 - K^2/4\gamma^2}{\lambda_u})$

K in equations (3) and (4) is a parameter corresponding to the maximum bending angle of the electron orbit, called the deflection constant, and is expressed as

$$K = \frac{eH_0\lambda_u}{2\pi mc^2} = 0.934B_0(T)\lambda_u \tag{5}$$

($B_0(T)$: Maximum flux density corresponding to H_0 λ_u : Magnetic field periodic length = 0.76 [m])

For the NewSUBARU BL07 undulator, the undulator gap dependence of B_0(T) and K from the magnetic field measurement data can be approximated by the following equation.

$$B_0(T) = 2.064 \times exp\left(-\frac{\pi g}{\lambda_u}\right) \tag{6}$$

$$K = 14.654 \times exp\left(-\frac{\pi g}{\lambda_u}\right) \tag{7}$$

(g : length of gap [m])

The relation between undulator light energy and gap length was obtained from equation (7) and the following equation.

$$\gamma = 1 + \frac{E}{m_e c^2} \tag{8}$$

$$W_1 = \left(1 + \frac{K^2}{2}\right) \times \frac{\lambda}{2\gamma^2} \tag{9}$$

$$E_1 = \frac{1}{W_1 \times 100 \times 8065.541} \tag{10}$$

(E : storage electron energy W_1 : wavelength of primary light
E_1 : peak energy of primary light)

3. Results and Conclusion

NewSUBARU is operated in two type modes of operation: 1.0 GeV operation and 1.5 GeV operation. The actual electron storage energy for 1.0 GeV operation was obtained as 0.974 GeV by Dr. Shuji Miyamoto's laser Compton backscattering experiments,[5] but the actual electron energy for 1.5 GeV operation has not yet been reported.

Figures 1 and 2 show the relation between the undulator gap and the peak energy of each order of light at 1.0 GeV operation. The dotted line is the value calculated by the above formula, and the solid line is the value of the undulator spectrum actually measured at BL07B. From Figure 1, it was found that the dotted and solid lines are out of alignment. Therefore, we corrected the misalignment by applying a zero-order correction to the coefficient 14.654 in Equation (7). As a result, as shown in Figure 2, the coefficient of 13.855 in equation (7) was the smallest deviation.

Figures 3 and 4 show the relationship between the undulator gap and the peak energy of each order light at 1.5 GeV operation. The dotted line in Fig. 3 is calculated by the above formula with the coefficient of Eq. (7) as 13.855 and the electron storage energy as 1.5 GeV, and the solid line is the value of the undulator spectra measured at BL07B. From Figure 3, it is found that the dotted line and the solid line are out of alignment. Here, we corrected the discrepancy between the dotted and solid lines by applying a zero-order

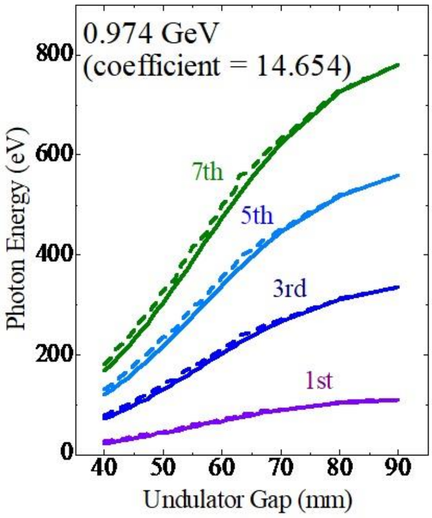

Figure 1. Relationship between undulator gap and peak energy of each order light at 1.0 GeV operation (before correction).

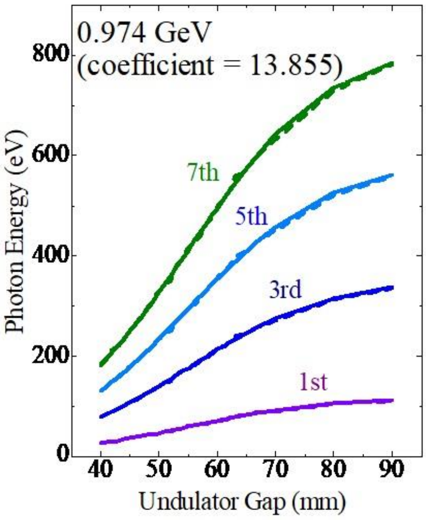

Figure 2. Relationship between undulator gap and peak energy of each order light at 1.0 GeV operation (after correction).

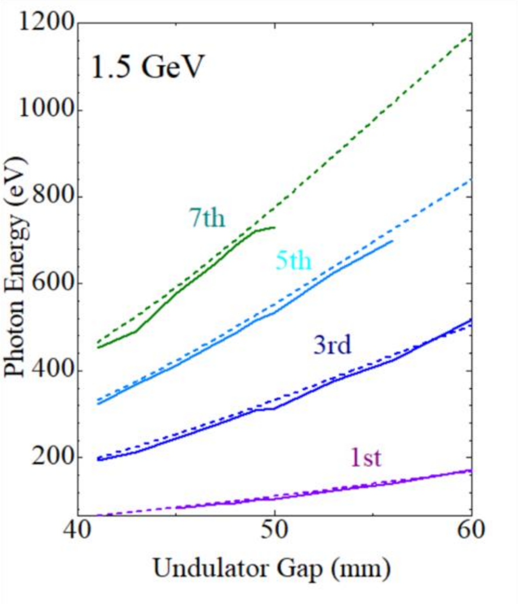

Figure 3. Relationship between undulator gap and peak energy of each order light at 1.5 GeV operation (before correction).

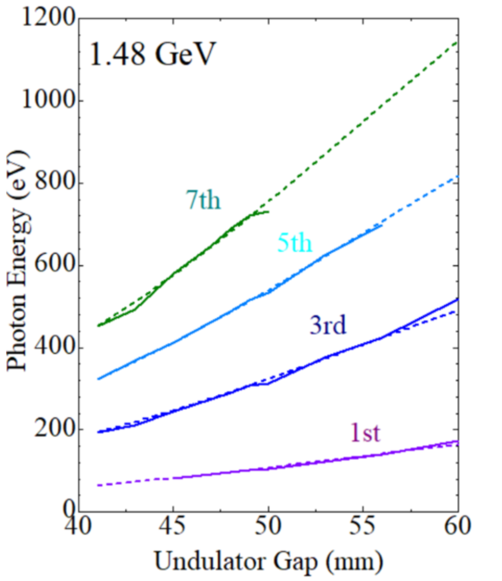

Figure 4. Relationship between undulator gap and peak energy of each order light at 1.5 GeV operation (after correction).

correction to the electron storage energy (E) in Eq. As shown in Figure 4, the case with 1.48 GeV had the smallest deviation. It is clear that the above correction lowered the coefficient in equation (7) for obtaining the K value from 14.654 to 13.855. This indicates that the magnetic field strength of the SU has decreased. Using this result, a program was created to calculate the peak energies of the 1st, 3rd, 5th, and 7th order photons by inputting the gap length and a program to calculate the gap length from the peak energy.

Acknowledgement

Dr. Yuichi Haruyama of the Laboratory of Advanced Science and Technology for Industry, University of Hyogo provided the data on BL07 undulator spectra measured at BL07B.

Dr. Shuji Miyamoto of the Laboratory of Advanced Science and Technology for Industry, University of Hyogo provided the data on the actual electron energy for 1.0 GeV operation at NewSUBARU.

References

[1] K. Kanda, Y. Haruyama, M. Fujisawa, S. Matsui: *NIMA*. **467-468**, 500-503 (2001).
[2] M. Okui, A. Shimoguchi, N. Yato, N. Murayama, I. Kikuchi, I. Tsuboki, K. Kanda: *Journal of Physics.* **2380**, 012054 (2022).
[3] S. Tanaka, S. Suzuki, T. Mishima, K. Kanda: *J. Synchrotron Rad.* **28**, 618-623 (2021).
[4] H. Ooyanagi: *Fundamentals of Synchrotron Radiation*, Maruzen Publishing (1996).
[5] S. Miyamoto, H. Utsunomiya, T. Shima and S. Amano: *SPring-8 Research Frontiers 2013*, 153-154 (2014).

Effect of Photon Energy on the Reduction of Graphene Oxide by Soft X-ray Irradiation

Akira Heya[1], Akinori Fujibuchi[1], Masahiro Hirata[1], Kazuhiro Kanda[2], Yoshiaki Matsuo[3], Junichi Inamoto[3], and Koji Sumitomo[1]

[1] *Department of Materials and Synchrotron Radiation Engineering, University of Hyogo*
[2] *Laboratory of Advanced Science and Technology for Industry (LASTI), University of Hyogo*
[3] *Department of Applied Chemistry and Chemical Engineering, University of Hyogo*

Abstract

The photon-energy dependence of reduction of graphene oxide (GO) through soft X-ray irradiation was investigated using photon energies of 300 eV for C 1s core electron excitation and 550 eV for O 1s core electron excitation. GO was reduced by soft X-ray irradiation at 150 °C (300 eV) and at 60 °C (550 eV). The O-related peaks such as C-O-C in GO after soft X-ray irradiation were smaller at 550 eV than at 300 eV. This indicates that the excitation of the core-shell electrons of O enhances the reduction of GO. It was found that the soft X-ray irradiation depends on the photon energy, in other words, the difference between C 1s and O 1s electron excitation.

1. Introduction

The reduction of graphene oxide (GO) is a promising low-cost method for fabricating graphene field-effect transistors (FETs)[1] and sensors[2]. However, the electrical property of reduced GO is degraded compared to those of ideal graphene due to defects introduced during reduction.

Soft X-ray irradiation to reduce GO is often used, and it has been reported that the X-ray induced reduction process is initiated by photo- and secondary electrons.[3,4] Our group has investigated the reductions of GO using soft x-rays and combined atomic hydrogen annealing (AHA) and x-ray methods.[5] In the soft X-ray reduction, to excite the C 1s core electron at 284.6 eV, the soft X-ray of 300 eV was irradiated with GO film. However, functional groups such as C-O-C and O=C-OH remain after soft X-ray irradiation. In contrast, the excitation of the O 1s core electron at 532 eV might promote the GO reduction.

In this study, to enhance the GO reduction, the O 1s core electron at 532 eV was excited by soft X-ray of 550 eV. The mechanism of GO reduction by soft X-ray irradiation was discussed from the comparison between 300 and 550 eV.

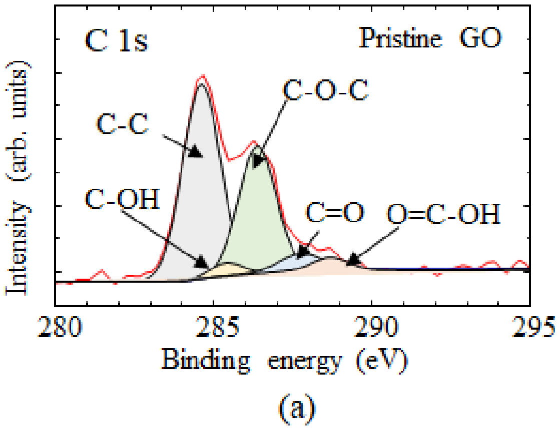

(a)

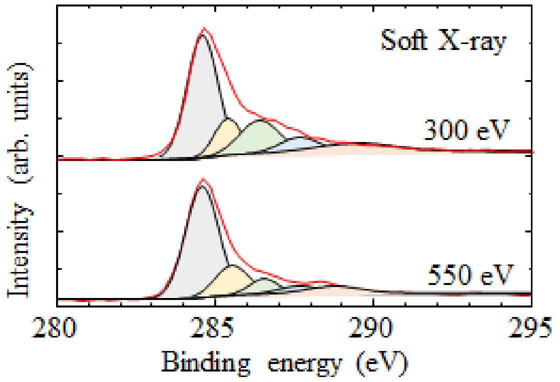

(b)

Figure 1. C 1s XPS spectra of the pristine GO (a) and soft X-ray irradiated GO (b). The C 1s spectrum are decomposed to five peaks.

2. Experimental

Individual GO sheets were prepared from natural graphite flakes with large grain sizes (～100 μm) based on the Brodie's method. A 5 mm × 5 mm array of circular wells with diameters of 1, 2, 4, and 8 μm, named microwell (MW) substrate, was used for application to suspended graphene FETs. The GO dispersed in 0.1 mL of solvent (0.006 mg/mL) was dropped onto the cleaned MW substrate on a hot plate at 150 °C.

The irradiation of soft X-rays was performed at BL07A of NewSUBARU.[6] The light source of BL07A was a 2.28 m undulator. The electron energy of the storage ring was 1 GeV during the experiments. The main photon energies were 300 and 550 eV. However, the soft X-ray irradiation was carried out without a monochromator to select the photon energy. Therefore, the irradiated light also had higher-order X-rays with lower photon density than the main photon energy. The irradiation duration was 3600 s. The storage-ring current and dose were 350 mA and 350 mA·h, respectively. The saturated sample temperatures during irradiation at 300 and 550 eV were 150 and 60 °C, respectively.

The surface property was evaluated using X-ray photoelectron spectroscopy (XPS). For XPS (ULVAC-PHI, PHI 5000Versaprobe), an energy step of 0.2 eV, pass energies of 23.5 eV, dwell times of 100 ms, and integration of 10 times were used. A neutralizer gun was used to suppress the charge. The binding energy was corrected by using C-C bond peak as a 284.6 eV.

3. Results and Discussion

The C 1s XPS spectra of the pristine GO and soft X-ray irradiated GO are shown in Fig. 1. The C 1s spectrum consists of five peaks: C–C (284.6 eV), C–OH (285.5 eV), C–O–C (286.6 eV), C=O (287.5 eV), and O=C–OH (288.9 eV).[7] To compare 300 eV and 550 eV, the C 1s peak was decomposed to five peaks. The C-O-C peak at 286.6 eV was reduced by soft X-ray irradiation. However, the C 1s spectra were different in the region of C-OH, C-O-C, C=O, and O=C-OH peaks. The peak area ratios of C–OH, C–O–C, C=O, and O=C–OH bonds estimated from the C 1s spectra at various treatments are shown in Fig. 2(a). The C–O/C–C ratio of the pristine GO, the soft X-ray irradiated GO are shown in Fig. 2(b). In this case, the C-C peak area was obtained from the peak at 284.6 eV and the C-O peak area was the sum of C-OH, C-O-C, C=O, and O=C-OH peaks.

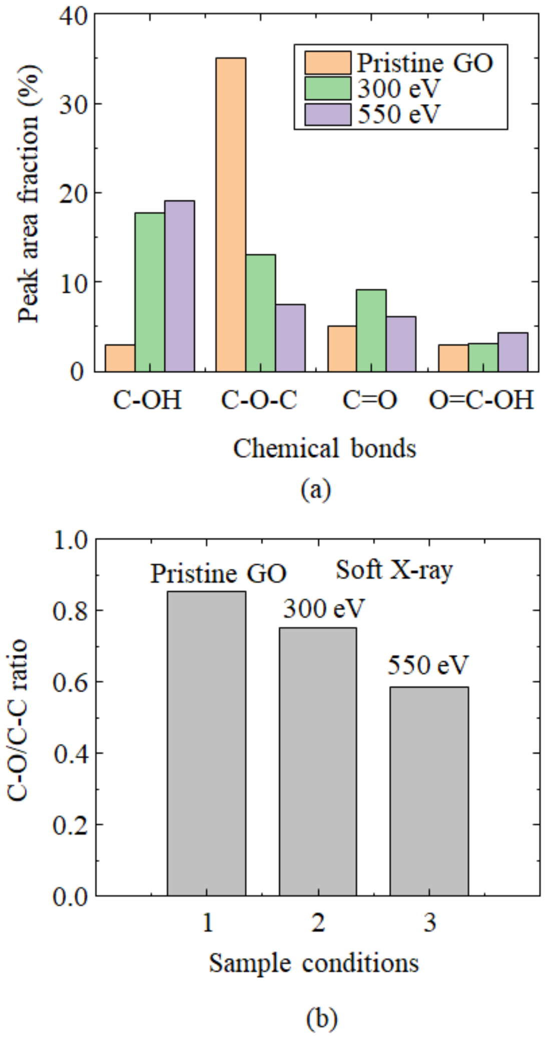

Figure 2. (a) Peak area fraction of the C–OH, C–O–C, C=O, and O=C–OH bonds estimated from C 1s spectra. (b) C–O/C–C ratio of the pristine GO, the soft X-ray irradiated GO.

The peak area ratios of the C–O–C and C=O at 550 eV were smaller than that at 300 eV. In contrast, the C-OH and O=C-OH at 550 eV were larger than that at 300 eV. The C-O/C-C ratio were 0.75 and 0.59 at 300 and 550 eV, respectively. and reduced by 22 % by using a photon energy of 550 eV corresponding to O 1s core electrons. It was confirmed that GO was reduced more at 550 eV than at 300 eV.

The difference in interaction of soft X-ray with core electrons between 300 and 550 eV is discussed based on the effect of resonant Auger electrons.[8] The electron excitation from C 1s and/or O 1s and the behavior of the electron are shown in Fig. 3. As GO absorbs soft X-rays of 300 eV, the core-shell electrons of C 1s are excited into an unoccupied orbital (σ^*), referred to as spectator electron. The spectator electron in the valence band then transfers to the C 1s core level. Auger electrons emit from the sample surface into vacuum. On the other hand, when the GO absorbs soft X-rays of 550 eV, the core-shell electrons of not only C 1s but also O 1s are emitted from the sample surface into vacuum. This suggests that the reduction of terminal groups such as C-O-C in GO is facilitated by the simultaneous action of excitation of both C and O core-shell electrons.

The speculated reduction mechanism due to the soft X-ray irradiation is shown in Fig. 4. In the Figure,

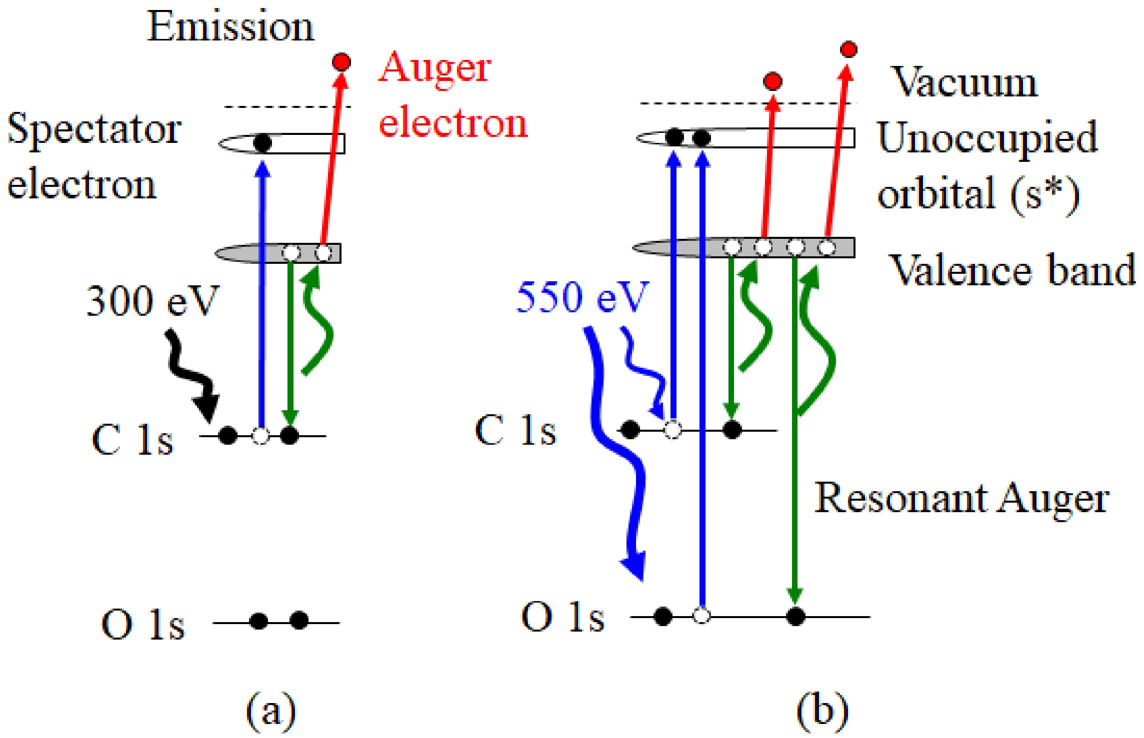

Figure 3. Electron excitation from C 1s and O 1s, and the behavior of electron.

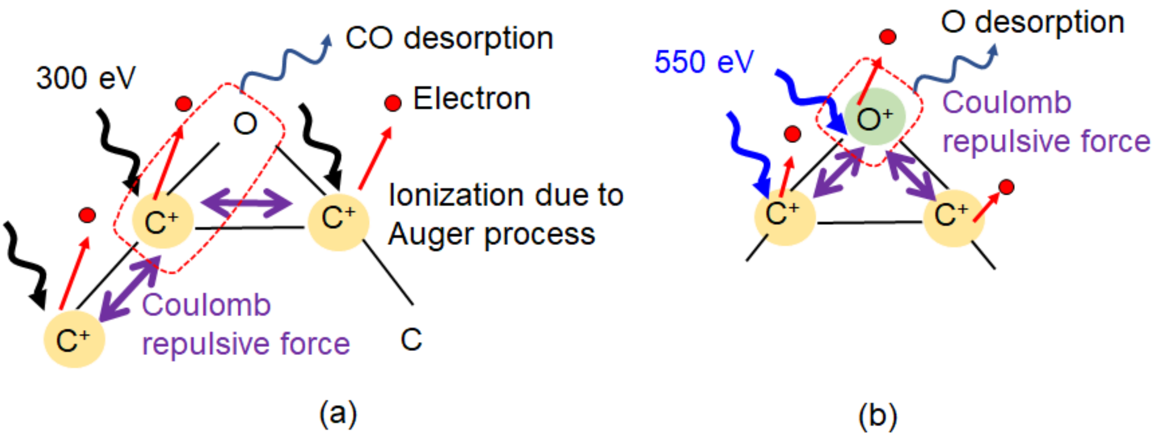

Figure 4. The speculated reduction mechanism due to soft X-ray irradiation.

we focus on the C-O-C of the main bond. As the C and O atoms absorbs soft X-ray, the ionization occurs. As the neighbor atom is also ionized, a Coulomb repulsive force is generated. The repulsive force enhances the bond breaking. At 300 eV, CO is desorbed in breaking the C-C bond. On the other hand, at 550 eV, the C and O atoms are ionized simultaneously. In this case, the O atom is desorbed. Since the ionization of O as well as C is realized at 550 eV, the reduction of GO occurs more at 550 eV than at 300 eV.

As mentioned, the change in XPS spectra indicates that the C-O-C changed to C-OH. The following reactions are considered.

$$\text{C-O-C} + h\nu\ (300\ \text{eV}) \rightarrow \text{C-} + \text{CO}\uparrow, \qquad (1)$$

$$\text{C-O-C} + h\nu\ (550\ \text{eV}) \rightarrow 2\text{C-} + \text{O}\uparrow, \qquad (2)$$

$$\text{C-} + \text{H}_2\text{O} \rightarrow \text{C-OH} + \text{H}. \qquad (3)$$

The increase in the C–OH peak after the soft X-ray irradiation is related to the generation of dangling bonds (C-) in the r-GO flakes. The C–OH generation is attributed to the reaction with H_2O in air, which occurs at the dangling bonds during air exposure.

4. Conclusion

GO was reduced by soft X-ray irradiation at 150 °C (300 eV) and at 60 °C (550 eV). The GO was reduced more at 550 eV than at 300 eV. The excitation of the core-shell electrons of O enhanced the reduction of GO. The C-C and C-O bonds preferentially broke by soft X-rays of 300 and 550 eV, respectively.

Acknowledgement

The authors are grateful to Dr. A. Oshima of NTT Basic Research Laboratories for the supply of the MW substrates. This work was supported by JSPS KAKENHI Grant Number JP22K04877.

References

[1] D.-J. Kim, Y. Sohn, J.-H. Jung, O. J. Yoon, N-E Lee, J.-S. Park: *Biosens. Bioelectron*. **41**, 621 (2013).

[2] K. Lee, Y. K. Yoo, M.-S. Chae, K.S. Hwang, J. Lee, H. Kim, D. H. and J. H. Lee: *Sci. Rep.,* **9**, 10297 (2019).

[3] C.-Y. Lin, C.-E. Cheng, S. Wang, H. W. Shiu, L. Y. Chang, C.-H. Chen, T.-W. Lin, C.-S. Chang, and F. S.-S. Chien: *J. Phys. Chem. C*, **119**, 12910 (2015).

[4] V. M. Mikoushkin, A. S. Kriukov, S. Yu. Nikonov, A. T. Dideikin, A. Ya. Vul, and O. Yu. Vilkov: *J. Appl. Phys.*, **124**, 175303 (2018).

[5] A. Heya, A. Fujibuchi, M. Hirata, K. Kanda, Y. Matsuo, J. Inamoto, and K. Sumitomo: *Jpn. J. Appl. Phys.*, **62**, SC1028 (2023).

[6] A. Heya, T. Oonuki, R. Utimi, K. Kanda, R. Yamasaki, and K. Sumitomo: *Thin Solid Films* **713**, 138365 (2020).

[7] O.-K. Park, M. G. Hahm, S. Lee, H.-I. Joh, S.-I. Na, R. Vajtai, J. H. Lee, B.-C. Ku, and P. M. Ajayan: *Nano Lett.*, **12**, 1789 (2012).

[8] K. Tanaka H. Kizaki, R. Sumii, Y. Matsumoto, and S. Wada: *Radiat. Phys. Chem.*, **75**, 2076 (2006).

Effect of Atomic Hydrogen Exposure on Hydrogen-Free Amorphous Carbon Films

Yuichi Haruyama[1], Daiki Morimoto[1], Akira Heya[2], Koji Sumitomo[2], Noriaki Toyoda[2], and Seigo Ito[2]

[1]*Laboratory of Advanced Science and Technology for Industry (LASTI), University of Hyogo*
[2]*Graduate School of Engineering, University of Hyogo*

Abstract

The effect of atomic hydrogen exposure on hydrogen-free amorphous carbon films was investigated by a soft X-ray photoelectron spectroscopy. From the dependence of the C 1s photoelectron spectra of hydrogen-free amorphous carbon films on atomic hydrogen exposure, it was shown that the contents of the *sp*^{3} hybridized and the C-H bonded carbon atoms increased remarkably after atomic hydrogen exposure. In addition, the surface coordination of C atoms in the hydrogen-free amorphous carbon films after atomic hydrogen exposure was investigated from the photoelectron emission angle dependence. It was found that the *sp*^{3} C atoms were dominant at the surface of hydrogen-free amorphous carbon films after atomic hydrogen exposure.

1. Introduction

Since amorphous carbon films have interesting properties such as high hardness and a low friction coefficient, they have been expected to be used as lubrication materials in space[1]. The properties of amorphous carbon films have been related with not only *sp*^{2}/*sp*^{3} ratio but also hydrogen contents in films[2]. It is reported that amorphous carbon films are etched in the atomic hydrogen exposure and the etching rate is depending on the hydrogen contents in films[3]. In addition, it is also reported that the coordination of the carbon atoms in the hydrogenated amorphous carbon films is unchanged in the atomic hydrogen exposure[4]. As the systematic investigation of atomic hydrogen exposure on the amorphous carbon films is important, the effect of atomic hydrogen exposure on the hydrogen-free amorphous carbon films was investigated by a soft X-ray photoelectron spectroscopy.

2. Experimental

Hydrogen-free amorphous carbon films were produced by the gas cluster ion beam method[5]. Atomic hydrogen was generated using a hot filament method[3,4]. W mesh composed of 0.03 mmφ wire at a density of 30 wires per inch was used as the filament and heated at a temperature of about 1700 °C. An Ar (95 %) and H_2 (5 %) gas mixture at a pressure of 10 Pa and flow rate of 100 sccm was used to produce the atomic hydrogen. During atomic hydrogen exposure, the sample temperature measured by a type-K thermocouple was kept below 40 °C by use of a water-cooled sample holder. The distance between the sample and W mesh was 150 mm. Since the atomic hydrogen generation apparatus was connected to the photoelectron analysis chamber through a gate valve, photoelectron spectroscopy spectra after atomic hydrogen exposure were measured without exposing them to air. Photoelectron measurements were carried out at the beamline 7B of NewSUBARU synchrotron radiation facility, University of Hyogo.

3. Results and Discussion

The C 1s core-level photoelectron spectrum of the hydrogen-free amorphous carbon film after atomic hydrogen exposure is compared with that before atomic hydrogen exposure in Figure 1. Although the peak was located at 284.4 eV before exposure, it shifted at 285.2 eV after hydrogen exposure. In addition, the width of the peak became narrower and the spectral feature changed symmetric line shape after atomic hydrogen exposure. The component at 284.4 eV was assigned to the C 1s electrons originating from the *sp*^{2} hybridized carbon atoms while the component at 285.2 eV was assigned to the C 1s electrons originating from the *sp*^{3} hybridized and the C-H bonded carbon atoms[5]. Therefore, it was observed that the contents of the *sp*^{3} hybridized and the C-H bonded carbon atoms increased remarkably after atomic hydrogen exposure. In the case of the hydrogenated amorphous carbon films[4], no change in the spectral features of the C 1s core-level photoelectron spectrum was observed from the atomic hydrogen exposure dependence. This indicates that the coordination of C atoms in the hydrogenated amorphous carbon film is not influenced by atomic hydrogen exposure. Thus, we obtained the different results, depending on the contents of the hydrogen in amorphous carbon films.

Figure 2 shows the photoelectron emission angle dependence of C 1s spectra after atomic hydrogen exposure on the hydrogen-free amorphous carbon film. With increasing photoelectron emission angle, the peak at 284.6 eV decreased while the spectral feature of the main peak at 285.2 eV remained unchanged. This indicates that the concentration of the *sp*^{2} C atoms increased with the depth and the *sp*^{3} C atoms are dominant in the surface of the hydrogen-free amorphous carbon film.

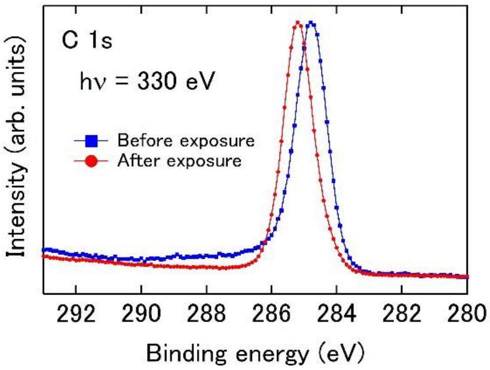

Figure 1. C 1s photoelectron spectra of the hydrogen-free amorphous carbon film before and after atomic hydrogen exposure.

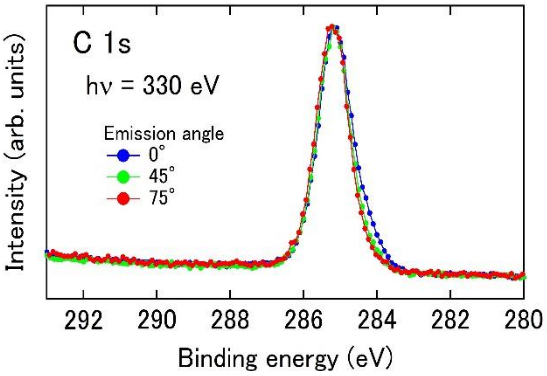

Figure 2. C 1s photoelectron spectra of the hydrogen-free amorphous carbon film as a function of the photoelectron emission angle.

4. Conclusion

We investigated the effect of atomic hydrogen exposure on hydrogen-free amorphous carbon films was by using a soft X-ray photoelectron spectroscopy. The coordination of carbon atoms in hydrogen-free amorphous carbon films was found to be affected by atomic hydrogen exposure while that in hydrogenated amorphous carbon films was unaffected by atomic hydrogen exposure. Thus, we obtained the different results, depending on the contents of the hydrogen in amorphous carbon films. After atomic hydrogen exposure for hydrogen-free amorphous carbon films, the *sp*^{3} carbon atoms was dominant at the surface. In addition, it was observed that the content of the *sp*^{2} carbon atoms increased with the depth.

References

[1] J. Robertson: *Surf. Coat. Tech.* **50**, 185 (1992).
[2] C. Lenardi, P. Piseri, V. Briois, C. E. Bottani, A. Li Bassi, P. Milani: *J. Appl. Phys.* **85**, 7159 (1999).
[3] A. Heya, T. Harada, M. Niibe, K. Sumitomo, T. Watanabe: *J. Photopolymer Sci.* and Tech. **33**, 419, (2020).
[4] Y. Haruyama, D. Morimoto, A. Heya, K. Sumitomo, S. Ito, K. Yokota, M. Tagawa: *Jpn. J. Appl. Phys.* **60**, 125504 (2021).
[5] Y. Haruyama, T. Kitagawa, K. Kanda, S. Matsui, T. Gejo, N. Toyoda, I. Yamada: *Jpn. J. Appl. Phys.* **47**, 3380 (2008).

Ultraviolet photoelectron spectroscopy study on d band center of Co and Ir catalyst particle

Takahiro Maruyama[1, 2], and Yuichi Haruyama[3, 4]

[1]*Department of Applied Chemistry, Faculty of Science and Technology, Meijo University*
[2]*Nanomaterial Research Center, Meijo University*
[3]*Laboratory of Advanced Science and Technology for Industry, University of Hyogo*
[4]*Department of Materials and Synchrotron Radiation Engineering, Graduate School of Engineering, University of Hyogo*

Abstract

Co and Ir are efficient catalysts for single-walled carbon nanotube (SWCNT) growth, but the optimal temperature for SWCNT growth with an Ir catalyst is above 800°C, which is much higher than that with a Co catalyst. Here, we investigated the energy levels of d band centers of Co and Ir nanoparticles by using ultraviolet photoelectron spectroscopy (UPS). Our result showed that the d band center of Co 3d level is ~0.8 eV lower than that of Ir 5d level. We consider that the wide temperature range of SWCNT growth with a Co catalyst is related to the lower binding energy of d band center of a Co catalyst.

1. Introduction

Single-walled carbon nanotubes (SWCNTs) [1] have been expected for various applications in many fields because they exhibit excellent properties. At present, chemical vapor deposition (CVD) is widely used for SWCNT growth because of both its capacity for mass production and its cost-effectiveness. So far, many groups reported growth of vertically aligned SWCNTs (VA-SWCNTs), so called, “SWCNT forests”, with Fe and Co catalysts [2]. Recently we reported VA-SWCNT growth by alcohol catalytic CVD (ACCVD) with an Ir catalyst [3]. However, the optimal temperature region for SWCNT growth with an Ir catalyst was above 800°C, which is much higher than that with iron-group metal catalysts.

In this study, we performed ultraviolet photoelectron spectroscopy (UPS) for Co and Ir catalysts to investigate their valence band structures, which are strongly related to the catalyst activity.

2. Experimental

Co and Ir particles were deposited on Al_2O_3/Si and SiO_2(100 nm)/Si substrates, respectively, by using the pulsed arc plasma deposition method in a high vacuum. This is because SWCNT forests were obtained from Co catalysts deposited on Al_2O_3/Si substrates, while SWCNT forests were grown from Ir catalysts on SiO_2/Si substrates. The particle sizes were mainly distributed between 1 and 3 nm. The samples were mounted in the sample preparation chamber of the end station of BL7B at NewSUBARU synchrotron light facility. After hydrogen treatments for cleaning the sample surface, they were transformed into the analysis chamber, and UPS measurements were performed at room temperature. For reference, we measured UPS spectra for Al_2O_3/Si and SiO_2/Si substrates with no catalyst particles under the same excitation energy.

3. Results and Discussion

Fig. 1(a) and (b) shows valence band spectra of Co and Ir catalysts which were deposited on Al_2O_3/Si and SiO_2/Si substrates, respectively. The excitation energies used for UPS measurements were 58 and 70 eV for Co/Al_2O_3/Si and Ir/SiO_2/Si substrates, respectively. For comparison, the spectra of Al_2O_3/Si and SiO_2/Si substrates with no catalysts are also shown, as black lines. In the spectra of Co/Al_2O_3/Si and Ir/SiO_2/Si substrates, weak structures appeared below the Fermi levels, as shown with black arrows. These structures are derived from the Co 3d band and Ir 5d band, respectively. To show the 3d and 5d derived bands clear, the differential spectrum between the Co/Al_2O_3/Si and Al_2O_3/Si and that between Ir/SiO_2/Si and SiO_2/Si are shown in the insets of Fig. 1(a) and (b). For Ir catalysts, one weak peak was seen at ~3.8 eV below the Fermi level, corresponding to Ir 5d band. In the case of Co catalysts, two structures were seen at ~2.2 and ~5.0 eV below the Fermi level. Farkaš et al. reported that the energy separation between the 3d spin-up and spin-down electrons of Co clusters was ~2.7 eV [4]. Therefore, we consider that the two structures observed in the in set of Fig. 9(a) corresponds to the energy bands of the up- and down-spin electrons of Co catalyst particles. From the differential spectra, we estimated the position of d band center of Co and Ir catalysts

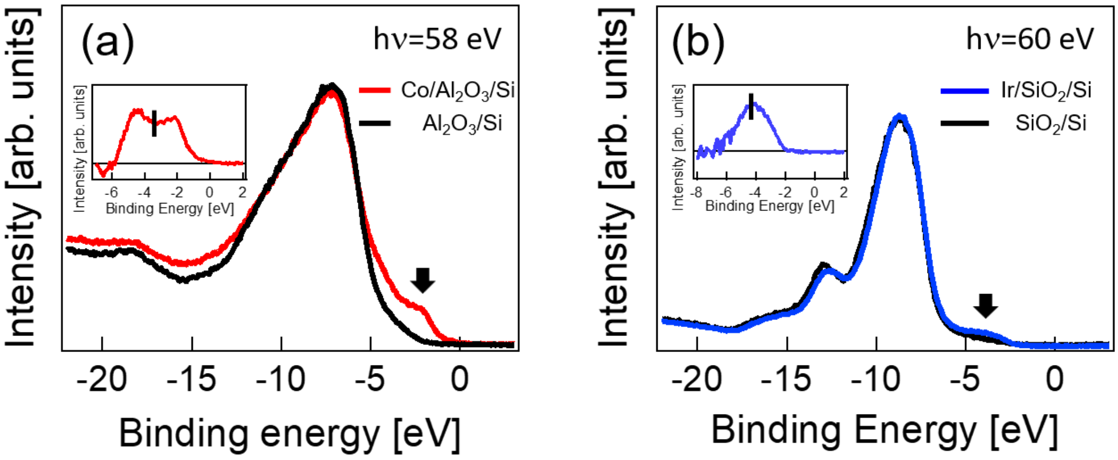

Figure 1. UPS spectra of (a) Co/Al$_2$O$_3$/Si and (b) Ir/SiO$_2$/Si samples. For comparison, UPS spectra of Al$_2$O$_3$/Si and SiO$_2$/Si samples are shown in (a) and (b) respectively, by black lines. The differential spectra between Co/Al$_2$O$_3$/Si and Al$_2$O$_3$/Si samples, and between Ir/SiO$_2$/Si and SiO$_2$/Si samples are shown in the insets of (a) and (b), respectively. The d band center position of Co 3d and Ir 5d are shown with vertical bars in the insets.

because the d band center is strongly related to the dissociation reaction process of feedstock gas. The d band center of Co 3d was ~3.42 eV below the Fermi level, while that of Ir 5d was ~4.22 eV. This indicates that the d band center of Co catalyst particles was ~0.8 eV lower than that of 5d band of Ir catalysts.

Previously, Wang et al. performed ab initio density functional theory (DFT) simulation for ethanol decomposition reaction on (111) surface of various transition metals [5]. Assuming various reaction pathways, they investigated a dissociation barrier for each reaction pathway, and pointed out that the overall dissociation barriers decrease as the energy level of d band center of a metal approaches the Fermi level. Our UPS result showed that the d band center of Co 3d level was ~0.8 eV closer to the Fermi level. We consider that such a lower binding energy of d band center of 3d level of Co catalyst particles leads to the lower dissociation barrier in the reaction of ethanol molecules on Co catalysts, resulting in the wide temperature range for SWCNT growth.

4. Conclusion

We investigated the d band centers of Co and Ir catalysts particles by UPS measurements. We found that the d band center of Co 3d level was ~0.8 eV closer to the Fermi level, compared with that of Ir 5d level. Such a low energy position of Co 3d level would lead to the high efficiency of feedstock decomposition, resulting in the wide temperature range of SWCNT growth by ACCVD.

Acknowledgement

This work was partly supported by JSPS KAKENHI (grant number 19H02563) and was also partly supported by Meijo University Nanomaterial Research Center.

References

[1] S. Iijima, and T. Ichihashi: *Nature*, **363**, 603 (1993).
[2] H. Ohno, D. Takagi, K. Yamada, S. Chiashi, A. Tokura, and Y. Homma: *Jpn. J. Appl. Phys.*, 47, 1956 (2008).
[3] T. Maruyama, T. Okada, K.P. Sharma, T. Suzuki, T. Saida, S. Naritsuka, Y. Iizumi, T. Okazaki, and S. Iijima: *Appl. Surf. Sci.*, **509**, 145340 (2020).
[4] B. Farkaš, U. Terranova, and N.H. de Leeuw: *Phys. Chem. Chem. Phys.*, **22**, 985 (2020).
[5] J. J. Wang, C. S. Lee, and M. C. Lin: *J. Phys. Chem.* C, **113**, 6681 (2009).

NEXAFS Studies of Amorphous Carbon Nitride Thin Films Deposited by Pressure-gradient RF Magnetron Sputtering

Masami Aono[1], Kyoji Morita[2], Tasuku Inoue[2], and Kazuhiro Kanda[3]
[1] *Department of Electrical and Electronics Engineering, Graduate School of Science and Engineering, Kagoshima University,*
[2]*Faculty of Engineering, University of Hyogo*
[3]*Laboratory of Advanced Science and Technology for Industry (LASTI), University of Hyogo*

Abstract

Amorphous carbon nitride (a-CN$_x$) thin films were deposited through radio frequency (RF) magnetron sputtering under increasing nitrogen gas pressure around a graphite target to provide nitrogen radicals at high concentrations. The C *K*-edge near-edge X-ray absorption fine structure (NEXAFS) measurements were performed at NewSUBARU BL09A. To increase the gas pressure around the graphite target, C *K*-edge NEXAFS spectra of the a-CN$_x$ films was changed. The nitrogen content in the a-CN$_x$ films obtained from XPS analysis did not increase when the nitrogen gas pressure around the graphite target was increased. The effect of nitrogen incorporation on the a-CN$_x$ films was comparatively more effective at higher RF powers.

1. Introduction

Liu and Cohen discovered a new super-hard material based on theoretical calculations, generating interest in carbon nitride compounds.[1] They predicted β-C_3N_4 based on β-Si_3N_4.[2] However, the growth of this hexagonal crystal structure has not been corroborated, even 30 years after its prediction. Following the prediction of β-C_3N_4, several crystalline structures based on *sp*^{3}C–N have been presented, such as α-C_3N_4 and cubic-C_3N_4.[3] Almost all the carbon nitrides prepared using thin film deposition techniques, such as chemical vapor deposition (CVD), sputtering, and laser ablation, have amorphous phases due to the low thermal stability of *sp*^{3}C–N bonds.

Thin films of amorphous carbon nitride (a-CN$_x$) comprise *sp*^{2}– and *sp*^{3}–hybridized carbon networks. a-CN$_x$ films can be deposited using two typical deposition methods: plasma-enhanced CVD using hydrocarbon gases and sputtering using graphite. NH_3 and N_2 are used as the nitrogen source. The range of nitrogen concentration (x) is wide, depending on the deposition method and condition; however, the maximum x value in most a-CN$_x$ films is approximately 0.5. Furthermore, a-CN$_x$ films deposited using the CVD method have a relatively lower nitrogen concentration and higher *sp*^{3}-C bonds because it contains hydrogen as source material.[4-6] In contrast, a-CN$_x$ films prepared from graphite and N_2 by physical vapor deposition have more *sp*^{2}-C bonds.[7, 8] The nitrogen concentration of the sputtering film depends on the sputtering gas ratio of Ar and N_2.

a-CN$_x$ films can be deposited with a high nitrogen concentration using the nitrogen-radical sputtering method proposed by Nitta *et al.*[9,10] In this method, nitrogen radicals in the glow discharge of nitrogen molecules react well with a carbon target at low energy.[11] This method can produce a higher nitrogen content than other techniques. The x value of a-CN$_x$ films deposited by nitrogen radical sputtering with hydrogen plasma etching is ~0.86.[10]

As essential technique to increase both the nitrogen content and *sp*^{3}C bond in a-CN$_x$ films is increasing the amount of high-energy nitrogen radical species. The mean free path of sputtered species on the growth surface is short under low-vacuum conditions. Therefore, sputtering under higher-vacuum conditions is desirable for the growth of high *sp*^{3}–hybridized carbon films. However, the number of nitrogen radical species is an important factor in increasing the nitrogen content. In the conventional sputtering method, the vacuum inside the growth chamber is uniform, and thus, generating excess nitrogen radicals is difficult. Recently, the pressure gradient sputtering source has been developed for sputtering at a high vacuum with low plasma damage.[12] In magnetron sputtering using a pressure gradient sputtering source, a gas is locally injected near the sputtering target through the pressure gradient sputtering source, and the main vacuum valve connected to the turbo-molecular pump is fully opened. This condition induces a pressure gradient with a high vacuum at the substrate position and a low vacuum around the target. Hence, the production of additional nitrogen radical species around the target can be expected using the pressure gradient sputtering source. In this study, a-CN$_x$ thin films were deposited using the pressure gradient and conventional sputtering modes with the same growth chamber, and the chemical bonding structure of the films was investigated to confirm the effect of nitrogen radicals.

2. Experimental

2.1. Sample Preparation

a-CN_x films were prepared from graphite with a purity of 99.95% and N_2 with a purity of 99.99995%. The substrates used were SiO_2 glass and Si(100), which were cleaned ultrasonically in acetone and ethanol for 15 min each, before loading into the vacuum chamber.

In the sputtering system, the gas inlet can be changed between two modes, the conventional sputtering and pressure gradient modes, by operating valves. In the gas pressure gradient mode (GP), the sputtering gas was injected near the target. Therefore, the gas pressure around the target was approximately one order of magnitude higher than that around the substrate holder. In comparison, the gas pressure in the chamber in the conventional sputtering mode (CS) was kept constant owing to the flow of N_2 gas through the middle of the target and substrate holder.

The base pressure was under 1×10^{-3} Pa. For the film deposition, the N_2 gas flow rate was 3 sccm, and the process pressure was maintained at 16 Pa (measured near the substrate holder). The samples obtained at RF powers of 85, 130, 200, and 300 W by the conventional sputtering mode were denoted by CS85, CS130, CS200 and CS300, respectively; the samples obtained using the gradient-pressure mode were denoted by GP85, GP130, GP200, and GP300, respectively.

2.2. Characterizations

The atomic concentrations of the samples were obtained from the C1s, N1s, O1s, and Si2p core-level peaks using X-ray photoelectron spectroscopy (XPS; Kratos Ultra 1, Shimadzu); Si was derived from the substrate. Monochromatic Al Kα radiation (1486.6 eV) was used as the X-ray source. The pass energy and step size were 40 and 0.05 eV, respectively. The analysis area was 300 μm × 700 μm. In this study, the Ar^+ bombardment etching process was skipped because it could possibly destroy the chemical bonding structure between carbon and nitrogen. The corresponding binding energies were calibrated with the C1s line at 284.5 eV for all cases, which could be assigned to sp^2 graphite like carbon.[13]

Near-edge X-ray absorption fine structure (NEXAFS) spectroscopy is sensitive to the local coordination of the CN structure and a probe of the electronic structure of unoccupied orbitals of carbon. NEXAFS measurements were performed using the BL09A at the NewSUBARU synchrotron facility of the University of Hyogo[14, 15]; the instrument has an 11 m undulator as a light source and a grating monochromator. The electron energy of the storage ring during this study was 1.23 GeV. The samples deposited on a Si substrate were mounted on a copper plate using a carbon conductive tape. The electrons emitted from the sample were detected in the total electron yield (TEY) mode. The NEXAFS spectra of the C K-edge absorption were measured using a grating of 1200 grooves/mm in the range of 275–330 eV. The energy resolution was estimated to be less than 0.5 eV (full width at half maximum).

3. Results and Discussion

Figure 1 shows the nitrogen content (N/C) obtained from the C1s and N1s core level XPS spectra. The GP and CS samples showed a similar N/C tendency as a function of the RF power. An increase in the RF power decreased the nitrogen content of the films in both sputtering modes. GP85 and CS85 have almost the same N/C ratio of 0.66, showing no significant influence of gas pressure around the target. A comparing of GP300 and CS300 indicates that the N/C ratio of GP300 is slightly larger than that of CS300. The slopes of the regression line of the GP and CS samples were 0.4×10^{-3} and 0.5×10^{-3}, respectively. The oxygen content (O/C) of the samples were in the range of 0.09–0.14; the oxygen originates from the surface adsorption of O_2 and H_2O after the deposition.

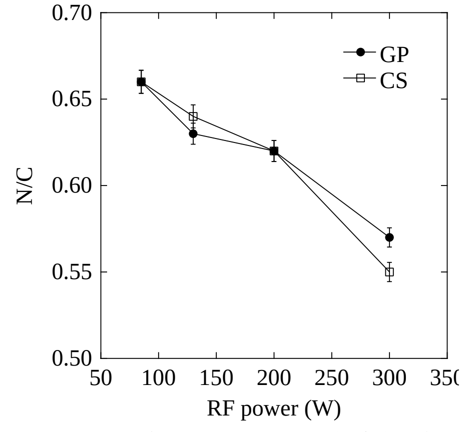

Figure 1. Nitrogen content (N/C) of a-CN_x films deposited using the gradient gas pressure (GP) and common sputtering (CS) modes.[23]

Figures 2 shows the TEY absorption spectra of the a-CN_x films and HOPG as a reference obtained using NEXAFS. The NEXAFS spectra of the a-CN_x film was without dependence on the incident angle of X-ray to the film surface. HOPG showed two strong peaks at approximately 285.5 eV (known as the π* peak), and 292 eV corresponding to various σ* transitions.

Conversely, a fine structure comprising of at least six peaks, centered at 284.5 eV (C1), 285.8 eV (C2), 286.6 eV (C3), 288.2 eV (C4), 288.9 eV (C5), and 289.5 eV (C6), could clearly be seen in the spectra of the a-CN$_x$ films. These spectral features are recognized in the C K-edge spectra of carbon-related materials and amorphous carbon films containing nitrogen.

A comparing GP85 and CS85 shows, the presence of two remarkable points in the NEXAFS spectra, as shown in Fig. 2a: 1) several peaks appeared in a region of 284–285 eV in CS85 and 2) the C3 peak of CS85 has an extremely high intensity. The peaks in 284–285 eV can be assigned π* transition. The spectral feature, characteristic of the several peaks appearing in the region of 284−285 eV, is similar to the electron-energy-loss spectra (EELS) of fullerenes in the energy region of the carbon *K*-absorption edge.[16] The first large peak of C60 and C70 appears to be of lower energy than graphite, while several small peaks appear to be of lower energy than the first large peak. These small peaks become one broad peak and a shoulder as the number of carbon atoms increases from C60 to C84. In addition, pure carbon materials exhibit C1 and C5 peaks, such as fullerene and amorphous carbon, and these can be assigned to 1s→π* transition and 1s→σ* transition of the C=C bond, respectively.[17, 18] From these reports, the small peaks around the C1 peak of CS85 are due to existence from bending graphene sheet-like imperfect fullerenes. The C2 peak is from the π* states of the C–N single bond.[19]

The identification of the C3 peak is not in agreement with previous results. McCann *et al*. concluded that the peak at approximately 286.6 eV corresponding to C3 in Fig. 8 is mainly due to C=N bonds in tetrahedral amorphous carbon films with increasing nitrogen concentration ($0 < x < 10.3$ at.%).[16] Point *et al*. concluded that the C3 peak can be attributed to the sp^2 carbon bonded to nitrogen atoms, which are generally isolated nitrogen atoms involved in C=N and C≡N bonds.[20] Lutham *et al*. suggested that C3 is 1s→π* transition of C=C–NH.[21] The sharp peak at 289.3 eV in CS85 is an unknown peak, although this position is closer to 289.6 eV, which is assigned to the σ* excitation in diamond.[18] The C4 peak is attributed to the sp^2 carbon bonded to the nitrogen atoms corresponding to the conjugated nitrogen involved in single bonds, *i.e.* N–C–N or N≡C–N.[22]

With increasing RF power, several small peaks appeared around the C1 peak similar to those in the NEXAFS spectrum of CS85 as shown in Fig. 1b. At the edge of the spectra, GP85 had a relatively long tail starting from 283.0 eV and then gradually shortened up to 283.3 eV with increasing RF power. This is probably due to an asymmetrically shaped fullerene-like structure, as mentioned above.

The C3 peak was noticeable and shifted toward the lower energy with increasing RF power. This is due to decreased intensities of the C2 and C4 peaks. Both peaks are attributed to bonding with nitrogen, and thus, the C3 peak is assigned as the C=C bond. With decreasing N/C, the carbon-to-carbon antibonding state becomes dominant in the conduction band; thus, the antibonding state of C=C shifts toward lower energy.

Lutham *et al*. suggested that the peak position of C6 is the 1s→σ* transition of the N–C bond.[21] In contrast, MaCann *et al*. explained that C6 corresponds to a σ* transition of the C–H bonds.[16] For the C6 peak, hydrogen is not used in the deposition environment of GP samples, therefore this peak is attributed to the transition of 1s→ σ* as in the case of diamond.[18] The intensity of C6 peak increased with increasing RF power in GP samples as shown in Fig. 2b. Thus, the advantage of high RF power with GP mode was achieved to increase sp^3C– N bond.

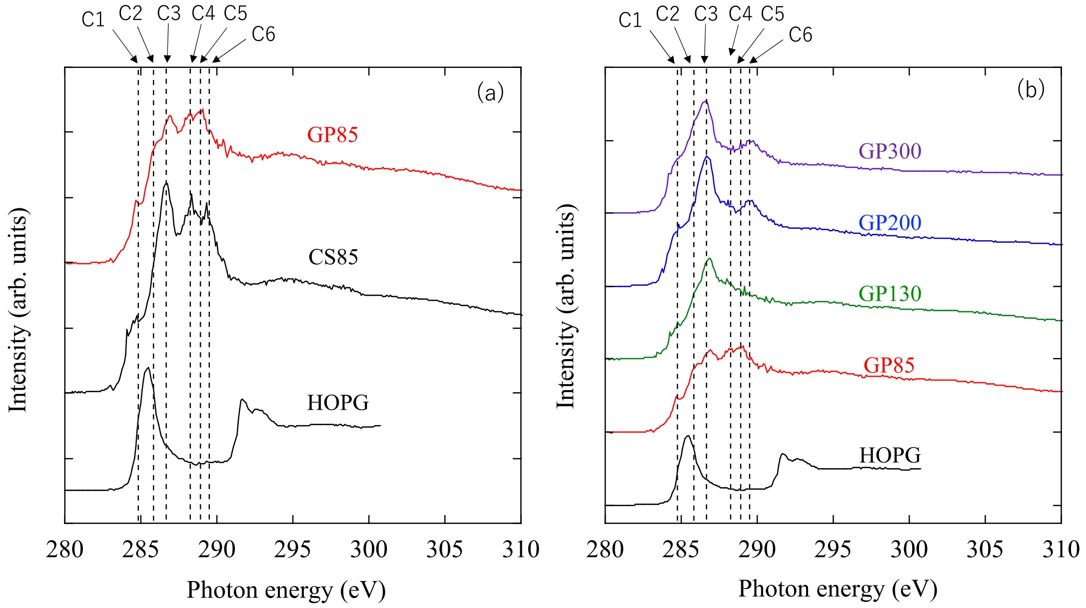

Figure 2. TEY X-ray absorption spectra in the C K-edge of a-CN$_x$ films and HOPG as a reference obtained using NEXAFS: (a) GP85 and CS85 and (b) GP samples prepared with different RF

4. Conclusion

Amorphous carbon nitride (a-CN_x) thin films were deposited using the gradient gas pressure sputtering method. The films were also deposited through the common sputtering mode, that is, at a uniform gas pressure in the chamber. The effect of the gradient gas pressure on the nitrogen content (N/C) was minimal, as obtained from XPS analysis results. The N/C ratios of the GP and CS samples were mostly the same at approximately 0.65 when the RF power was 85 W but decreased to 0.57 and 0.55, respectively, with increasing RF power up to 300 W. The chemical bonding structure of the films was investigated using NEXAFS measurements at NewSUBARU BL09A. When comparing GP and CS samples deposited at 85 W, a reduction of the peak intensity corresponding to the π^* transition was observed in the NEXAFS spectrum of GP samples. The intensity of the peak, which is assigned to the $1s\rightarrow\sigma^*$ transition of the N–C bond, increased with increasing RF power of GP mode. At the edge of NEXAFS spectra, the tail gradually decreased with increasing RF power.

Acknowledgement

A part of this work was supported from Hyogo COE Research Program and JSPS KAKENHI (22H00267).

References

[1] A. Y. Liu, M. L. Cohen: *Science*, **245**, 841 (1989).
[2] A. Y. Liu, M. L. Cohen: *Phys. Rev. B*, **41**, 10727 (1989).
[3] S. Matsumoto, E.-Q. Xie, F. Izumi: *Diam. Relat. Mater.*, **8**, 1175 (1999).
[4] E. F. Motta, I. Pereyra: *J. Non-Cryst. Solids*, **338-340**, 525 (2004).
[5] P. Wang, T. Takeno, K. Adachi, H. Miki, T. Takaghi: *Appl. Surf. Sci.,* **258**, 6576 (2012).
[6] Y. Iwano, T. Kittaka, H. Tacushi, M. Soukawa, S. Kunitsugu, K. Takarabe, K. Itoh: *Jpn. J. Appl. Phys*., **47**, 7842 (2008).
[7] H. Kinoshita, M. Kubota: *Thin Solid Films*, **518**, 3502 (2010).
[8] M. Aono, T. Takeno, T. Takagi: *Diam. Relat. Mater.,* **63**, 120 (2016).
[9] S. Nitta, in: S.R.P. Silva (Ed.), Amorphous Carbon, INSPEC, UK, 2002, p. 62–63.
[10] S. Nitta, M. Aono, T. Katsuno, Y. Naruse: *Diam. Relat. Mater.*, **12**, 219 (2003).
[11] N. Takada, K. Arai, S. Nitta, S. Nonomura: *Appl. Surf. Sci*., **113/114**, 274 (1997).
[12] Y. Terai, K. Haraguchi, R. Ichinose, H. Oota, K. Yonezawa: *Jpn. J. Appl. Phys.*, **62**, SA1003 (2023).
[13] N. Hellgren, R. T. Haasch, S. Schmidt, L. Hultman, I. Petrov, *Carbon*, **108**, 242 (2016).
[14] M. Niibe, M. Mukai, H. Kimura, Y. Shoji: *Fourth Huntsville gamma-ray burst symposium*, **705**, 243 (2004).
[15] M. Niibe, M. Mukai, S. Miyamoto, Y. Shoji, S. Hashimoto, A. Ando, T. Tanaka, M. Miyai, H. Kitamura: *Fourth Huntsville gamma-ray burst symposium*, **705**, 576 (2004).
[16] R. McCann, S.S. Roy, T, P. Papakonstantinou, I. Ahmad, P. Maguire, J.A. McLaughlin, L. Petaccia, S. Lizzit, A. Goldoni: *Diam. Relat. Mater.*, **14**, 1057 (2005).
[17] Y. Zhou, J. Lin, Xue-Ying Nie, Xiu-Neng Song, Yong Ma, Chuan-Kui Wang: *Spectrochim. Acta A*, **229**, 117904 (2020).
[18] J. Diaz, S. Anders, X. Zhou, E. J. Moler, S. A. Kellar, Z. Hussai: *Phys. Rev. B*, **64**, 125204 (2001).
[19] B. Bouchet-Fabre, K. Zellama, C. Godet, D. Ballutaud, T. Mine'a: *Thin Solid Films*, **482**, 156 (2005).
[20] S. Hosokawa, H. Sato, Y. Wang, E. Ohata, A. Fukushima: *J. Electron Spectrosc.*, **137-140**, 2357 (2004).
[21] K. G. Latham, M. I. Simone, W. M. Dose, J. A. Allen, S. W. Donne: *Carbon*, **114**, 566 (2017).
[22] S. Point, T. Minea, B. Bouchet-Fabre, A. Granier, G. Turban: *Diam. Relat. Mater.* **14**, 891 (2005).
[23] M. Aono, M. Terauchi, Y. K. Sato, K. Morita, T. Inoue, K. Kanda, K. Yonezawa: *Appl. Surf. Sci.*, **635**, 157677 (2023).

Laser irradiation effect on oriented *sp*^{2} bonded carbon structure in hydrogenated amorphous carbon films

Dai Harada[1], Naoki Umada[1], Yuko Aono[1], Kazuhiro Kanda[2], Masahito Niibe[2,3], Yuki Hirata[4], Naoto Ohtake[4], and Hiroki Akasaka[1*]

[1]*Dept. of Mechanical Eng., Tokyo Institute of Technology*
[2]*Laboratory of Advanced Science and Technology for Industry (LASTI), University of Hyogo*
[3]*Institute of Solid State Physics (ISSP), The University of Tokyo*
[4]*Institute of Innovative Research, Tokyo Institute of Technology*

Abstract

The effect of laser irradiation on the *sp*^{2} orientation of a hydrogenated amorphous carbon film with an oriented *sp*^{2} carbon bonding structure was evaluated by X-ray absorption spectroscopy using synchrotron radiation. XAS measurements while changing the incident angle of X-rays, and evaluated the change in the orientation of *sp*^{2} carbon from the angle dependence of π* peak at XAS spectra. A hydrogenated amorphous carbon film was deposited from C_2H_2 by the pulsed plasma CVD method and a ytterbium-doped fiber pulsed laser with 1064 nm was irradiated at defocus condition. The XAS spectra of the hydrogenated amorphous carbon films before and after laser irradiations measured at an X-ray incident angle of 0-75°. From angle dependence of the intensity of π* peak in hydrogenated amorphous carbon films, the *sp*^{2} orientation in the film became stronger by laser irradiation. From the molecular structure and the angle dependence at HOPG as standard sample, this indicates that the *sp*^{2} bonded carbons at the surface of these hydrogenated amorphous carbon films were oriented perpendicular to the substrate, this perpendicular orientation was increased by laser irradiation.

1. Introduction

Hydrogenated amorphous carbon film consists of *sp*^{2} or *sp*^{3} hybridized bonding carbon and hydrogen. The structure in hydrogenated amorphous carbon films is that these carbon bonding networks are terminated with hydrogen, and is often discussed in the ternary diagram in terms of *sp*^{2} or *sp*^{3} ratio and the amount of hydrogen[1, 2]. ISO 20523:2017 has also been established by International Organization for Standardization (ISO) based on the consideration including of ternary diagram[3]. Recently, extremely small the oriented *sp*^{2} bonded carbon network structure in hydrogenated amorphous carbon film was detected by the X-ray incident angle dependence of X-ray absorption spectroscopy (XAS) and X-ray emission spectroscopy (XES) measurements using synchrotron radiation X-rays[4]. Although this oriented *sp*^{2} structure is too small to be detected by X-ray diffraction, it was indicated there is an extremely small graphene sheet-like structure from results both the angle dependence of XAS measurement and the results of Raman spectroscopy. And the orientation distribution and direction of the *sp*^{2} carbon structure depended on the source material.

Although hydrogenated amorphous carbon films are usually weak against heating and change the structure[5,6], the partial heating using laser irradiation improve the tribological properties. It was reported that one of the structural changes was by *sp*^{2} increasing by laser irradiation[7]. It is possible that the orientation of *sp*^{2} is also changed due to the structural change of *sp*^{2} carbon due to this local heating. In this study, XAS measurements using synchrotron radiation X-rays with different incident angles were performed to detect the orientation of extremely small the *sp*^{2} bonded carbon network structure in hydrogenated amorphous carbon film. Based on previous study, an oriented *sp*^{2} structure containing hydrogenated amorphous carbon films were prepared and heated partially by laser irradiation, and we investigated how the orientation in the hydrogenated amorphous carbon film was changed.

2. Experimental

The hydrogenated amorphous carbon films were deposited by pulsed plasma chemical vapor deposition (CVD) method from acetylene (C_2H_2, 98 %)[8]. A pulsed power supply (TE-HV1000-TK: Tamaoki Electronics) was used as a power source to generate plasma. The Silicon (100) substrate was placed on the electrode in the vacuum chamber, which was evacuated to 5×10^{-3} Pa. Subsequently, argon (Ar, 99.995 %)

were introduced into the chamber while controlling the flow rates using a mass flow controller. The natural oxidation layer at the substrate surface was removed by Ar ion irradiation for 30 min before the deposition of the film. The flow rate of Ar and pressure of the reaction chamber were 20 cm^3/min and 2 Pa, respectively. The pulsed bias voltage of -3.5 kV, with a frequency of 14.4 kHz, was applied to generate Ar plasma. After the cleaning, C_2H_2 was introduced into the vacuum chamber with a flow rate of 20 cm^3/min. The pressure was adjusted to 3 Pa. A pulsed negative bias voltage of -4.5 kV with a frequency of 14.4 kHz was applied to the substrate. The thickness of the film deposited was adjusted by the controlling the deposition duration at approximately 500 nm.

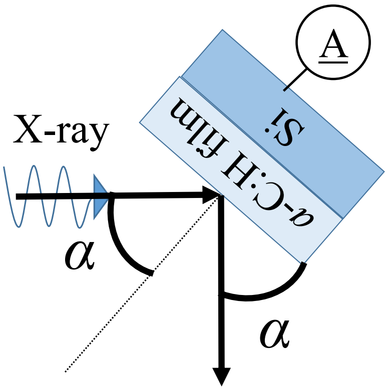

Figure 1. The X-ray incident angle, α at measurement.

Laser irradiation was conducted to these deposited hydrogenated amorphous carbon surface using laser marking apparatus with an ytterbium-doped fiber pulsed laser (LP-S; Panasonic). Its wavelength is 1064 nm. The energy density and irradiation time for one shot were 0.1 J/cm^2 and 20 μs, respectively. The laser irradiation area of the hydrogenated amorphous carbon film was controlled by dis tance between laser irradiation spots to 100 μm intervals using a galvanometer mirror scanner. The sample was placed at a depth of 5 mm from the focal point under laser irradiation. A laser microscope (OLS4100; Olympus Co.) and an optical microscope (BX53; Olympus Co.) were used to observe the surface shapes of laser-irradiated hydrogenated amorphous carbon films.

The XAS measurements for the hydrogenated amorphous carbon films using soft X-rays were carried out at the beamline BL-09A of the NewSUBARU synchrotron radiation facility at the University of Hyogo[9-12]. The samples were fixed to a copper plate holder, and was introduced into the vacuum chamber while maintaining pressure of the order of 10^{-5} Pa. The synchrotron radiation extracted from an undulator, which is the light source of BL-09A, was mo nochromated and introduced at the irradiation point of the sample. X-ray absorption spectra was measured using a total electron yield (TEY) method by sample current measurement[13]. The X-ray incident angle, α, for XAS measurement is defined as the angle measured from the film surface normal of the sample, as shown in Fig. 1. X-ray incident angle, α, was varied from 0 to 75°.

3. Results and Discussion

Figure 2 shows the photomicrographs before and after laser irradiation of the hydrogenated amorphous carbon film surface. Before laser irradiation, the hydrogenated amorphous carbon film deposited onto the Si substrate appeared completely smooth, observed under an optical microscope. The surface shape changed after an area of the films were subjected to laser irradiation at an interval of 100 μm using a galvanometer mirror scanner. From the photomicrographs after irradiation, circular shapes centered on the center point of the laser irradiation were observed on the surface. Continuous circles were observed at irradiation intervals of 100 μm. The center points of the circular irradiation areas matched the laser irradiation interval. The surface topographies of the irradiated samples were obtained and characterized using a laser microscope. The

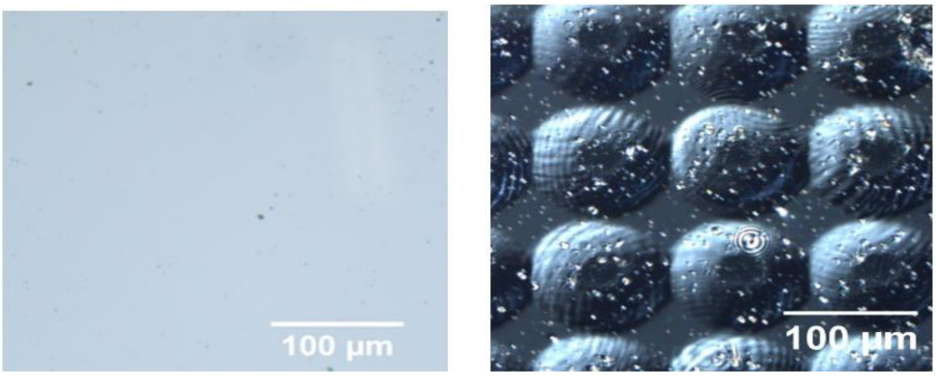

Figure 2. Photomicrographs; before (Left) and after (Right) laser irradiation.

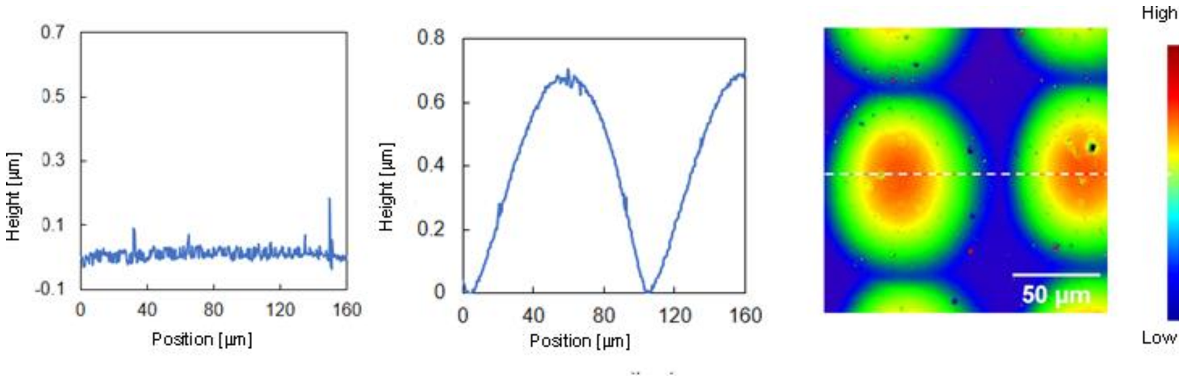

Figure 3. Cross sectional profiles before (Left) and after (center) the laser irradiation area, and laser microscopic images (Right) after irradiation.

images and the profiles at the center of the circular irradiation area are shown in Fig. 3. The films were changed to hemispherical shape from flat by the laser irradiation.

First, an evaluation using XAS was performed to detect the orientation of these sp^2 carbon network structures.

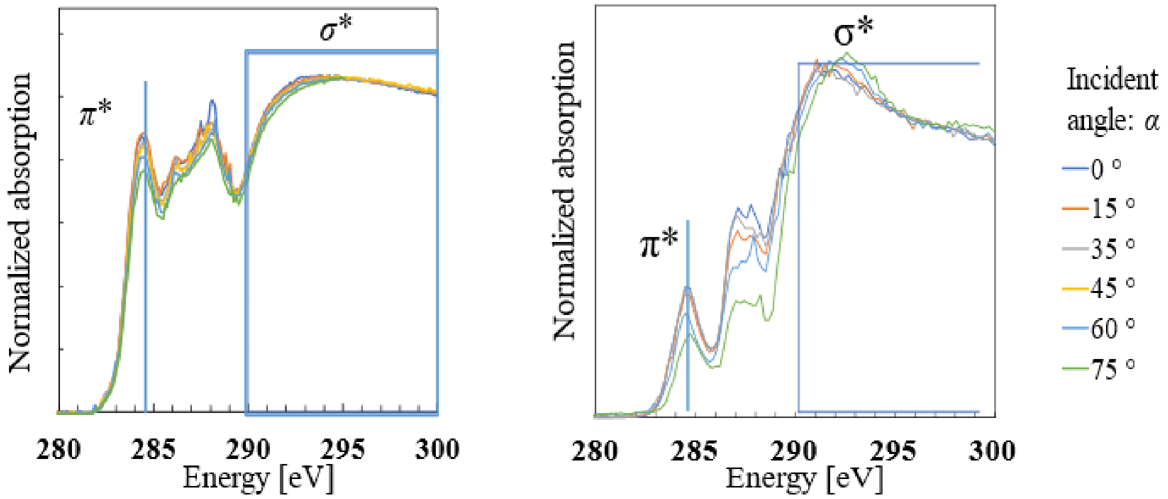

Figure 4. XAS spectra of hydrogenated amorphous carbon film before (Left) and after (Right) irradiation.

Figure 4 (Left) shows the XAS spectra of the hydrogenated amorphous carbon films before irradiation measured at an X-ray incident angle of 0-75° and normalized at 295 eV. Absorption of C=C π* in the sp^2 bonded carbon atoms was observed near the photon energy of 285 eV[14,15]. The broad peaks near 292-295 eV corresponds to the C-C σ* in sp^2 and sp^3-bonded carbon atoms was also observed[14, 16, 17]. The XAS spectra for the hydrogenated amorphous carbon films shows that the absorption intensity of π* band at 285 eV depend on the incident angle. Before laser irradiation, the intensity of π band depended on the X-ray incident angle. The results indicate that the peak intensity corresponding to the π* band in XAS spectra was dependent on X-ray incidence angle in the deposited hydrogenated amorphous carbon films, further indicating that oriented sp^2-bonded carbon networks were present in their film structures. Figure 4 (Right) shows the XAS spectra of the laser-irradiated hydrogenated amorphous carbon films measured at an X-ray incident angle of 0-75° and normalized at 295 eV. The XAS spectra for the laser-irradiated hydrogenated amorphous carbon film presented the dependence of the absorption intensity of π* band at 285 eV on the incident angle. The oriented sp^2 -bonded carbon networks were present in the laser-irradiated hydrogenated amorphous carbon film structures. These XAS measurements indicate that there are oriented graphene-like structures composed of very small sp^2-bonded carbons in the hydrogenated amorphous carbon films, and these orientations maintain in the films after laser irradiation.

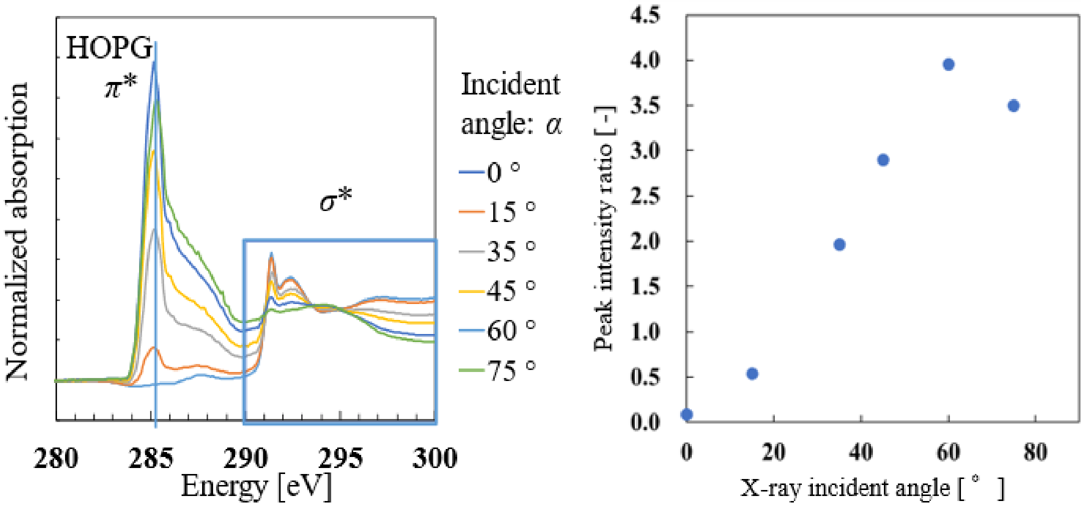

Figure 5. XAS spectra (Left) and X-ray incident angle dependence on peak intensity ratio of π^*/σ^* (Right) for HOPG.

Next, the orientation angle of the sp^2 carbons in hydrogenated amorphous carbon film was estimated from comparison of XAS spectra with HOPG as standard. The structure in HOPG is that sp^2 bonded-graphene sheets are stacked completely parallel to the material surface. Thus, at the X-ray incidence angle α=0°, the X-ray is incident perpendicular to the π electron cloud of the sp^2 bonded carbon networks. And this angle has the smallest absorption at π peak in XAS for HOPG. Figure 5 (Left) shows the XAS spectra of HOPG. The absorption intensity increases rapidly as α increases owing to the π* peak. The sp^2 orientation direction in the hydrogenated amorphous carbon films was estimated in HOPG based on this tendency. The angle dependence of the amount of X-ray absorbed was extremely small because the uniform electron distribution of sp^3 bonded carbon compared to that of the sp^2 bonded carbons. Hence, the change in intensity ratio of the peak of π*/σ* against the X-ray incident angle was determined. From spectra shown in Fig. 4, the X-ray incident angle dependence of the absorption intensity ratio of the peak at 284.5 eV was determined owing to the absorption of sp^2 bonded carbon. When the ratio against absorption ratio of 284.5 eV at X-ray incident angle α=0°, the absorption ratios were appeared the X-ray incident angle dependence as shown in Fig. 6. Angle dependence of the intensity ratio in hydrogenated amorphous carbon was opposite trend as that of HOPG, and the tendency became stronger by laser irradiation. From the molecular structure and the angle

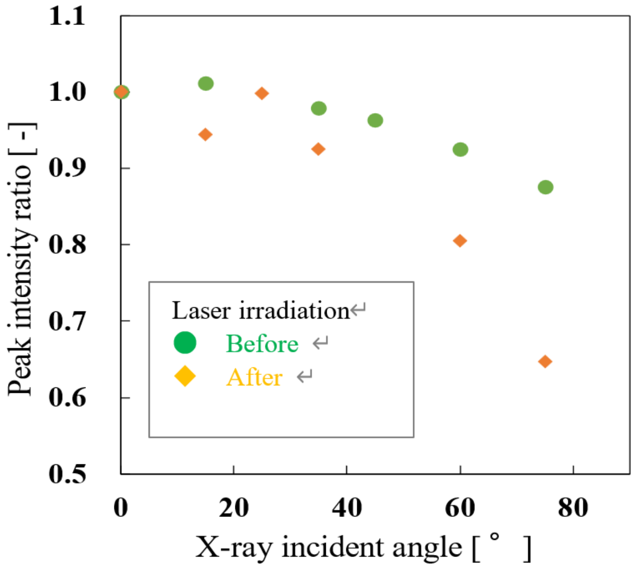

Figure 6. X-ray incident angle dependence on π^*/σ^* for the films.

dependence at HOPG, this indicates that the *sp*^{2} bonded carbons at the surface of these hydrogenated amorphous carbon films were oriented perpendicular to the substrate, this perpendicular orientation was increased by laser irradiation.

4. Conclusion

Using XAS with synchrotron radiation, a very small *sp*^{2} orientation in the hydrogenated amorphous carbon films was detected and laser irradiation to hydrogenated amorphous carbon films effect to the orientation was investigated. A hydrogenated amorphous carbon film was deposited from C_2H_2 by the pulsed plasma CVD method and the pulsed laser with 1064 nm was irradiated at defocus condition. The XAS spectra of the hydrogenated amorphous carbon films before and after laser irradiation measured at varying X-ray incident angle. From angle dependence of the intensity of π^* peak in hydrogenated amorphous carbon films, the *sp*^{2} orientation in the film became stronger by laser irradiation. By the comparison of the molecular structure and the angle dependence at HOPG, the *sp*^{2} bonded carbons with perpendicular orientation was increased by laser irradiation.

Acknowledgement

Funding: The part of this research was funded by the JSPS KAKENHI Grant-in-Aid for Scientific Research (B) Grant No. 22H01355, and ENEOS TONENGENERAL Research/Development Encouragement & Scholarship Foundation. The XRD and Raman spectroscopy analysis was performed at the Materials Analysis Division, Open Facility Center in Tokyo Institute of Technology.

References

[1] N. Ohtake, M. Hiratsuka, K. Kanda, H. Akasaka, M. Tsujioka, K. Hirakuri, A. Hirata, T. Ohana, H. Inaba, M. Kano, and H. Saitoh: *Materials* **14** 315 (2021).

[2] J. Robertson, Diamond-like amorphous carbon. *Mater. Sci. Eng.,* **R37** 129 (2002).

[3] *Carbon Based Films*—Classification and Designations ISO 20523:2017; The International Organization for Standardization; Vernier: Geneva, Switzerland, 2017.

[4] N. Umada, K. Kanda, M. Niibe, Y. Hirata, N. Ohtake, and H. Akasaka: *Diam. Relat. Mater.*, **131** 109533(2023).

[5] H. Akasaka, S. Tunmee, U. Rittihong, M. Tomidokoro, C. Euaruksakul, S. Norizuki, R. Supruangnet, H. Nakajima, Y. Hirata, and N. Ohtake: *Diam. Relat. Mater.*, **101** 107609 (2020).

[6] H. Akasaka, S. Kawaguchi, S. Ohshio, and H. Saitoh: *Trans. Mater. Res. Soc. Japan,* **36** 505 (2011).

[7] D. Harada, S. Tunmee, C. Euaruksakul, U. Rittihong, H. Nakajima, Y. Aono, Y. Hirata, N. Ohtake, and H. Akasaka: *Diam. Relat. Mater.*, **131** 109573 (2023).

[8] M. Tomidokoro, S. Tunmee, U. Rittihong, C. Euaruksakul, R. Supruangnet, H. Nakajima, Y. Hirata, N. Ohtake, and H. Akasaka: *Materials* **14** 2355 (2021).

[9] A. Ando, S. Amano, S. Hashimoto, H. Kinosita, S. Miyamoto, T. Mochizuki, M. Niibe, Y. Shoji, M. Terasawa, and T. Wantanebe: *Proc. the IEEE Particle Accelerator Conference*, **12–16** 757 (1997).

[10] S. Hashimoto, A. Ando, S. Amano, Y. Haruyama, T. Hattori, K. Kanda, H. Kinoshita, S. Matsui, H. Mekaru, S. Miyamoto, T. Mochizuki, M. Niibe, Y. Shoji, Y. Utsumi, T. Watanabe, and H. Tsubakino: *Trans. Mat. Res. Soc. Japan* **26** 783 (2001).

[11] K. Kanda, T. Ideta, Y. Haruyama, H. Ishigaki, and S. Matsui: *Jpn. J. Appl. Phys.* **42** 3983 (2003).

[12] Y. Kato, K. Kanda, Y. Haruyama, and S. Matsui: *Jpn. J. Appl. Phys.* **43** 3938 (2004).

[13] M. Niibe, T. Kotaka, and T. Mitamura: *J. Phys.: Conference Series* **425** 132008 (2013).

[14] P. E. Batson: *Phys. Rev. B* **48** 2608 (1993).

[15] M. Niibe, T. Tokushima, N. Takehira, and Y. Arakia: *J. Electron Spectroscopy Related Phenomena,* **220** 118 (2017).

[15] J. Stöhr: *NEXAFS spectroscopy,* Springer series in surface sciences.

[16] S. Ohmagari, T. Yoshitake, A. Nagano, S. AL-Riyami, R. Ohtami, H. Setoyama, E. Kobayashi, and K. Nagayama: *J. Nanomater.* 876561 (2009).

NEXAFS Studies of Amorphous Carbon Nitride Thin Films Deposited by Pressure-gradient RF Magnetron Sputtering

Masami Aono[1], Kyoji Morita[2], Tasuku Inoue[2], and Kazuhiro Kanda[3]
[1] *Department of Electrical and Electronics Engineering, Graduate School of Science and Engineering, Kagoshima University,*
[2]*Faculty of Engineering, University of Hyogo*
[3]*Laboratory of Advanced Science and Technology for Industry (LASTI), University of Hyogo*

Abstract

Amorphous carbon nitride (a-CN$_x$) thin films were deposited through radio frequency (RF) magnetron sputtering under increasing nitrogen gas pressure around a graphite target to provide nitrogen radicals at high concentrations. The C *K*-edge near-edge X-ray absorption fine structure (NEXAFS) measurements were performed at NewSUBARU BL09A. To increase the gas pressure around the graphite target, C *K*-edge NEXAFS spectra of the a-CN$_x$ films was changed. The nitrogen content in the a-CN$_x$ films obtained from XPS analysis did not increase when the nitrogen gas pressure around the graphite target was increased. The effect of nitrogen incorporation on the a-CN$_x$ films was comparatively more effective at higher RF powers.

1. Introduction

Liu and Cohen discovered a new super-hard material based on theoretical calculations, generating interest in carbon nitride compounds.[1] They predicted □-C_3N_4 based on □-Si_3N_4.[2] However, the growth of this hexagonal crystal structure has not been corroborated, even 30 years after its prediction. Following the prediction of □- C_3N_4, several crystalline structures based on *sp*^{3}C–N have been presented, such as □-C_3N_4 and cubic-C_3N_4.[3] Almost all the carbon nitrides prepared using thin film deposition techniques, such as chemical vapor deposition (CVD), sputtering, and laser ablation, have amorphous phases due to the low thermal stability of *sp*^{3}C–N bonds.

Thin films of amorphous carbon nitride (a-CN$_x$) comprise *sp*^{2}– and *sp*^{3}–hybridized carbon networks. a-CN$_x$ films can be deposited using two typical deposition methods: plasma-enhanced CVD using hydrocarbon gases and sputtering using graphite. NH_3 and N_2 are used as the nitrogen source. The range of nitrogen concentration (x) is wide, depending on the deposition method and condition; however, the maximum x value in most a-CN$_x$ films is approximately 0.5. Furthermore, a-CN$_x$ films deposited using the CVD method have a relatively lower nitrogen concentration and higher *sp*^{3}-C bonds because it contains hydrogen as source material.[4-6] In contrast, a-CN$_x$ films prepared from graphite and N_2 by physical vapor deposition have more *sp*^{2}-C bonds.[7, 8] The nitrogen concentration of the sputtering film depends on the sputtering gas ratio of Ar and N_2.

a-CN$_x$ films can be deposited with a high nitrogen concentration using the nitrogen-radical sputtering method proposed by Nitta *et al*.[9,10] In this method, nitrogen radicals in the glow discharge of nitrogen molecules react well with a carbon target at low energy.[11] This method can produce a higher nitrogen content than other techniques. The x value of a-CN$_x$ films deposited by nitrogen radical sputtering with hydrogen plasma etching is ~0.86.[10]

As essential technique to increase both the nitrogen content and *sp*^{3}C bond in a-CN$_x$ films is increasing the amount of high-energy nitrogen radical species. The mean free path of sputtered species on the growth surface is short under low-vacuum conditions. Therefore, sputtering under higher-vacuum conditions is desirable for the growth of high *sp*^{3}–hybridized carbon films. However, the number of nitrogen radical species is an important factor in increasing the nitrogen content. In the conventional sputtering method, the vacuum inside the growth chamber is uniform, and thus, generating excess nitrogen radicals is difficult. Recently, the pressure gradient sputtering source has been developed for sputtering at a high vacuum with low plasma damage.[12] In magnetron sputtering using a pressure gradient sputtering source, a gas is locally injected near the sputtering target through the pressure gradient sputtering source, and the main vacuum valve connected to the turbo-molecular pump is fully opened. This condition induces a pressure gradient with a high vacuum at the substrate position and a low vacuum around the target. Hence, the production of additional nitrogen radical species around the target can be expected using the pressure gradient sputtering source. In this study, a-CN$_x$ thin films were deposited using the pressure gradient and conventional sputtering modes with the same growth chamber, and the chemical bonding structure of the films was investigated to confirm the effect of nitrogen radicals.

2. Experimental

2.1. Sample Preparation

a-CN_x films were prepared from graphite with a purity of 99.95% and N_2 with a purity of 99.99995%. The substrates used were SiO_2 glass and Si(100), which were cleaned ultrasonically in acetone and ethanol for 15 min each, before loading into the vacuum chamber.

In the sputtering system, the gas inlet can be changed between two modes, the conventional sputtering and pressure gradient modes, by operating valves. In the gas pressure gradient mode (GP), the sputtering gas was injected near the target. Therefore, the gas pressure around the target was approximately one order of magnitude higher than that around the substrate holder. In comparison, the gas pressure in the chamber in the conventional sputtering mode (CS) was kept constant owing to the flow of N_2 gas through the middle of the target and substrate holder.

The base pressure was under 1×10^{-3} Pa. For the film deposition, the N_2 gas flow rate was 3 sccm, and the process pressure was maintained at 16 Pa (measured near the substrate holder). The samples obtained at RF powers of 85, 130, 200, and 300 W by the conventional sputtering mode were denoted by CS85, CS130, CS200 and CS300, respectively; the samples obtained using the gradient-pressure mode were denoted by GP85, GP130, GP200, and GP300, respectively.

2.2. Characterizations

The atomic concentrations of the samples were obtained from the C1s, N1s, O1s, and Si2p core-level peaks using X-ray photoelectron spectroscopy (XPS; Kratos Ultra 1, Shimadzu); Si was derived from the substrate. Monochromatic Al Kα radiation (1486.6 eV) was used as the X-ray source. The pass energy and step size were 40 and 0.05 eV, respectively. The analysis area was 300 μm × 700 μm. In this study, the Ar^+ bombardment etching process was skipped because it could possibly destroy the chemical bonding structure between carbon and nitrogen. The corresponding binding energies were calibrated with the C1s line at 284.5 eV for all cases, which could be assigned to *sp*^{2} graphite like carbon.[13]

Near-edge X-ray absorption fine structure (NEXAFS) spectroscopy is sensitive to the local coordination of the CN structure and a probe of the electronic structure of unoccupied orbitals of carbon. NEXAFS measurements were performed using the BL09A at the NewSUBARU synchrotron facility of the University of Hyogo[14, 15]; the instrument has an 11 m undulator as a light source and a grating monochromator. The electron energy of the storage ring during this study was 1.23 GeV. The samples deposited on a Si substrate were mounted on a copper plate using a carbon conductive tape. The electrons emitted from the sample were detected in the total electron yield (TEY) mode. The NEXAFS spectra of the C K-edge absorption were measured using a grating of 1200 grooves/mm in the range of 275–330 eV. The energy resolution was estimated to be less than 0.5 eV (full width at half maximum).

3. Results and Discussion

Figure 1 shows the nitrogen content (N/C) obtained from the C1s and N1s core level XPS spectra. The GP and CS samples showed a similar N/C tendency as a function of the RF power. An increase in the RF power decreased the nitrogen content of the films in both sputtering modes. GP85 and CS85 have almost the same N/C ratio of 0.66, showing no significant influence of gas pressure around the target. A comparing of GP300 and CS300 indicates that the N/C ratio of GP300 is slightly larger than that of CS300. The slopes of the regression line of the GP and CS samples were 0.4×10^{-3} and 0.5×10^{-3}, respectively. The oxygen content (O/C) of the samples were in the range of 0.09–0.14; the oxygen originates from the surface adsorption of O_2 and H_2O after the deposition.

Figures 2 shows the TEY absorption spectra of the a-CN_x films and HOPG as a reference obtained using NEXAFS. The NEXAFS spectra of the a-CN_x film was without dependence on the incident angle of X-ray to the film surface. HOPG showed two strong peaks at approximately 285.5 eV (known as the π^* peak), and 292 eV corresponding to various σ^* transitions. Conversely, a fine structure comprising of at least six peaks, centered at 284.5 eV (C1), 285.8 eV (C2), 286.6 eV (C3), 288.2 eV (C4), 288.9 eV (C5), and 289.5 eV (C6), could clearly be seen in the spectra of the a-CN_x films. These spectral features are recognized in the C K-edge spectra of carbon-related materials and amorphous carbon films containing nitrogen.

A comparing GP85 and CS85 shows, the presence of two remarkable points in the NEXAFS spectra, as shown in Fig. 2a: 1) several peaks appeared in a region of 284–285 eV in CS85 and 2) the C3 peak of CS85 has an extremely high intensity. The peaks in 284–285 eV can be assigned π^* transition. The spectral feature, characteristic of the several peaks appearing in the region of 284–285 eV, is similar to the electron-energy-

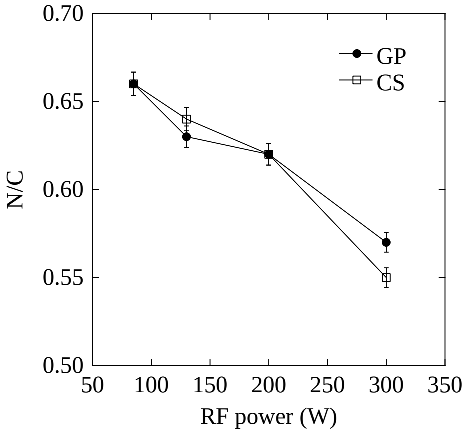

Figure 1. Nitrogen content (N/C) of a-CN_x films deposited using the gradient gas pressure (GP) and common sputtering (CS) modes.[23]

loss spectra (EELS) of fullerenes in the energy region of the carbon *K*-absorption edge.[16] The first large peak of C60 and C70 appears to be of lower energy than graphite, while several small peaks appear to be of lower energy than the first large peak. These small peaks become one broad peak and a shoulder as the number of carbon atoms increases from C60 to C84. In addition, pure carbon materials exhibit C1 and C5 peaks, such as fullerene and amorphous carbon, and these can be assigned to 1s→π* transition and 1s→σ* transition of the C=C bond, respectively.[17, 18] From these reports, the small peaks around the C1 peak of CS85 are due to existence from bending graphene sheet-like imperfect fullerenes. The C2 peak is from the π* states of the C–N single bond.[19]

The identification of the C3 peak is not in agreement with previous results. McCann *et al.* concluded that the peak at approximately 286.6 eV corresponding to C3 in Fig. 8 is mainly due to C=N bonds in tetrahedral amorphous carbon films with increasing nitrogen concentration ($0 < x < 10.3$ at.%).[16] Point *et al.* concluded that the C3 peak can be attributed to the sp^2 carbon bonded to nitrogen atoms, which are generally isolated nitrogen atoms involved in C=N and C≡N bonds.[20] Lutham *et al.* suggested that C3 is 1s→π* transition of C=C–NH.[21] The sharp peak at 289.3 eV in CS85 is an unknown peak, although this position is closer to 289.6 eV, which is assigned to the σ* excitation in diamond.[18] The C4 peak is attributed to the sp^2 carbon bonded to the nitrogen atoms corresponding to the conjugated nitrogen involved in single bonds, *i.e.* N–C–N or N≡C–N.[22]

With increasing RF power, several small peaks appeared around the C1 peak similar to those in the NEXAFS spectrum of CS85 as shown in Fig. 1b. At the edge of the spectra, GP85 had a relatively long tail starting from 283.0 eV and then gradually shortened up to 283.3 eV with increasing RF power. This is

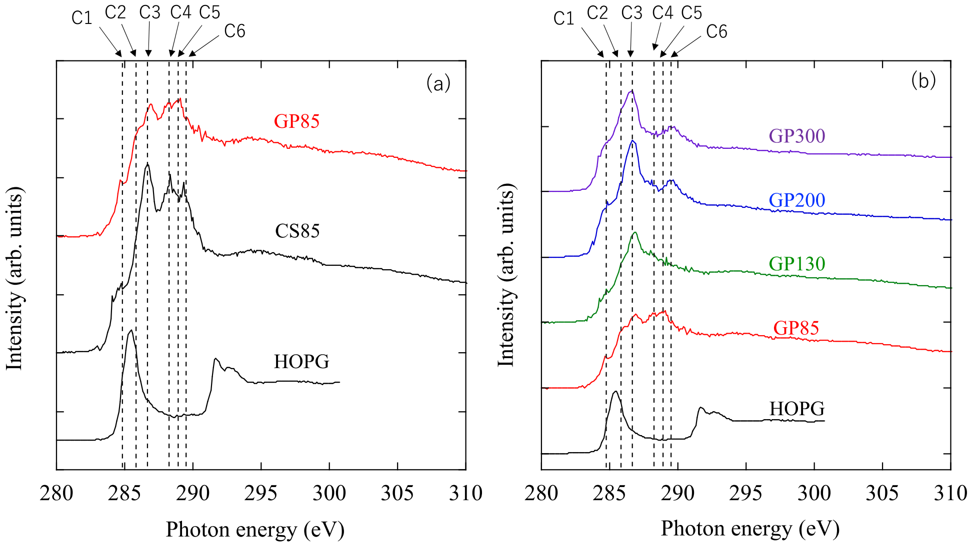

Figure 2. TEY X-ray absorption spectra in the C K-edge of a-CN_x films and HOPG as a reference obtained using NEXAFS: (a) GP85 and CS85 and (b) GP samples prepared with different RF power.[23]

probably due to an asymmetrically shaped fullerene-like structure, as mentioned above.

The C3 peak was noticeable and shifted toward the lower energy with increasing RF power. This is due to decreased intensities of the C2 and C4 peaks. Both peaks are attributed to bonding with nitrogen, and thus, the C3 peak is assigned as the C=C bond. With decreasing N/C, the carbon-to-carbon antibonding state becomes dominant in the conduction band; thus, the antibonding state of C=C shifts toward lower energy.

Lutham *et al*. suggested that the peak position of C6 is the 1s→σ* transition of the N–C bond.[21] In contrast, MaCann *et al*. explained that C6 corresponds to a σ* transition of the C–H bonds.[16] For the C6 peak, hydrogen is not used in the deposition environment of GP samples, therefore this peak is attributed to the transition of 1s→ σ* as in the case of diamond.[18] The intensity of C6 peak increased with increasing RF power in GP samples as shown in Fig. 2b. Thus, the advantage of high RF power with GP mode was achieved to increase sp^3C– N bond.

4. Conclusion

Amorphous carbon nitride (a-CN_x) thin films were deposited using the gradient gas pressure sputtering method. The films were also deposited through the common sputtering mode, that is, at a uniform gas pressure in the chamber. The effect of the gradient gas pressure on the nitrogen content (N/C) was minimal, as obtained from XPS analysis results. The N/C ratios of the GP and CS samples were mostly the same at approximately 0.65 when the RF power was 85 W but decreased to 0.57 and 0.55, respectively, with increasing RF power up to 300 W. The chemical bonding structure of the films was investigated using NEXAFS measurements at NewSUBARU BL09A. When comparing GP and CS samples deposited at 85 W, a reduction of the peak intensity corresponding to the π* transition was observed in the NEXAFS spectrum of GP samples. The intensity of the peak, which is assigned to the 1s→π* transition of the N–C bond, increased with increasing RF power of GP mode. At the edge of NEXAFS spectra, the tail gradually decreased with increasing RF power.

Acknowledgement

A part of this work was supported from Hyogo COE Research Program and JSPS KAKENHI (22H00267).

References

[1] A. Y. Liu, M. L. Cohen: *Science*, **245**, 841 (1989).
[2] A. Y. Liu, M. L. Cohen: *Phys. Rev. B*, **41**, 10727 (1989).
[3] S. Matsumoto, E.-Q. Xie, F. Izumi: *Diam. Relat. Mater.*, **8**, 1175 (1999).
[4] E. F. Motta, I. Pereyra: *J. Non-Cryst. Solids*, **338-340**, 525 (2004).
[5] P. Wang, T. Takeno, K. Adachi, H. Miki, T. Takaghi: *Appl. Surf. Sci.,* **258**, 6576 (2012).
[6] Y. Iwano, T. Kittaka, H. Tacushi, M. Soukawa, S. Kunitsugu, K. Takarabe, K. Itoh: *Jpn. J. Appl. Phys.*, **47**, 7842 (2008).
[7] H. Kinoshita, M. Kubota: *Thin Solid Films*, **518**, 3502 (2010).
[8] M. Aono, T. Takeno, T. Takagi: *Diam. Relat. Mater.,* **63**, 120 (2016).
[9] S. Nitta, in: S.R.P. Silva (Ed.), Amorphous Carbon, INSPEC, UK, 2002, p. 62–63.
[10] S. Nitta, M. Aono, T. Katsuno, Y. Naruse: *Diam. Relat. Mater.*, **12**, 219 (2003).
[11] N. Takada, K. Arai, S. Nitta, S. Nonomura: *Appl. Surf. Sci.*, **113/114**, 274 (1997).
[12] Y. Terai, K. Haraguchi, R. Ichinose, H. Oota, K. Yonezawa: *Jpn. J. Appl. Phys.*, **62**, SA1003 (2023).
[13] N. Hellgren, R. T. Haasch, S. Schmidt, L. Hultman, I. Petrov: *Carbon*, **108**, 242 (2016).
[14] M. Niibe, M. Mukai, H. Kimura, Y. Shoji: *Fourth Huntsville gamma-ray burst symposium*, **705**, 243 (2004).
[15] M. Niibe, M. Mukai, S. Miyamoto, Y. Shoji, S. Hashimoto, A. Ando, T. Tanaka, M. Miyai, H. Kitamura: *Fourth Huntsville gamma-ray burst symposium*, **705**, 576 (2004).
[16] R. McCann, S.S. Roy, T, P. Papakonstantinou, I. Ahmad, P. Maguire, J. A. McLaughlin, L. Petaccia, S. Lizzit, A. Goldoni: *Diam. Relat. Mater.*, **14**, 1057 (2005).
[17] Y. Zhou, J. Lin, Xue-Ying Nie, Xiu-Neng Song, Yong Ma, Chuan-Kui Wang: *Spectrochim. Acta A*, **229**, 117904 (2020).
[18] J. Diaz, S. Anders, X. Zhou, E. J. Moler, S. A. Kellar, Z. Hussai: *Phys. Rev. B*, **64**, 125204 (2001).
[19] B. Bouchet-Fabre, K. Zellama, C. Godet, D. Ballutaud, T. Mine'a: *Thin Solid Films*, **482**, 156 (2005).
[20] S. Hosokawa, H. Sato, Y. Wang, E. Ohata, A. Fukushima: *J. Electron Spectrosc.*, **137-140**, 2357 (2004).
[21] K. G. Latham, M. I. Simone, W. M. Dose, J. A. Allen, S. W. Donne: *Carbon*, **114**, 566 (2017).
[22] S. Point, T. Minea, B. Bouchet-Fabre, A. Granier, G. Turban: *Diam. Relat. Mater.* **14**, 891 (2005).
[23] M. Aono, M. Terauchi, Y. K. Sato, K. Morita, T. Inoue, K. Kanda, K. Yonezawa: *Appl. Surf. Sci.*, **635**, 157677 (2023).

Development of Reflection- and Projection-Type Soft-X-Ray Microscope (RPS-XRM) for Resist-Thin-Film Observation

Tetsuo Harada, Shuhei Iguchi, Shinji Yamakawa, and Takeo Watanabe

Laboratory of Advanced Science and Technology for Industry (LASTI), University of Hyogo

Abstract

A reflection- and projection-type soft-X-ray microscope (RPS-XRM) was developed at the NewSUBARU synchrotron light facility to observe the chemical state distribution of resist thin film on the Si wafers. A capillary mirror was used to focus the soft X-ray on the wafer at oblique incidence. Magnified projection image was observed on a CCD camera. The observation result of a chemically amplified resists revealed the presence of aggregation structures, which would cause defect in EUV lithography.

1. Introduction

In EUV lithography at a wavelength of 13.5 nm, the development of high-performance resists is very important. In addition to achieve high resolution and high sensitivity, resists with small line width variation and few defects simultaneously are required. Local aggregation of resist components is considered to be one of the causes of defect generation. Line width variations on the order of several micrometers scale have been reported as local critical dimension (CD) uniformity based on CD-SEM observations, and it is thought that resist aggregation occurs on the micrometer scale. Since the aggregation of resist components would be caused by the polarity of the functional groups and conventional microscopes cannot observe them at a few µm size, soft X-ray observation is suitable for this purpose. Scanning soft X-ray microscopy (STXM) is usually used for soft X-ray imaging. However, STXM cannot measure resist wafers coated in the actual process. Therefore, we developed a reflection-and projection-type soft-X-ray microscope (RPS-XRM)1) to observe the chemical state distribution of the resist on the wafer.

2. Experimental

A schematic view of RPS-XRM developed at the NewSUBARU synchrotron radiation facility beamline BL-10 is shown in Fig. 1. The monochromator of BL-10 provides soft X-ray of 50 – 1,000 eV region. In this study, we used around carbon K-edge region of 284 eV. A 100-µm-diameter pinhole is installed at the focusing point as a virtual source using. The pinhole image was focused by a capillary mirror optic (Sigray)2), which has an axially symmetric ellipsoidal shape. The focusing size evaluated by the knife-edge method was around 2 µm. In this microscope, the sample is placed horizontally on the optical axis and half of the light from the capillary mirror is focused near the sample surface. The soft X-rays reflected by the sample are

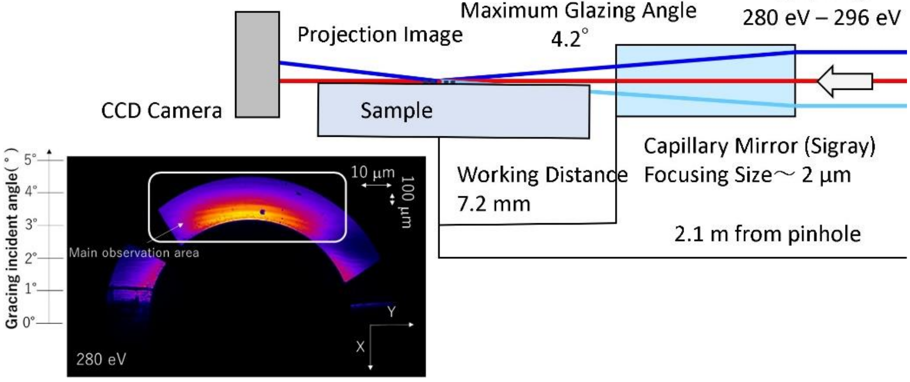

Figure 1. Schematic layout of the RPS-XRM, and observation result example.

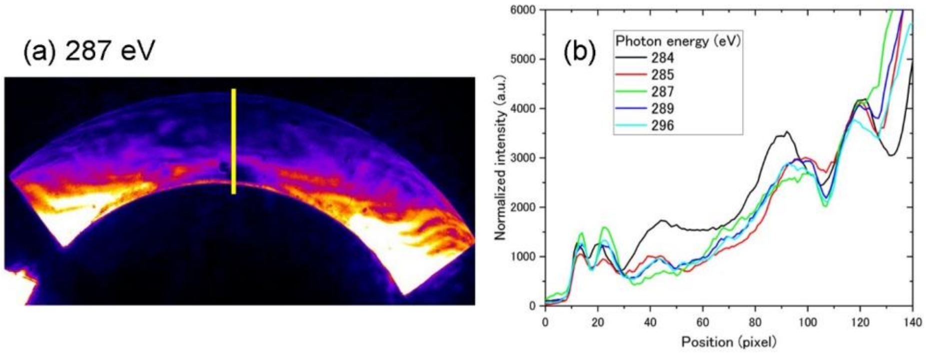

Figure 2. (a) Observation result image of CAR 50 nm thick resist at 287 eV. (b) Intensity profile at the indicated line position in (a).

magnified and projected onto a CCD camera. The angle of incidence is determined by the angle of incidence of the mirror, with a maximum angle of 4.2° and oblique incidence.

On the lower energy side of the carbon absorption edge, such as 280 eV, where the absorption of the resist is small, the surface reflection of the resist is weak and is mainly from the substrate silicon wafer. In this case, an absorption image of the resist can be observed. On the high energy side, the absorption of the resist becomes larger and all components reflected by the wafer are absorbed, resulting in the observation of the surface reflectance distribution. The observed image is a sample image projected on a half arc corresponding to the acquisition angle of the focusing element. The observation magnification varies with the distance between the focal point and the sample reflection point and is usually in the range of 60 – 1000x.

3. Results and Discussion

The sample is a 50 nm thick chemically amplified resist (CAR) on a silicon wafer. The observation image is shown in Fig. 2(a). The observed energy is 287 eV. The stripe pattern is mainly derived from speckles from the substrate of the Si wafer. In order to compare in the observation photon energy, measured intensity profiles on the yellow line in Fig. 2(a) are shown in 284 - 296 eV. The speckle shape is dominant in the profiles as well, but the shape differs with energy around 70 pixel position; no aggregation is observed at 284 eV, but a change in the intensity profile occurs, especially at 287 eV. The speckle distribution does not change significantly in this energy range. Therefore, the change is sample-induced and is an aggregation structure of the functional groups in the resist. The total length of the profile is 100 µm, so the aggregation structure is of the order of 10 µm. This aggregation would change the local pattern formation characteristics and cause the local CD changes, which would change the local defects formation characteristic.

4. Conclusion

The existence of large aggregation structures was revealed using RPS-XRM. This microscope can be used to observe the chemical state distribution of not only resist but also functional thin films such as carbon in a wide energy range of 50 eV-1,000 eV, and has a wide range of applications, including the ability to observe the chemical state distribution of films that were thought to be uniform.

References

[1] Shuhei Iguchi, Tetsuo Harada, Shinji Yamakawa, Takeo Watanabe, and Takeharu Motokawa: *J. Photopolym. Sci. Technol.* **36** (2023) 25.

[2] R. J. Koch, C. Jozwiak, A. Bostwick, B. Stripe, M. Cordier, Z. Hussain, W. Yun, and E. Rotenberg: *Synchrotron Rad. News*, **31** (2018) 50.

Analytical method to determine Fe^{3+}/Fe^{2+} ratio in pumice: Oxidation process pumice from 7.6 ka Mashu caldera-forming eruption

Kyohei Sano[1], Tetsuo Harada[2], and Shinji Yamakawa[2]

[1]*Graduate School of Regional Resource Management, University of Hyogo*
[2]*Laboratory of Advanced Science and Technology for Industry (LASTI), University of Hyogo*

Abstract

We conducted synchrotron analysis for pumices from Mashu caldera-forming activity and established the analytical method to determine the Fe^{3+}/Fe^{2+} ratio in volcanic products using soft X-ray synchrotron. To determine the Fe^{3+}/Fe^{2+} ratio, we collected absorption spectra between 650 eV and 750 eV with using the standard materials at room temperature using the BL-10 beamline at the NewSUBARU, Laboratory of Advanced Science and Technology for Industry, University of Hyogo, Japan. The soft X-rays were focused on 2.5 mm ×1.2 mm area. To construct the calibration curve for Fe^{3+}/Fe^{2+} ratio, standard materials are prepared by wet chemistry. Based on the calibration curve, we estimated the Fe^{3+}/Fe^{2+} ratio for Mashu caldera-forming eruption. In the Ma-i layer, Fe^{3+}/Fe^{2+} ratio changes from 11.5 to 16.6 from lower to the upper layer. On the other hand, Fe^{3+}/Fe^{2+} ratio in Ma-h layer changes from 9.2 to 13.1. These valuable Fe^{3+}/Fe^{2+} ratios are formed because of the change of temperature of eruption cloud and eruption rate during eruption.

1. Introduction

Caldera-forming eruption including pyroclastic flow has a huge influence on human society and it is important to reveal the sequence of magma ascent process during the eruption for the risk management of volcanic eruption. For the formation of pyroclastic flow, the stability of the eruption cloud is an essential factor[1]. The entrainment of air into the eruption cloud originates the buoyancy because of the heating and thermal expansion of air. Such entrainment also causes the oxidation of pyroclasts. Thus, by analyzing the degrees of oxidation based on the Fe^{3+}/Fe^{2+} ratio in volcanic products, we can reveal the temperature condition in volcanic clouds, and discuss the formation process of pyroclastic flow based on the temperature of volcanic clouds. In this study, we conducted the synchrotron analyses for pumices from Mashu caldera-forming activity and constructed the calibration curve to estimate the Fe^{3+}/Fe^{2}+ ratio.

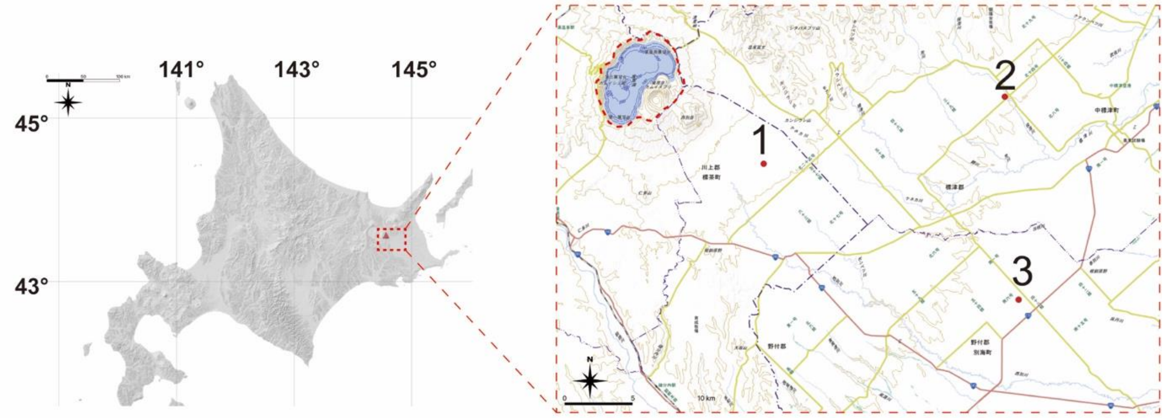

Figure 1. Location of Mashu volcano and sampling point.

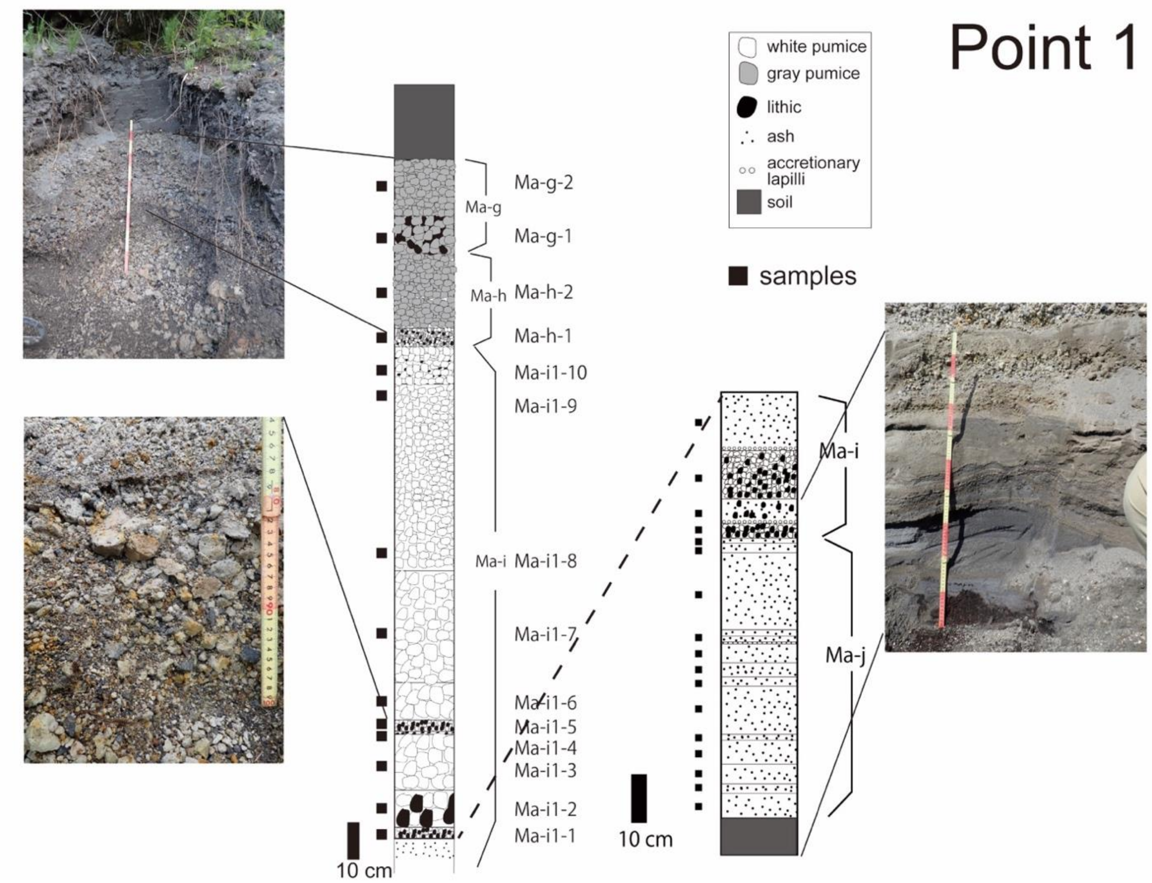

Figure 2. Columnar section and photographs pf Point 1 outcrop.

2. Experimental

2.1. Sample Preparation

Mashu Volcano is located in the east part of Hokkaido, Japan. Approximately 7.6 ka, the caldera-forming activity of Mashu Volcano started as phreatomagmatic eruption (Ma-j) and followed Plinian falls (Ma-i, -h, -g) and pyroclastic flow (Ma-f)[2] (Fig.2). In this study, we conducted the field survey and collected samples for synchrotron analysis. We sieved samples and picked up the pumices larger than 4 mm. Samples were washed by a sonic wave washer and dried at 110°C. For the synchrotron analysis, we used the powdered pumices.

2.2. Analytical method

To determine the Fe^{3+}/Fe^{2+} ratio of pumice samples, we collected the absorption spectra between 650 eV and 750 eV by using the standard materials at room temperature using the BL-10 beamline at the NewSUBARU, Laboratory of Advanced Science and Technology for Industry, University of Hyogo, Japan. The soft X-rays were focused on a 2.5 mm ×1.2 mm area. For the standard material, pumice from the 7.6 ka Mashu

Figure 3. Samples for synchrotron analysis.

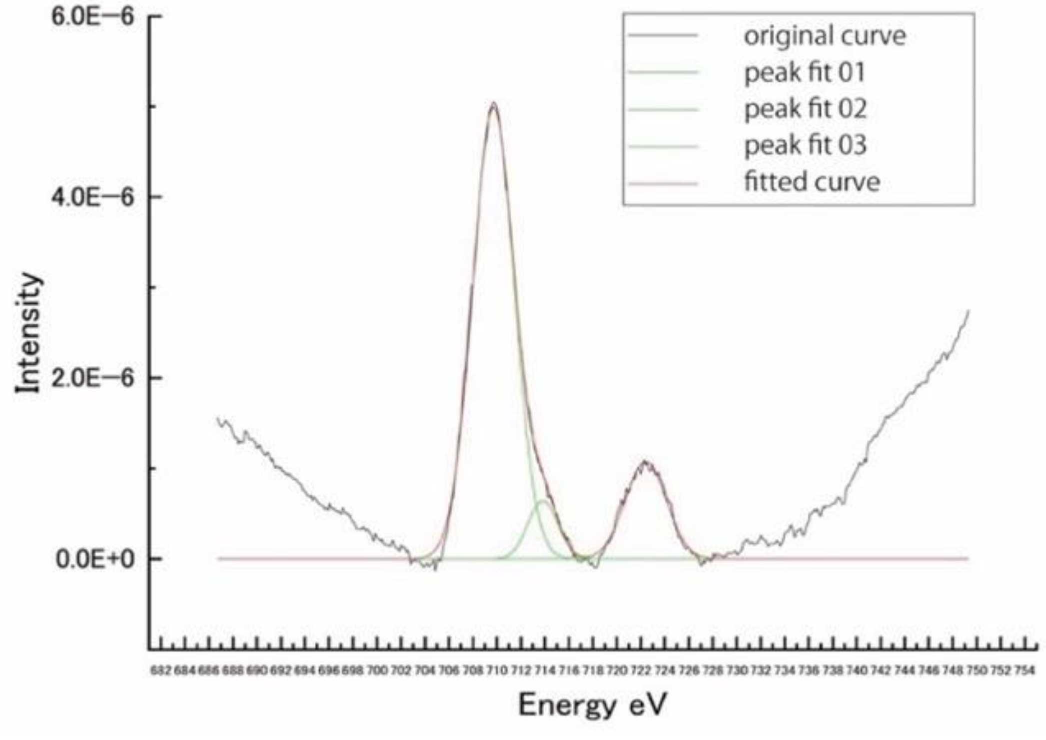

Figure 4. Representative spectra and separated Gaussian peak.

eruption and obsidian from Akaishiyama lava, Shirataki, Hokkaido, Japan[3] were analyzed by wet chemical analysis at JFE Tecno-Research Corporation. Samples were mounted on the analytical stage by carbon tape (Fig. 3).

3. Results

Figure 4 shows the representative analytical results. In the spectrum, peaks around 709 eV and 723 eV reflect the L_3 and L_2 of Fe, respectively[4] (Fig. 4). Furthermore, we identified the small peak around 713 eV, and we considered that this peak reflects the Fe^{3+} of L_3[4]. For the construction of the calibration curve, we extracted the three Gaussian peaks on 709, 713, 723 eV, and collected the peak intensity and area of each Gaussian peak. Using the intensity and area values, we calculate the peak character as follows;

$$\boldsymbol{Peak\ character} = (\boldsymbol{I_{709}} / \boldsymbol{I_{713}}) \times \boldsymbol{A_{722}} \times \boldsymbol{A_{713}}$$

where I is the intensity, and A is the area of each Gaussian peak. By compiling the peak character values and Fe^{3+}/Fe^{2+} ratio determined by wet chemical analysis, we construct the calibration curve for Fe^{3+}/Fe^{2+} ratio by using the absorption spectra (Fig.5). Constructed calibration curve shows that slope is 4.9×10^{10} and correlation factor (R^2) is 0.9, although some variation of peak character in same sample are observed.

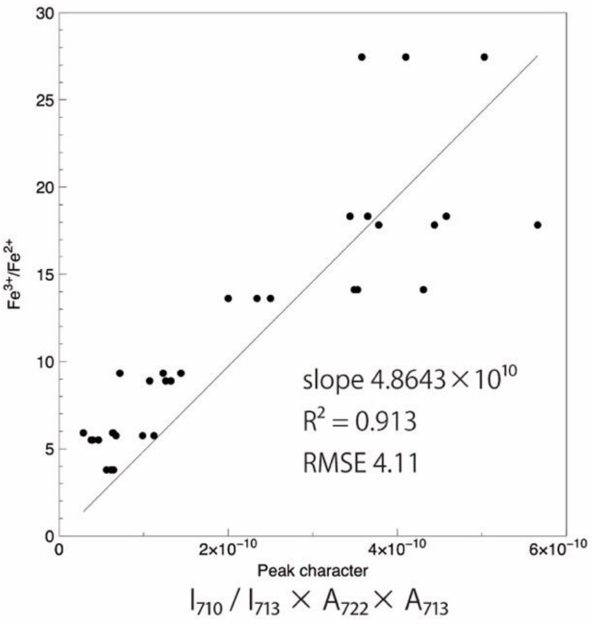

Figure 5. Constructed calibration curve for Fe^{3+}/Fe^{2+} ratio.

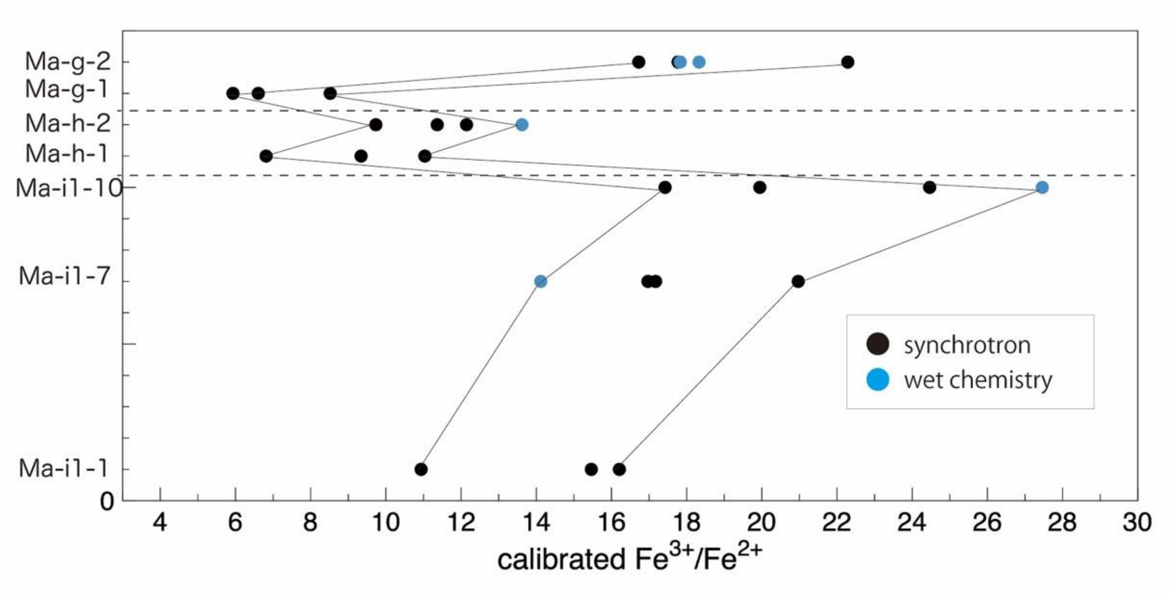

Figure 6. Fe^{3+}/Fe^{2+} ratio for 7.6ka Mashu pumices estimated by soft X-ray synchrotron analysis.

4. Discussion

Based on the calibration curve, we estimated the Fe^{3+}/Fe^{2+} ratio for Mashu caldera-forming eruption. Figure 6 shows the estimated Fe^{3+}/Fe^{2+} ratio for 7.6ka Mashu pumices. In the Ma-i layer, Fe^{3+}/Fe^{2+} ratio changes from 12 to 17 from lower to the upper layer. On the other hand, Fe^{3+}/Fe^{2+} ratio in Ma-h layer ranges from 7 to 12 (Fig. 6). In Ma-g layer, Fe^{3+}/Fe^{2+} ratio drastically increase from 6 to 22 (Fig.6). We considered that these variations in Fe^{3+}/Fe^{2+} ratio reflect the change of eruption rate and temperature of eruption cloud during eruption.

The variability of peak character could be caused by the sample preparation. Powdered pumice is not sieved and the amount of powder on the analytical stage is not constant. These preparations affect the electrical conductivity of samples. Furthermore, we analyzed three times for each sample and the increase of number of analyses enhances the accuracy.

5. Conclusion

In this study, we conducted the synchrotron analyses for pumices from Mashu caldera-forming activity and tried to establish the analytical method to determine the Fe^{3+}/Fe^{2+} ratio. Fe^{3+}/Fe^{2+} ratio for Mashu caldera-forming eruption shows variability and we considered that these Fe^{3+}/Fe^{2+} ratio reflect the change of eruption rate and temperature of eruption cloud during eruption.

Acknowledgement

This study was supported by ERI JURP 2021-KOBO21 in Earthquake Research Institute, the University of Tokyo. Dr. Keiji Wada supported field survey in Mashu volcano. Wet chemical analysis for standard materials were conducted by JFE Tecno-Research Corporation.

References

[1] A. W. Woods: *Bulletin of Volcanology.* **50**, 169-193 (1988).
[2] H. Kishimoto, T. Hasegawa, M. Nakagawa, K, Wada: *Bulletin of the Volcanological Society of Japan.* **54**, 15-36 (2009).
[3] K. Sano: *Journal of Regional Resource Management*. **1**, 35-43 (2021)
[4] S.J. Brotton, R. Shapiro, G. Laan, J. Guo, P. Glans, J. M. Ajello: *Journal of Geophysical Research*. **112** (2007).

Total-Electron-Yield XANES Measurements of Inks Painted on Insulating Copy Papers

Miyu Mamezaki and Yasuji Muramatsu

Graduate School of Engineering, University of Hyogo

Abstract

To non-destructively analyze components of inks painted on papers, X-ray absorption spectra (XAS) of the inks/papers have been measured using a total-electron-yield (TEY) method. TEY-XAS measurements were performed in BL10 at the NewSUBARU. From the C *K*-, N *K*- and O *K*-XANES spectra, ink-components dependent on colors and types of pens could be identified by the TEY-XANES. It is therefore confirmed that components of inks painted on copy papers can be non-destructively detected by using the TEY-XAS method.

1. Introduction

Monitoring the sample current during X-ray irradiation is easy way to measure X-ray absorption spectra (XAS), which is called as a total electron yield (TEY) method. Although numerous XAS studies have used the TEY method to examine electrically conductive materials, it is difficult to apply to insulating bulk materials because electric charge-up distort the XAS. To avoid or suppress charge-up effects of insulating bulk samples during X-ray irradiation, bulk samples are often powdered, and the powdered samples are placed on conductive substrates. We have recently developed another method to easily observe the TEY of insulating samples. In the method, insulating film samples are tightly placed on conductive substrates, and the sample current generated by soft X-ray irradiation can be efficiently detected through the conductive substrates [1]. The TEY-XAS measurements of various insulating samples such as papers, wiping clothes, and organic tapes were performed [2-4], which confirmed that the method would be a powerful tool to non-destructively measure TEY-XAS of insulating samples.

To further apply the present TEY-XAS method for a novel analytical tool, we have measured TEY-XAS of various inks painted on copy papers.

2. Experimental

Samples used in the experiments are shown in Table 1. Commercially-obtained copy papers (denoted as CP) were used for matrix sample. Types of writing pens were black oil-based ballpoint pen (BB), black gel ballpoint pen (GB) and black pencil (PB). All writing pens were made in the same manufacturer.

The ink-painted CPs were cut into small pieces of about 5 mm square, after drying. Each ink was also applied on a gold (Au) substrate to obtain XAS of the ink itself. The ink (X) painted on CP is denoted as X/CP, and the ink coated on the Au substrate is denoted as X/Au. These samples were held on an aluminum plate by conductive carbon tapes as shown in Figure 1. X-ray absorption near-edge structure (XANES) in the C *K*, N *K*, and O *K* regions of the samples were measured in the XAS chamber at BL10/NewSUBARU [5].

3. Results and Discussion

3.1. TEY-XAS

TEY-XAS covering C *K*, N *K*, and O *K* regions of CP, X/CP, and X/Au samples are shown in Figure 2. The black lines exhibit X/CP and red lines X/Au. TEY intensity on the vertical axis is described on the same scale for each region. XANES spectra in the C *K* and O *K* regions can be clearly observed in all the samples. Especially, C *K*- and O *K*-XANES spectra were observed in CP, reflecting the main component of cellulose. Hence, the XANES profiles of CP will be significant backgrounds to identify the ink components in X/CP. Although N *K*-XANE intensity was weak in all the samples, XANES profile can be slightly observed in the 400 – 410 eV region. The N *K*-XANES will also be useful to identify the ink components.

3.2. Comparisons in the C *K*- and N *K*-XANES between X/CP and X/Au

O *K*-XANES profiles of X/CP were as same as CP. Hence, it is difficult to identify the ink components on X/CP from O *K*-XANES.

Table 1. Specifications of the samples.

Label	Component
CP	Copy paper
BB	Oil-based ballpoint pen, black
GB	Gel ballpoint pen, black
PB	Pencil, black

Figure 3 shows the XANES spectra in the C *K* (a) and N*K* (b) regions with the black lines for CP and X/CP, and with the red lines for X/Au. Because XANES spectra of X/Au reflect the ink-only XANES, spectra between the X/CP and X/Au were compared to confirm the ink components on CP. In the C *K*-XANES, CP-derived peaks were observed in X/CP. However, ink-derived characteristic peaks were observed in the range of 287 - 293 eV, which can be identified in X/Au. Additionally, the ink-derived characteristic peaks were dependent on writing pens. This suggests that the writing pens can be identified even in X/CP. In N *K*-XANES, spectra of X/Au exhibit the small S/N ratio due to

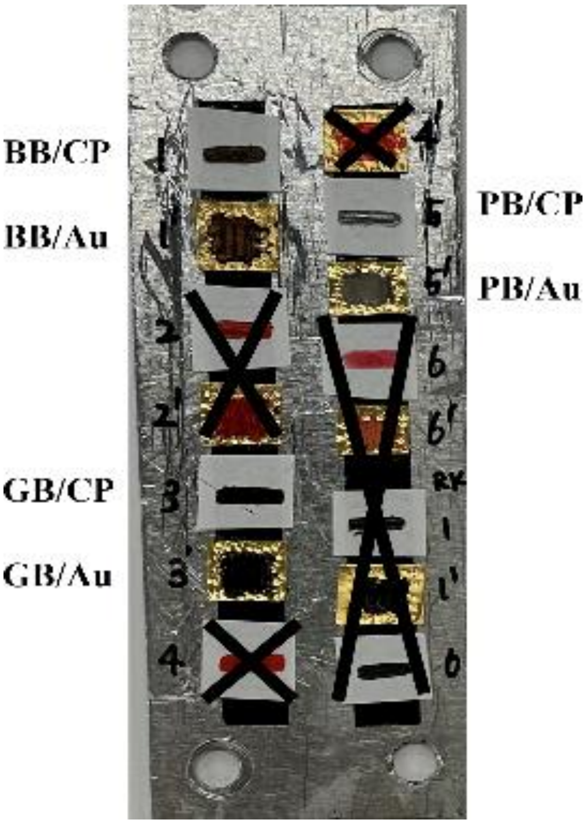

Figure 1. Photo of the sample plate.

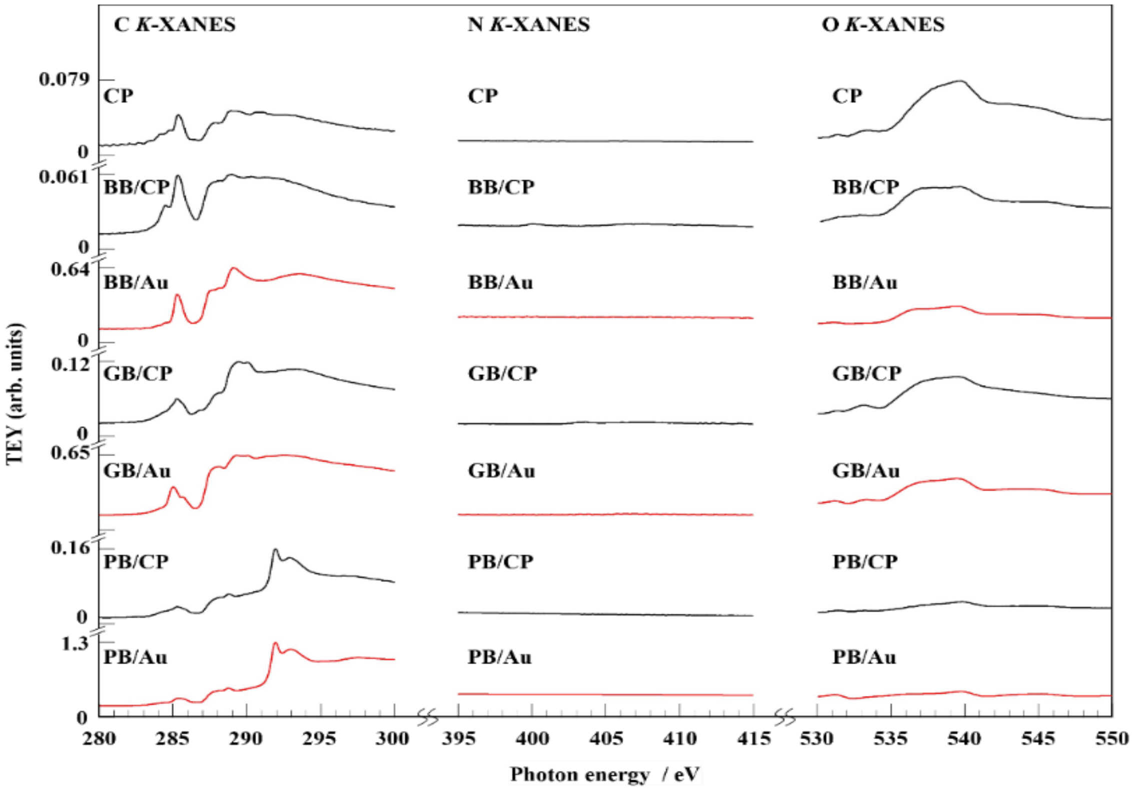

Figure2. TEY-XAS covering C *K*, N *K*, and O *K* regions of CP, X/CP, and X/Au.

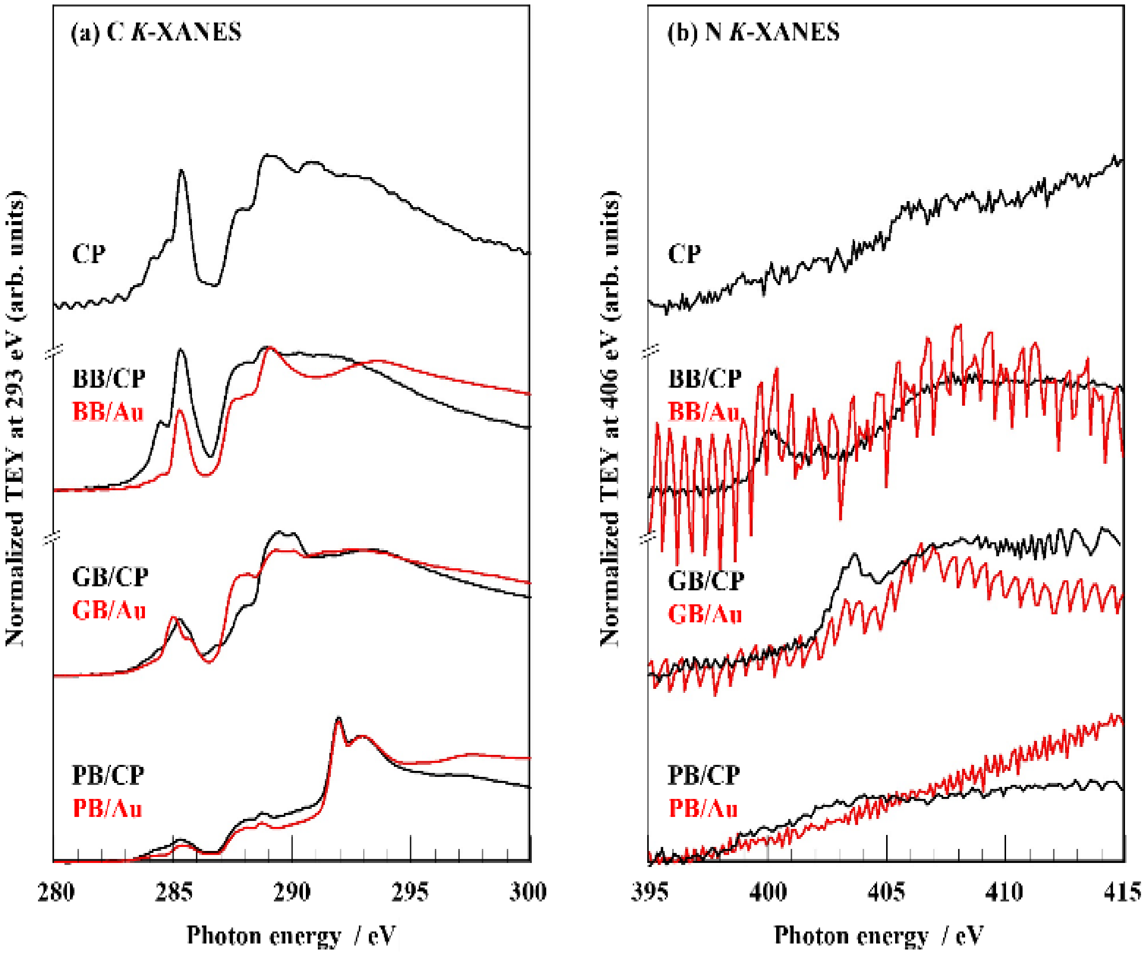

Figure 3. Comparison between the X/CP (black lines) and X/Au (red lines) of XANES spectra in C *K* (a) and N *K* (b) regions.

some experimental errors. However, BB/CP, GB/CP, and PB/CP clearly exhibit characteristic peaks in N *K*-XANES, which are dependent on writing pens. This suggests that types of writing pens will be identified from N *K*-XANES as well as C *K*-XANES.

References

[1] Y. Muramatsu and E. M. Gullikson: *Anal. Sci.*, **36**, 1507-1513 (2020).
[2] Y. Muramatsu, Y. Tani, Y. Tobita, S. Hamanaka, and E. M. Gullikson: *Adv. X-ray Chem. Anal., Japan* **49**, 219-230 (2018).
[3] Y. Muramatsu, R. Maruyama, and E. M. Gullikson: *Adv. X-ray Chem. Anal., Japan* **51**, 179-190 (2020).
[4] R. Maruyama and Y. Muramatsu: *Adv. X-ray Chem. Anal., Japan* **53**, 243-256 (2022).
[5] T. Uemura, Y. Muramatsu, K. Nambu, D. Fukuyama, M. Kuki, T. Harada, T. Watanabe, and H. Kinoshita: *Adv. X-Ray Chem. Anal. Japan* **46**, 317-325 (2015).

In-situ XANES Measurements of Peptide Bonds in Thermal Denaturation of Proteins in Eggs

Ikuya Shimogaki and Yasuji Muramatsu

Graduate School of Engineering, University of Hyogo

Abstract

We have recently measured *in-situ* XANES spectra of egg yolk and egg white during heating, and spectral changes were successfully observed due to thermal denaturation. To clarify the chemical transformation of proteins, XANES spectra of various related compound were measured and the thermal-denaturized XANES were analyzed through finger-print analysis. It is confirmed that peptide-binding structures can transform in protein molecules during thermal denaturation.

1. Introduction

Proteins are macromolecular compounds consisting of a large number of amino acids linked by peptide bonds. Proteins generally take complex conformations due to hydrogen bonds, disulfide bonds, and hydrophobic interactions. In addition, nonpolar side chains of amino acids aggregate inside the protein structure due to hydrophobic interactions, and hydrophilic side chains of amino acids hydrate with the solvent outside the structure. By heating, molecular structures of proteins drastically change. Intramolecular bonds such as hydrogen bonds are broken and the steric structure disintegrates. This is thermal denaturation of proteins. Such the structures result in thermal denaturation are unique and interesting. Although molecular structures in thermal denaturation of proteins have been commonly and widely analyzed by using X-ray diffraction method, the detailed local structures and chemical transformations have not been well elucidated.

To clarify the chemical transformations of proteins from the view point of chemical bonds, we have recently measured XANES spectra in the C *K*, N *K*, and O *K* regions of egg yolk and egg white during heating, and have successfully observed spectral change in the XANES profiles due to the thermal denaturation [1]. In the present study, we have measured protein-related compounds such as typical amino acids, peptides involved in egg white, and some unsaturated fatty acids, to further analyze the *in-situ* XANES spectra of the heated egg yolk and egg white,

2. Experiments

Protein-related reference compounds of unsaturated fatty acids, amino acids, and dipeptide were commercially obtained. Unsaturated fatty acids were oleic acid, linoleic acid, α-linolenic acid, and γ-linolenic acid. Amino acids were glutamic acid, aspartic acid, leucine, serine, valine, lysine, phenylalanine, alanine, arginine, and glycine. Dipeptide was alanyl leucine.

XANES measurements in the C *K*, N *K*, and O *K* regions were performed in BL10 using a total electron yield (TEY) method at a room temperature [2].

3. Results and Discussion

Figure 1 shows C *K*-XANES spectra of egg yolk heated from RT to 180°C (a) [1] and unsaturated fatty acids (b) [3]. In egg yolk, intensity of shoulder peak at 287.7 eV decreased as the temperature increased. The 287.7 eV shoulder corresponds to the shoulders of unsaturated fatty acids. In the unsaturated fatty acids, the shoulder intensity is dependent on the degree of unsaturation. The shoulder at 287.7 eV is attributed to the sp^3-C in unsaturated fatty acids, and the intensity of the shoulder decreases as the sp^2-C of C=C double bond increases, while the sp^3-C decreases. This suggests that sp^3-C decreases in thermal denaturation of egg yolk.

Figure 2 shows C *K*-XANES spectra of egg white heated from RT to 180°C (a) [1] and dipeptide (alanyl-leucine) with the sum-spectrum of amino acids alanyl and leucine (b). In egg white, intensity of the π^* peak near 285 eV increased and the σ^* peak at 288.3 eV decreased as the temperature increased. This suggests that sp^2-C increases and sp^3-C decreases in thermal denaturation of egg white. This corresponds to above-mentioned egg yolk. A peak was also observed at 284.3 eV in 180°C-heating. Figure 2(b) shows the C *K*-XANES spectra of alanyl-leucine, which has a peptide bond between alanyl and leucine amino acids, and of alanyl and leucine amino acids. Although each alanyl and leucine amino acid has no peak at 284.3 eV, alanyl-

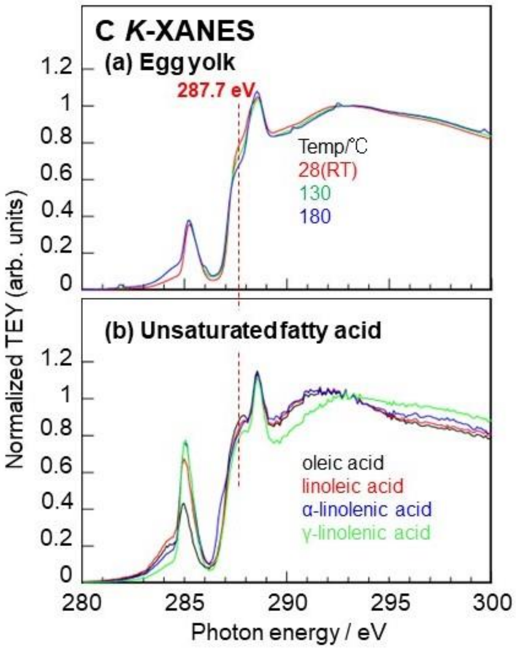

Figure 1. C *K*-XANES spectra of the egg yolk heated up to 180˚C (a) and unsaturated fatty acids (b).

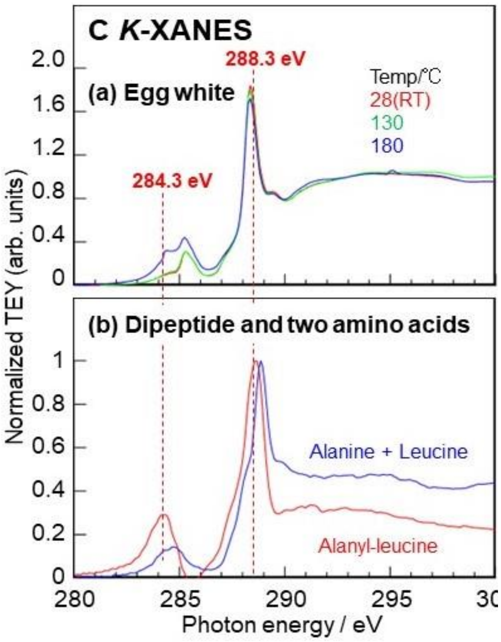

Figure 2. C *K*-XANES spectra of the egg white heated up to 180˚C (a), and dipeptide with two amino acids (b).

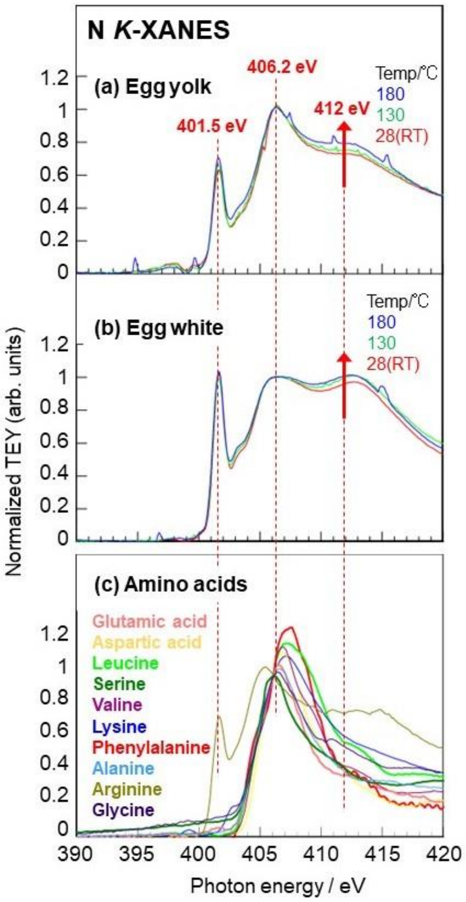

Figure 3 N *K*-XANES spectra of the egg yolk (a), egg white (b) heated up to 180˚C, compared to amino acids (c).

leucine exhibited a peak at 284.3 eV. This means that peptide bonds exhibit the 284.3-eV peak, corresponding to the 284.3-eV peak observed in yolk white heated at 180°C. It is therefore confirmed that peptide bonds can be formed in thermal denaturation.

Figure 3 shows N K-XANES spectra of egg yolk (a), egg white (b), and amino acids (c). Egg yolk and egg white exhibit a sharp peak at 401.5 eV, a main peak at 406.2 eV, and a broad peak near 412 eV. Compared to the amino acids, the 401.5-eV peak corresponds to arginine, and the 406-eV peak almost corresponds to these amino acids. Hence these spectral structures of egg yolk and egg white agree to the elemental amino acids. However, the 412-eV peak dependent on heating temperature does not correspond to the amino acids. This suggests that the 412-eV peak reflects peptide bond formation and the thermal denaturation affects peptide bonds in proteins of eggs.

References

[1] Shimogaki and Y. Muramatsu: *LASTI Annual Report* **23**, 61-62 (2021).
[2] T. Uemura, Y. Muramatsu, K. Nambu, D. Fukuyama, M. Kuki, T. Harada, T. Watanabe, H. Kinoshita: *Adv. X-Ray Chem. Anal. Japan* **46**, 317-325 (2015).
[3] R. Maruyama and Y. Muramatsu: *Adv. X-Ray Chem. Anal, Japan*, **53**, 243-256 (2022).

XANES Spectra in the C *K* and N *K* Regions of Nitrogen-Containing Aromatic Compounds

Saki Yamada and Yasuji Muramatsu

Graduate School of Engineering, University of Hyogo

Abstract

XANES spectra in the C *K* and N *K* regions of aromatic compounds having various nitrogen functional groups were measured to prepare an XANES database for a *fingerprint* analysis of nitrogen-containing graphitic carbon materials. It can be found that carbon atoms directly bonded to nitrogen atoms exhibit characteristic peak structures between π* and σ* peaks in C *K*-XANES. In addition, it was found that each nitrogen functional group exhibited a characteristic peak structure in N *K*-XANES. Such the C *K*- and N *K*-XANES database will be useful for the *fingerprint* analysis of nitrogen-containing graphitic materials.

1. Introduction

Nitrogen-containing graphitic carbon materials such as carbon nitride (CN_x) films and polyacrylonitrile (PAN)-based carbon fibers have attracted much attention in carbon industries. CN_x films are advanced functional materials due to their high elastic recovery rate and mechanical properties. PAN-based carbon fibers are used as composite materials due to their excellent mechanical, electrical and thermal properties. Developments of such nitrogen-containing graphitic carbon materials require local structure analysis to clarify the electronic and chemical bonding states.

Soft X-ray absorption spectroscopy is a powerful tool for the local structure analysis of light-element materials. We have previously reported that chemical state and quantitative analysis of nitrogen atoms in graphitic carbon materials can be successfully achieved by X-ray absorption near-edge structure (XANES) measurements in the C *K* and N *K* regions of reference aromatic compounds having various nitrogenated functional groups [1, 2]. Additionally, XANES database of typical reference compounds will be useful for *finger-print* analysis. Hence, in this study, XANES in the C *K* and N *K* regions of further aromatic compounds having various nitrogenated functional groups were measured to prepare the XANES database for characterization of nitrogen-containing graphitic carbon materials.

2. Experimental

Figure 1 shows the reference aromatic compounds having typical nitrogenated functional (amine, imine) groups; aminopyrene (denoted by A1), carbazole (A2), dimethyltriphenylamine (A3), phenazine (I1), bathophenanthroline (I2), benzo[c]cinnoline (I3), 6-aminoquinoline (AI1), and 9H-pyrido[3,4-b]indole (AI2). These compounds were commercially obtained. These powder samples were held on the indium (In) substrate for XANES measurements. XANES measurements in the C *K* and N *K* regions were performed at BL10 in NewSUBARU by using the total electron yield (TEY) method [3].

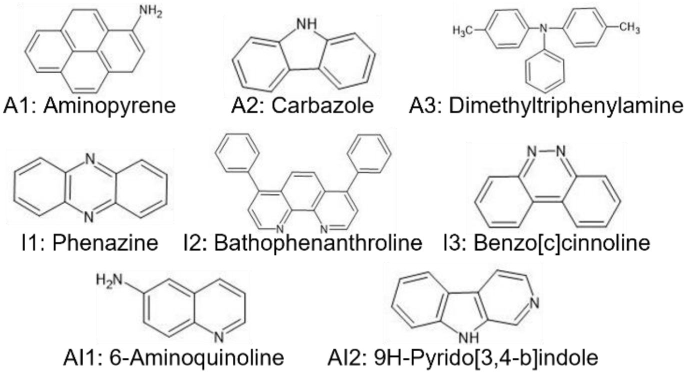

A1: Aminopyrene A2: Carbazole A3: Dimethyltriphenylamine

I1: Phenazine I2: Bathophenanthroline I3: Benzo[c]cinnoline

AI1: 6-Aminoquinoline AI2: 9H-Pyrido[3,4-b]indole

Figure 1. Nitrogen-containing aromatic compounds as reference compounds

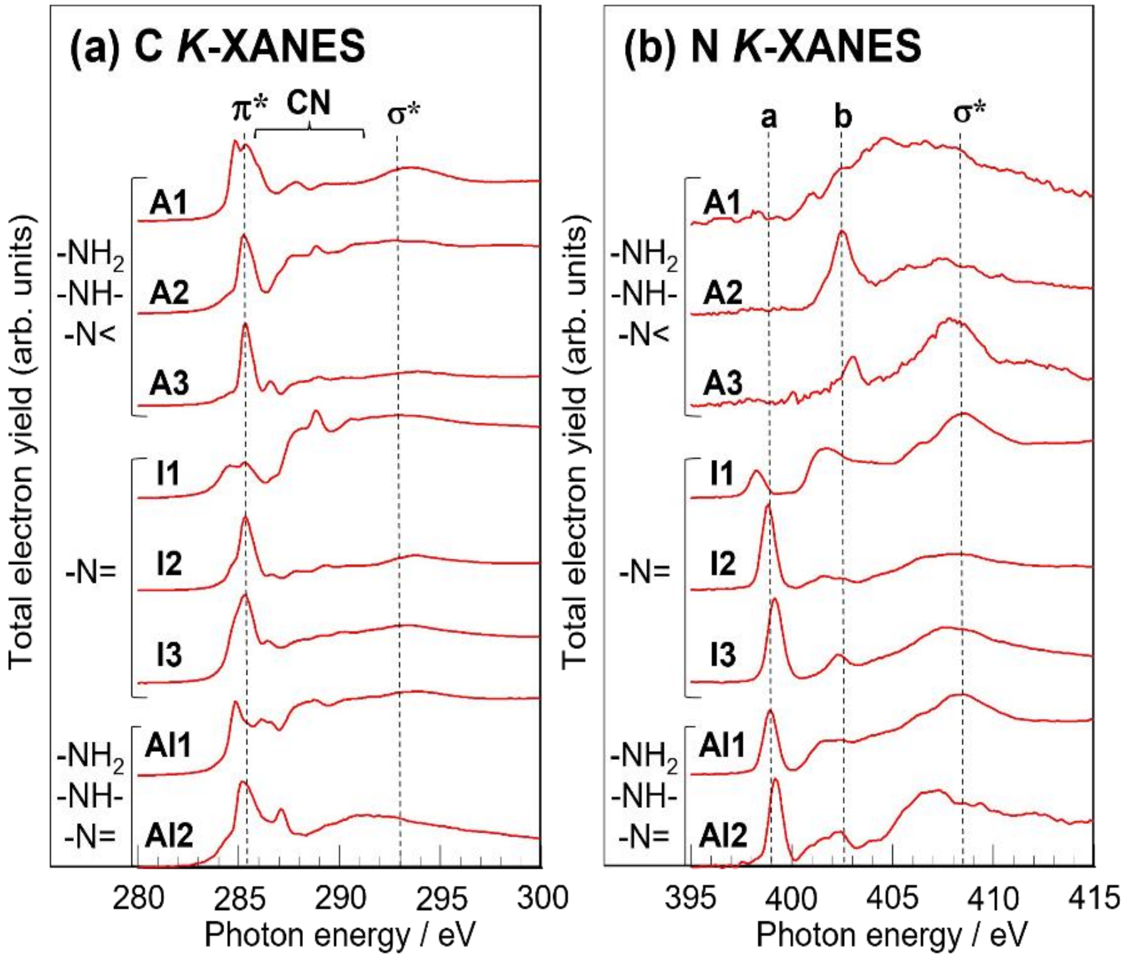

Figure 2. XANES spectra in the C *K* (a) and N *K* (b) regions of the reference compounds.

3. Results and Discussion

C *K*-XANES of the reference compounds is shown in Figure 2 (a). All compounds exhibit the π* peak around 285 eV and σ* peak around 293 eV, reflecting the electronic structure of sp^2-C atoms in the aromatic backbones. Some compounds exhibit the π* peak broadening or splitting. These π* peak profiles usually arise from edge carbon atoms terminated with hydrogen (H) atoms [4]. All compounds exhibit peak structures in the 286 – 290 eV region. This suggests that the π* peaks can shift to the higher energy side due to the formation of hybridized orbitals in the C-N bonds. Hence, various characteristic peak structures can be observed between π* and σ* peaks in C *K*-XANES. In other words, it is necessary to keep this point in mind when analyzing C *K*-XANES of nitrogen-containing graphitic carbon materials.

N *K*-XANES of the reference compounds is shown in Figure 2 (b). All compounds exhibit characteristic peak structures, dependent on nitrogenated functional groups. Compounds having imine nitrogen (I1-3, AI1, AI2) show peak ***a*** around 399 eV. Compounds having amine nitrogen (A1-3, AI1, AI2) exhibit peak ***b*** around 403 eV. It is therefore confirmed that the chemical states of nitrogen atoms can be analyzed from the *fingerprint* analysis using the N *K*-XANES of such the reference compounds.

References

[1] T. Amano, K. Shirode, Y. Muramatsu, and E. M. Gullikson: Jpn. J. Appl. Phys., 52, 041304 (2013).
T. Amano, Y. Muramatsu, N. Sano, J. D. Denlinger, and E. M. Gullikson: *J. Phys. Chem. C* **116**, 6793-6799 (2012).

[2] T. Uemura, Y. Muramatsu, K. Nambu, D. Fukuyama, M. Kuki, T. Harada, T. Watanabe, and H. Kinoshita: *Adv. X-Ray Chem. Anal. Japan* **46**, 317-325 (2015).

[3] Y. Muramatsu, K. Murayama, T. Okada, and T. Ooe: *Anal. Sci.* **37**, 1617-1623 (2021).

Annealing effect on the structure and physical properties of highly hydrogenated diamond-like carbon film

Daisuke Niwa[1], Tomohiro Mishima[1], Koji Nakanishi[1], Naoki Fukumuro[2], Tsuneo Suzuki[3], Kazuhiro Kanda[1]

[1] *Laboratory of Advanced Science and Technology for Industry (LASTI), University of Hyogo*
[2] *Graduate School of Engineering, University of Hyogo*
[3] *Nagaoka University of Technology*

Abstract

The desorption process of highly hydrogenated diamond-like carbon (H-DLC) films due to the annealing was investigated by the measurement of the thermal desorption spectrum of H-DLC film and the temperature dependence on several properties of H-DLC film. Hydrogen molecule ions were desorbed from the H-DLC film at around 360°C and 450°C. On the other hand, hydrocarbon ions were desorbed around 450°C. Film thickness, hydrogen content, and the $sp^2/(sp^2+sp^3)$ ratio of carbon atoms varied significantly in the temperature region higher than 360°C.

1. Introduction

Diamond-like carbon (DLC) films are amorphous carbon films composed of triangularly coordinated (sp^2) carbon atoms, tetrahedrally coordinated (sp^3) carbon atoms, and hydrogen atoms. DLC films possess several useful properties such as high hardness, wear resistance, biocompatibility, and gas barrier[1]. DLC films have already been applied in a wide range of fields such as tools, artificial joints, and plastic bottles, mainly as coating materials. Typical DLC films have a low coefficient of friction in the air and water. However, a coefficient of friction increases in the vacuum[2]. Highly hydrogenated diamond-like carbon (H-DLC) films, that contain more than 40% hydrogen atoms, maintain a low friction coefficient in a vacuum and are expected as solid lubricants in space[3]. However, H-DLC films were reported to desorb hydrogen at a relative low temperature region[4]. In this study, we performed a thermal deposition spectrometry (TDS) study of H-DLC films to examine the temperatures at which various species desorb to investigate the decomposition process of H-DLC film. In addition, samples were prepared by stopping the temperature increase at several temperatures, and a couple of properties were measured. The film thickness and hydrogen content of these samples were measured by the combination technique of Rutherford backscattering spectroscopy and elastic recoil detection analysis (RBS/ERDA) and the $sp^2/(sp^2+sp^3)$ ratio of carbon atoms were evaluated by the measurement of the X-ray absorption near edge structure (XANES).

2. Experimental

H-DLC films were deposited using methane and hydrogen gases by plasma enhanced-chemical vapor deposition method. Si wafer was used as a substrate.

TDS spectra of 20 kinds of ions, mainly hydrogen molecule ions, and hydrocarbon ions, were measured using a quadrupole mass spectrometer, BGM102(ULVAC). A temperature increase rate was 5°C/min and the measured temperature range was from room temperature to 1100°C.

RBS/ERDA spectra were measured using a tandem electrostatic accelerator at the Nagaoka University of Technology. The film thickness was measured by RBS using He^{2+} ions with an energy of 2.0 MeV and hydrogen contents were measured by ERDA using He^{2+} ions with an energy of 2.3 MeV.

XANES measurements were performed at BL09A in NewSUBARU equipped with the grating monochromator. The C-K edge XANES spectra were measured in the energy range from 270 eV to 380 eV with the total electron yield method.

3. Results and Discussion

Figure 1 shows the TDS spectra of hydrogen molecule ion and methyl-, ethyl-, propyl-, and butyl-hydrocarbon ions from room temperature to 900°C for the H-DLC film. No peaks were observed above 900°C in all spectra. Peaks were observed at 360°C and 450°C in the spectrum of the hydrogen molecule ion. It was considered that the peak at 360°C was ascribed to the desorption of hydrogen molecules from the

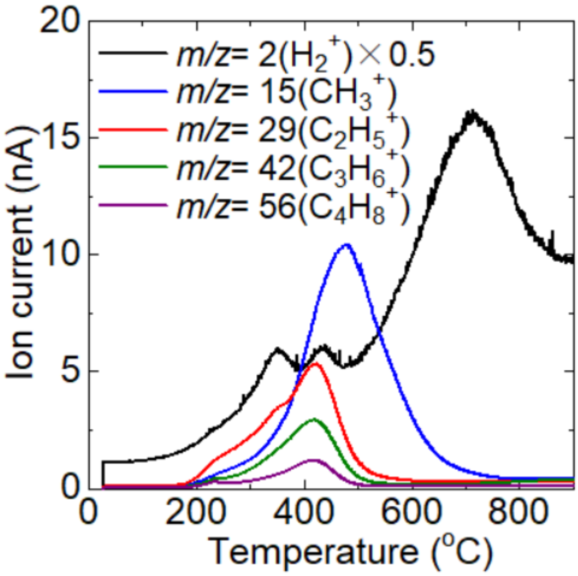

Figure 1. TDS spectra of H-DLC films

H-DLC film because this peak was not observed in the spectra of hydrocarbon ions. In the spectra of methyl ion, the peak was observed near 480°C, and in the spectra of other hydrocarbon ions, peaks appeared near 420°C. In other words, the desorption of carbon atoms from H-DLC film dominantly began in the temperature region higher than 400°C. From these results, we prepared samples by the stopping of temperature increase at several temperatures, such as 200°C, 360°C, 400°C, 450°C, 550°C, and 700°C to discuss the temperature dependence of several film properties of H-DLC film.

Figure 2 shows the temperature dependence of thickness and hydrogen content of the H-DLC films obtained from the RBS/ERDA study. The hydrogen content of the H-DLC film was about 50% before annealing and decreased from 50 % at 360°C to 35% at 400°C by the temperature increase. On the other hand, the film thickness was about 250 nm before annealing. In the temperature region lower than 360°C, the film thickness was maintained at 250 nm and it started to decrease at 360°C. With a further increase in the annealing temperature, the thickness decreased to 40 nm at 700°C.

Figure 3 shows the temperature dependence of the $sp^2/(sp^2+sp^3)$ ratio of carbon atoms which was estimated

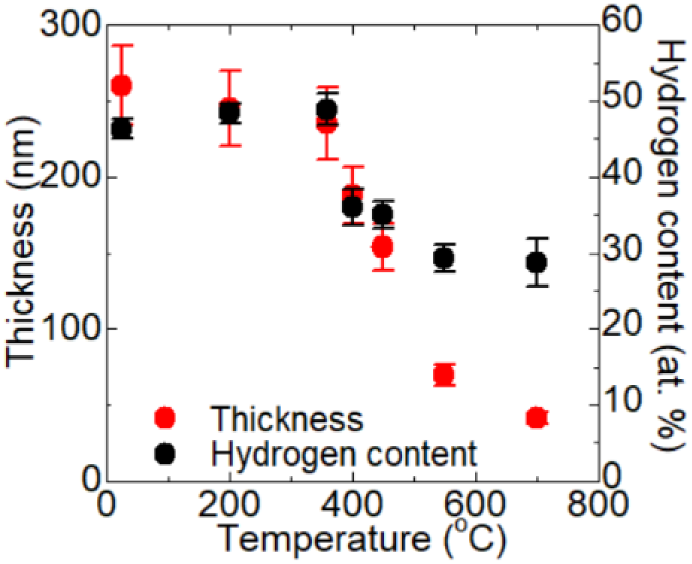

Figure 2. Temperature dependence of the hydrogen content and thickness of the H-DLC films.

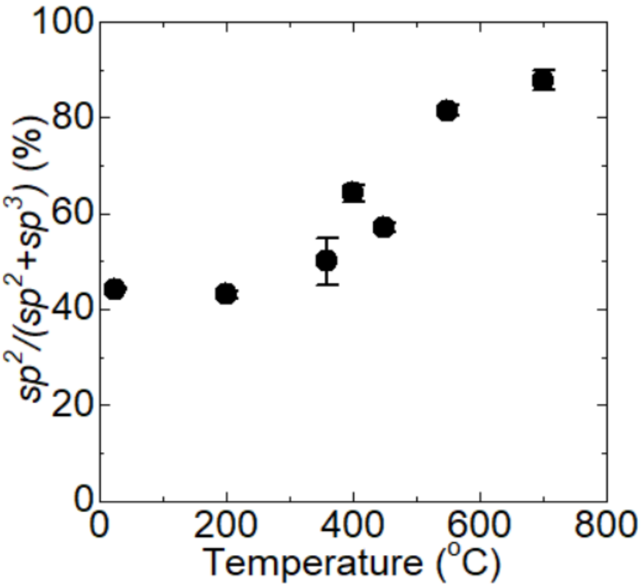

Figure 3. Temperature dependence of the *sp*^{2} /(*sp*^{2}+*sp*^{3})of the H-DLC films.

from the C-K XANES spectrum. The *sp*^{2}/(*sp*^{2}+*sp*^{3}) ratio can be extracted by normalizing the area of the resonance corresponding to the 1*s*→π* transitions at 285.3 eV with a large section of the spectrum [5]. The absolute *sp*^{2}/(*sp*^{2}+*sp*^{3}) ratio was determined by comparing it with that from the XANES spectrum of HOPG. Before annealing, the *sp*^{2}/(*sp*^{2}+*sp*^{3}) ratio of H-DLC film was about 40%. Above 400°C, the *sp*^{2}/(*sp*^{2}+*sp*^{3}) ratio increased. This increase was considerable to be due to the coupling of carbon double bonds by the desorption of hydrogen. Films remaining above 550°C were mostly graphitized.

4. Conclusion

The desorption process of highly hydrogenated DLC films due to increasing temperature was investigated by the measurement of the TDS, RBS/ERDA, and XANES spectra. The results showed that hydrogen molecules desorbed at 360°C, hydrocarbon molecules desorbed at about 450°C. Decreases in film thickness and hydrogen content and increases in the *sp*^{2}/(*sp*^{2}+*sp*^{3}) ratio started above 360°C.

Acknowledgment

I would like to thank Mr. Naoya Iida for helping with my XANES experiment and Mr. Sugimoto belongs to Nagaoka University of Technology for helping RBS/ERDA experiment.

References

[1] J. Robertson: *Curr. Opin. Solid. State. Mat. Sci.*, **1**, 557-561 (1996).

[2] J. Fontaine, C. Donnet, A. Grill, T. LeMogne: *Surf. Coat. Tech.*, **146-147**, 286-291 (2001).

[3] A. Wei, G. Ma, G. Li, Z. Li, C. Han, H. Zhao, W. Guo, Z. Xing, H. Wang: *Diam. Relat. Mater.*, **135**, 1-10 (2023).

[4] H. Li, Tao. Xu, C. Wang, J. Chen, H. Zhou, H. Liu: *Thin. Solid. Films*., **515**, 2153-2160 (2006).

[5] K. Kanda, T. Kitagawa, Y. Shimizugawa, Y. Haruyama, S. Matsui, M. Terasawa, H. Tsubakino, I. Yamada, T. Gejo, M. Kamada: *Jpn. J. Appl. Phys.*, **41**, 4295 (2002).

Scanning electron microscopy of living biological samples

Tomoki Eguchi[1], Yuhei Miki[1], Hidehiro Ishizawa[2], Masahiro Takeo[2], and Satoru Suzuki[1]

[1]*Laboratory of Advanced Science and Technology for Industry (LASTI), University of Hyogo*
[2]*Graduate School of Engineering, University of Hyogo*

Abstract

Scanning electron microscopy (SEM) is an effective analytical tool for observing and analyzing micro- and nanostructures. However, it is very difficult to observe living biological specimens by using a conventional scanning electron microscope because the specimens must be exposed to a vacuum. In this study, we developed a cell that encapsulates biological specimens for analytical techniques in a vacuum, such as SEM. Using the developed cell, we succeeded in scanning electron microscope observation and energy dispersive X-ray analysis of living molds using a conventional scanning electron microscope.

1. Introduction

In recent years, numerous developments in image analysis equipment have given birth to the concept of an imaging complex, in which various analysis devices are used to "deepen our understanding of life by looking at it. Observation of living or wet samples is becoming increasingly essential. However, vacuum analyzers used to observe and analyze microstructures must expose samples to a high vacuum environment ($10^{-5} \sim 10^{-7}$ Pa). If biological specimens are exposed to this pressure, the gases and fluids in their bodies will be deprived, their bodies will shrink, and their microstructures will be severely deformed. For this reason, some researchers have developed instruments such as pre-drying biological samples after applying various scientific pretreatments or using a low-vacuum SEM with a vacuum reduced to about 10^{-2}Pa, but the former results in a loss of microstructure and the latter results in a loss of resolution. However, the former resulted in the collapse of microstructures, while the latter reduced the resolution. Against this background, it is extremely difficult to observe wet samples of living organisms at high magnification and resolution, much less live organisms. To solve this problem, it is necessary to establish a means of observing living biological samples with a vacuum analyzer. Although scanning electron microscopes aim to maintain living morphology as much as possible by applying a number of treatments to biological samples before observation, the current situation is that dead samples are observed[1,2].

In this study, we developed a cell for sealing biological specimens that can be used in a vacuum analyzer. Molds and Wolffia globosa were used as biological samples, and the objective was to observe live biological samples using SEM as a vacuum analyzer. Using the developed cell, molds were observed by general-purpose SEM and qualitatively analyzed by EDS.

2. Experimental

2.1. Sample Preparation

In this study, we used a Si membrane substrate (NTT-AT) with a SiN film as the electron permeable film. We used a 1.5 mm × 1.5 mm window with a film thickness of 200 nm and Si chips with a thickness of 200 µm or 381 µm. In the SEM observation of the cell, it is important to attach the sample to the film because the depth of secondary electron generation in the SEM image detection is very shallow (10 nm).

This experiment was conducted at room temperature in vacuum using an SEM (JEOL, JSM6700F). Observations were made using a secondary electron detection method. Basically, the observation was performed at an acceleration voltage of 20 kV and an irradiation current of 0.25 ~ 0.35 nA, which was changed as necessary. The magnification was set to about 100x.

2.2. Mold Cell Creation

Nutrition, moisture, and temperature are important factors for mold development and growth, and growth can be observed in cells if these factors are sufficiently met. In this experiment, we used mold generated on commercially available miso. To generate the mold, miso was placed flat on a petri dish, and gauze with pure water was placed on the side to maintain sufficient humidity. The petri dish was covered with a lid and placed in an incubator set at 25°C. After one week, mold gradually grew on the miso.

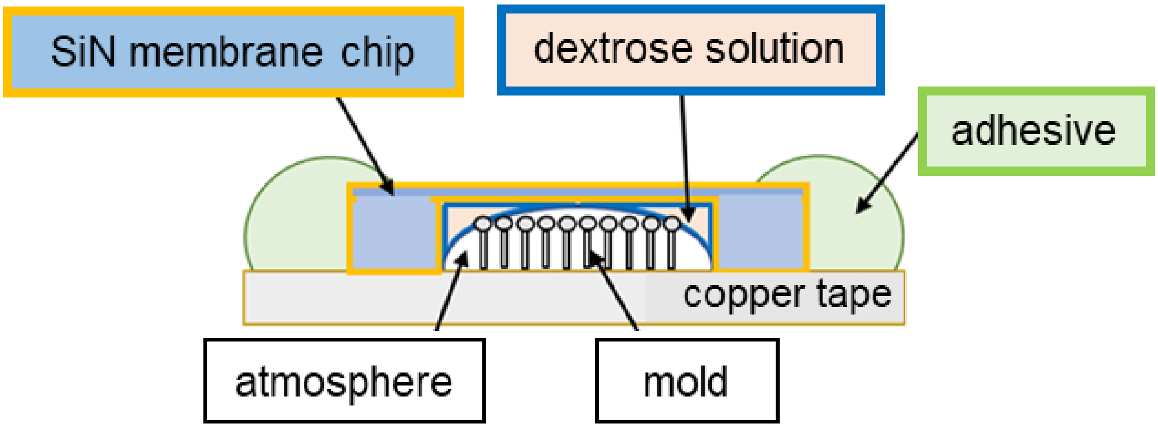

Figure 1. Schematic diagram of a vacuum analysis cell with mold encapsulation.

In order to observe mold growth in the cell, we attempted to grow mold on the membrane instead of attaching mold directly to the membrane. Figure 1 shows a schematic diagram of the vacuum analysis cell in which the mold was encapsulated in this study. The cell is prepared by dropping a glucose solution, which is a nutrient for mold, onto the SiN film of a chip beforehand and allowing the chip to dry for 10 minutes. At this time, a 200 nm thick SiN chip with a 200 μm thick SiN film was used for the chip. The mycelium and spore parts of the mold on the miso were taken out, placed on the copper tape, and the chip was covered from the top to seal it together with the atmosphere. Here, the Si chip was covered with Araldite (Huntsman), a high-performance epoxy-based rapid curing adhesive, to improve sealing.

To allow the mold to grow in the cells, the mold was provided with the conditions for growth: nutrients from glucose, humidity from the moisture in the glucose solution in the cells, and sufficient temperature by storing the cells in an incubator at 25°C.

2.3. Creating a cell of Wolffia globosa

Wolffia globosa is the world's smallest seed plant, consisting of a leafy body that is not divided into roots, stems, or leaves. It is 0.8 mm × 0.4 mm in size, but there are individual differences before and after division. Since it absorbs phosphorus hydrochloric acid and arsenic, it is expected to improve water quality through environmental purification[3] and as a raw material for biomass fuels[4] and biomass plastics. wolffia globosa reproduces through its unique division, which is a determining factor to demonstrate that it is alive in the cell.

Figure 2 shows a schematic diagram of the vacuum analysis cell in which wolffia globosa were encapsulated in this study. wolffia globosa cells were prepared by dropping Schenk & Hildebrandt Basal Salt Mixture (PhytoTech LABS) as the culture medium onto a Si substrate. A single wolffia globosa was placed on top. The cell was sealed with a Si chip, taking care to fill the cell with wolffia globosa and culture medium. A 381 μm thick Si chip with a 200 nm thick SiN was used for the chip. As in the mold cell, the Si chip was covered with Araldite around the chip to improve sealing. The cells were introduced into an incubator set at 25°C and irradiated with plant light for 24 hours.

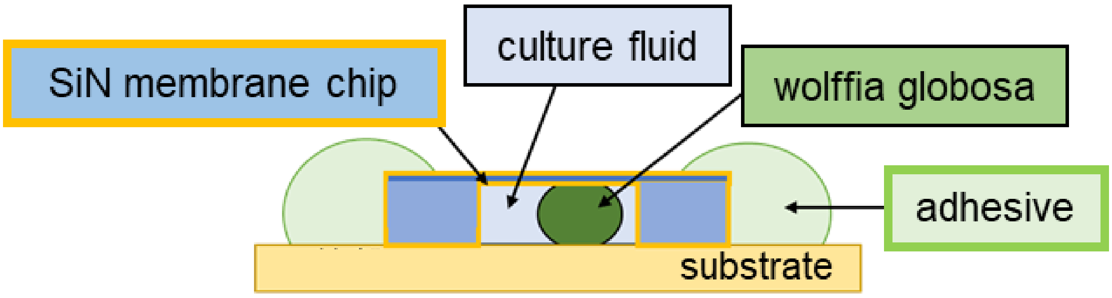

Figure 2. Schematic diagram of a vacuum analysis cell with wolffia globosa encapsulation.

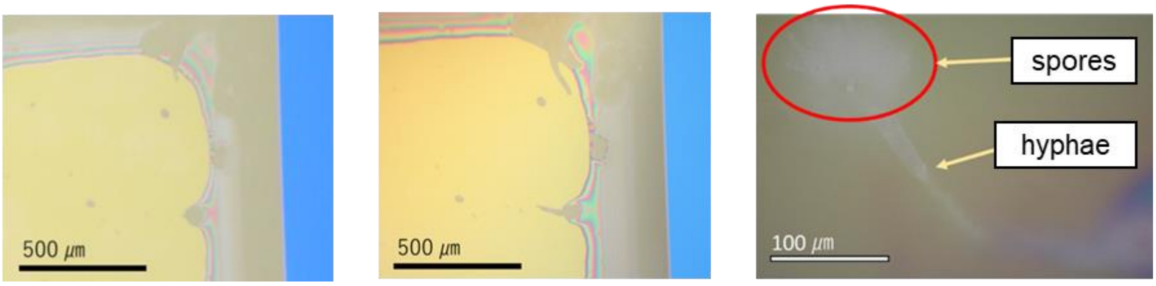

Figure 3. Optical microscopy of mold growing in a cell.

3. Results and Discussion

3.1. SEM Observation of Mold

Progressive observation of the cell revealed new mold from two locations at the edge of the aqueous glucose solution on the membrane surface, as shown in Figure 3 when the magnification was increased, new mold could also be seen at the back. When the focus was changed, each of them came into focus, indicating that the mold had become self-sustaining and formed mycelium and spores. Mold growth could be seen even after sealing in the cell, indicating that the mold was alive inside the cell. The mold cell sample was observed under an optical microscope (BX60M) before and after introduction into the vacuum, and there was no noticeable damage to the sample, confirming that measurements can be made under vacuum. EDS mapping did not show any noticeable problems.

Figure 4 shows the SEM image of the mold, and the mycelium and spores of the mold were also observed by SEM. This indicates that the SEM observation of mold under atmospheric conditions was successful. The diameter of the mycelium was about 10 μm and the spores were less than 100 μm in size.

The depth of secondary electron emission in the SEM is very shallow at 10 nm. Despite the 200 nm thickness of the membrane, we are able to observe the mold on the membrane through the membrane, much less the mycelium and spores of the mold that are free-standing from the membrane. This may be due to the following reasons.

The primary electrons in this observation have sufficiently high energy (20 kV) to pass through the SiN film. The secondary electrons are excited by the electrons inside the sample. The excited electrons affect other electrons, not the direct detection of the excitation energy from the spores. However, since this is only a hypothesis, we will make observations on SiN of several thicknesses and compare the dependence on acceleration voltage and irradiation current in order to elucidate the cause.

3.2. EDS Observation of Mold

Elemental mapping by EDS is shown in Figure 5. It can be seen that carbon and oxygen, the major elements of the organism, as well as phosphorus and potassium, are observed along the mycelium and spores of the mold.

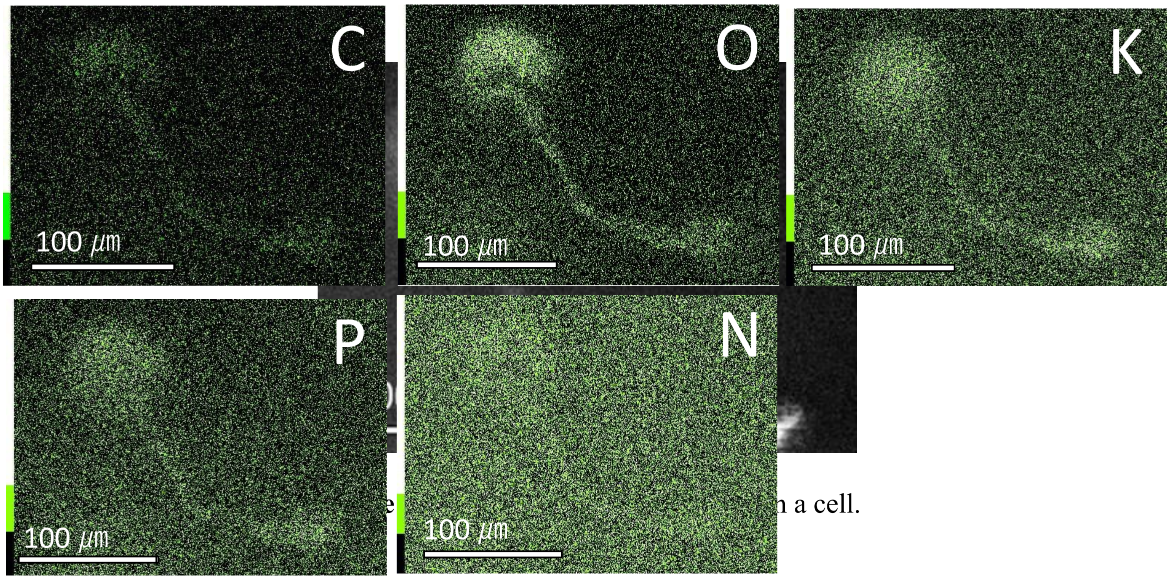

Figure 5. Elemental Mapping of Molds by EDS.

Figure 6 shows the EDS spectra of a mold sticking to the surface of the SiN film and the SiN film. Nitrogen is known to be one of the most abundant elements in living organisms, although it is observed throughout because it is also used as a material for the membrane. Therefore, a point analysis by EDS was performed on the mold and nonmold areas on the membrane, respectively.

Although the same elements are observed from both, perhaps because the mold lives outside the SiN film

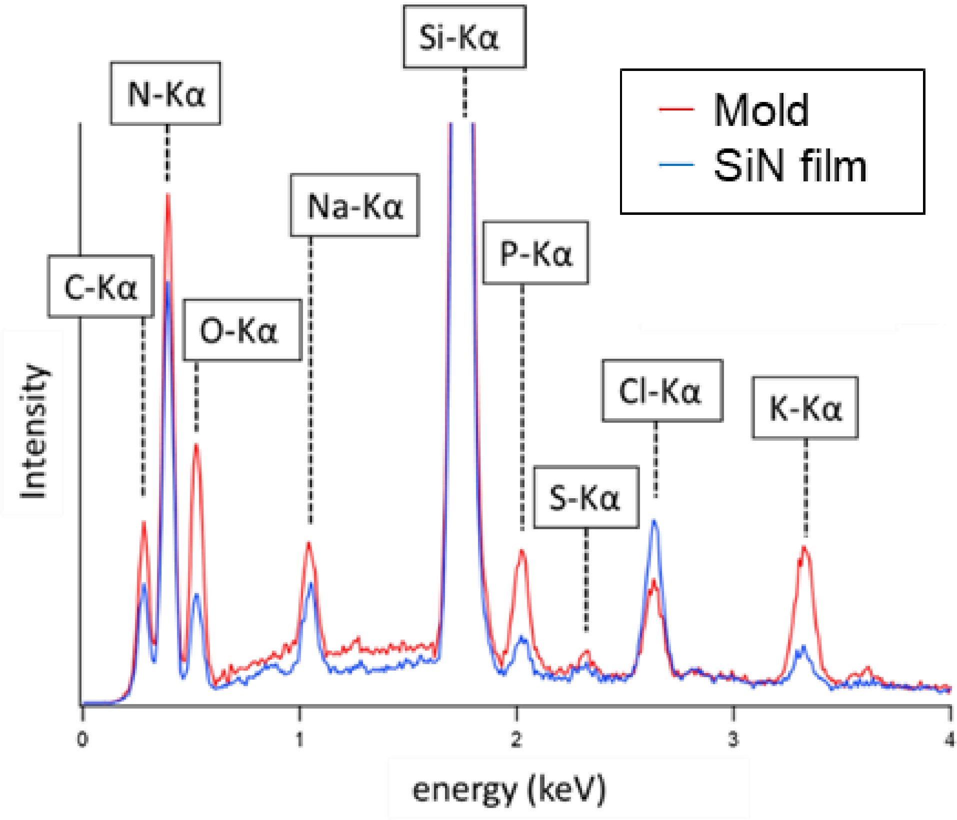

Figure 6. EDS spectra of a mold and the SiN film.

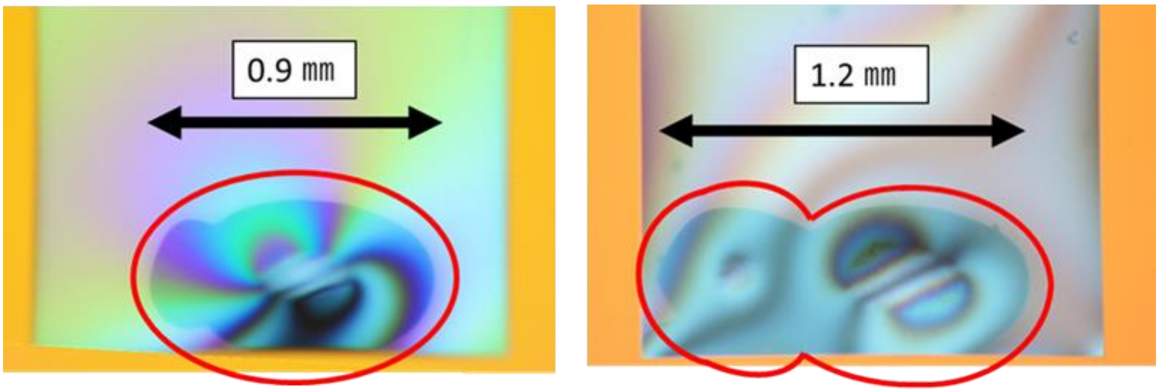

Figure 7. Optical microscopy of wolffia globosa growing in a cell.

surface, it can be confirmed that the carbon, nitrogen, oxygen, phosphorus, and potassium peaks are stronger in the point analysis of the mold. This comparison indicates that the nitrogen peak is also strongly detected in the film mold. Sodium and chlorine are thought to be derived from the salt content of miso, and since soybeans, along with beef and fish, are among the foods that contain sulfur, they are thought to be derived from miso.

3.3. Observation of the growth of wolffia globosa in a cell

Figure 7 shows the growth process of wolffia globosa observed in the cell. The cells were sealed with wolffia globosa and culture medium, and the progress was observed. After 10 days of encapsulation in the cell, division of wolffia globosa was observed, as shown in Figure 7 This occurs when wolffia globosa proliferates, indicating that wolffia globosa is growing inside the cell and that it lives inside the cell for at least 10 days. In the future, we would like to perform vacuum analysis of biological Sample, which is difficult to measure under air because it lives in water, as wolffia globosa does.

4. Conclusion

In the present study, we developed a cell for encapsulating biological samples that can be used in a vacuum analyzer. We succeeded in observing mold in the cell through a 200 nm thick SiN film, and found that the chip used in this study was effective in the development of this cell.

The mold was successfully observed growing in the cell using a commercially available miso, and the cell was used for SEM and EDS observations of the mold under atmospheric conditions. Although we were able to confirm mycelium and spores in the SEM images, growth observation was the main focus of this experiment due to lack of biological knowledge, but we increased our prior knowledge of mold structure and growth process, and conducted observations by type, such as white mold and black mold However, we believe that we can deepen our understanding of molds by increasing our prior knowledge of the structure and growth process of molds and observing different types of molds, such as white molds and black molds.

Although SEM observation of wolffia globosa has not been successful, we plan to develop a cell using a jig for micro-XAFS in order to observe SEM, and at the same time, we plan to use other analytical instruments such as X-ray CT at BL02[5] and photoemission electron microscopy (PEEM) at BL09A. In addition, since wolffia globosa is known to absorb phosphorus hydrochloric acid and nitrogen, we will examine the possibility of linking this to environmental issues such as water quality improvement through environmental purification action by encapsulating what is considered to be those environmental pollutants with the culture medium and observing the progress using EDS.

References

[1] S. R. Aid. et al: *Journal of Physics: Conference Series,* **1447,** 012034 (2020).
[2] Y. takaku, H. Suzuki et al. *J. surf. Sci. Soc. Jpn.*, **36**, No4, 201-206, (2015).
[3] X. Zhang, F.-J. Zhao et al.: *New Phytologist,* **182** 421-428 (2009).
[4] Y. Hubenova, E. Hubenova, M. Mitov.: *J. Elctrochem. Sci. Eng.* **00** (2023).
[5] A. Yamaguchi et al.: *J. Vac. Sci. Technol. B*, in press.

Analysis of emulsions by conventional scanning electron microscopy

Masaki Nakamura, Satoru Suzuki

Laboratory of Advanced Science and Technology for Industry (LASTI), University of Hyogo

Abstract

Liquid samples, including emulsions, are difficult to observe under a vacuum like that of a scanning electron microscope. We applied the liquid cell preparation procedure reported in our laboratory in the past to observe emulsion samples using a conventional scanning electron microscope (SEM). We also performed structural analysis using an energy dispersive X-ray spectrometer. As a result, two types of emulsions were successfully observed in the SEM, and the dispersion of water and oil was confirmed.

1. Introduction

ater and oil are widely known as mutually immiscible relations. Both can be brought into a mixed state by the introduction of surfactants having two properties, hydrophilic and lipophilic groups. A liquid in which these two solutions are dispersed is called an emulsion, and the process of bringing it into an emulsion state is called emulsification. Emulsification technology is utilized in many fields, including cosmetics, food products such as mayonnaise and butter, and adhesives.

The emulsified particles are called the dispersed phase and the medium in which the emulsified particles are dispersed is called the continuous phase, and according to these types, there are four types of emulsions.[1]

The first is the O/W type, in which oil is dispersed in water. The second is W/O type, in which water is dispersed in oil. Then there are W/O/W type emulsions, in which W/O emulsions are dispersed as droplets in water, and O/W/O compound emulsions, in which O/W emulsions are dispersed in oil.

Previous studies on emulsions have reported the observation of the microstructure of emulsions using cryo-SEM method by Yamashita[2] and TEM observation using gelatinized emulsions by Okamoto[3]. However, it is difficult to observe liquid samples such as emulsions as they are under vacuum conditions such as in scanning electron microscopy. Therefore, we applied the liquid cell preparation procedure[4] reported in our laboratory in the past to observe emulsion samples using a conventional SEM. We also used an energy dispersive X-ray spectrometer (EDS) to evaluate the dispersion state of water and oil.

2. Experimental

2.1. Emulsion sample and liquid cell preparation method

Pure water, edible oil (Nissin Canola Oil, Nissin Oillio Group Corporation), and a detergent (Attack Zero, Kao Corporation) were used for the emulsion solution in this study. A micropipette was used to add 1 mL of water, 1 mL of salad oil, and 100 µL of detergent in that order to make a sample. Figures 1 and 2 shows a schematic of the sample structure, and a photograph of the whole sample, respectively.

Copper foil (Niraco Corporation) was cut to a size that would fit into a sample holder for SEM observation

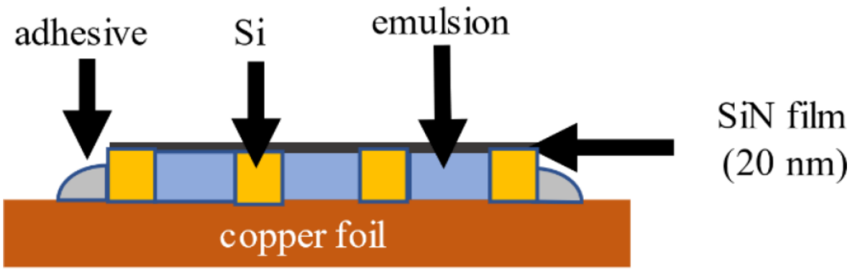

Figure 1. Schematic diagram of the prepared sample.

Figure 2. Completed sample.

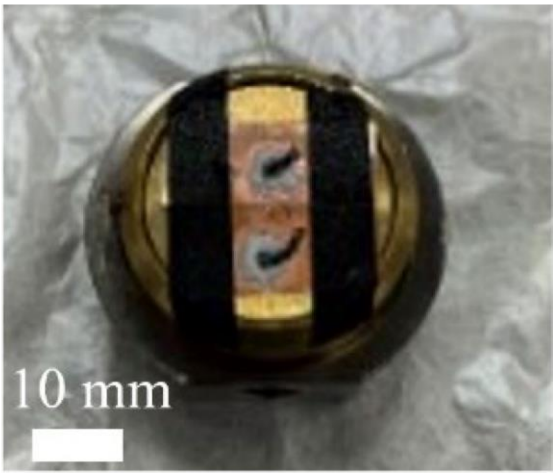

Figure 3. Sample holder for SEM observation after liquid cell installation.

and used as the base. The copper foil was employed to minimize the effect of charge-up of the sample. A 1 µL drop of emulsion sample was dropped into the sample holder with a micropipette, and a Si chip with SiN film (EM Japan Corporation), which is an electron permeable film, was placed on top. The Si chip with SiN film was used in this study because the emulsion sample attached to the SiN film was confirmed by optical

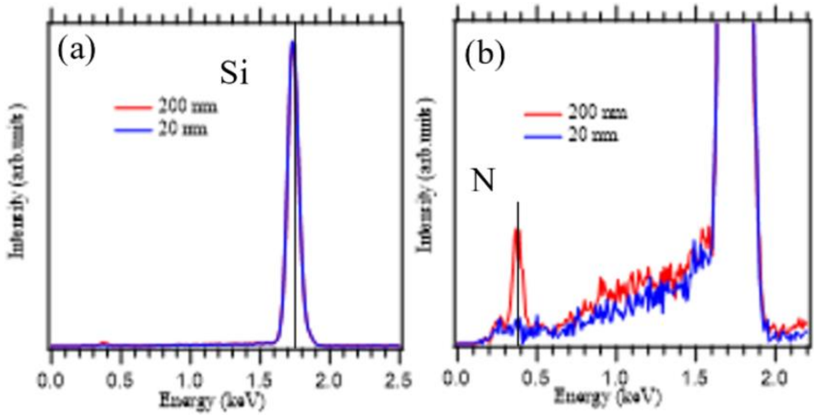

Figure 4. EDS data for 20 nm and 200 nm film thickness. (a) Characterstic X-ray spectrum. (b) Enlarged spectra near light elements.

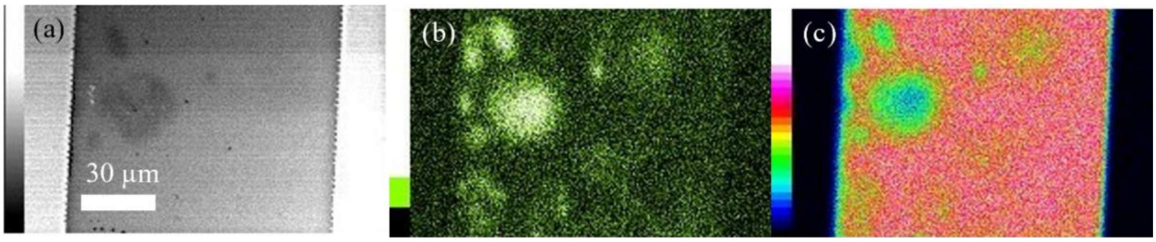

Figure 5. (a) SEM image, (b) C distribution image, (c) O distribution image of emulsion sample.

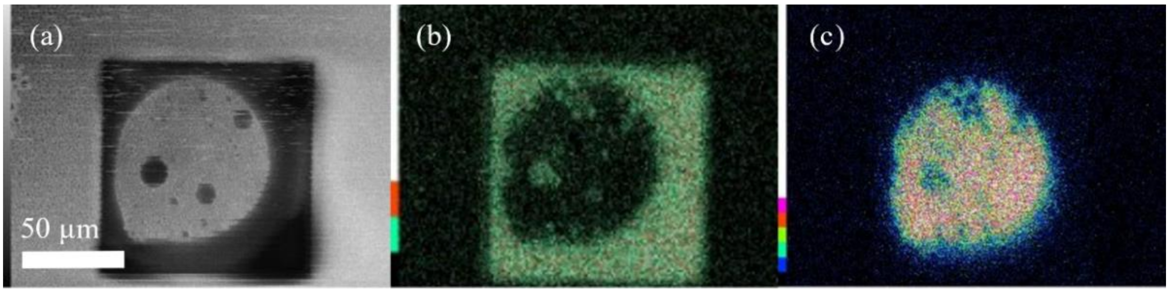

Figure 6. (a) SEM image, (b) C distribution image, (c) O distribution image of emulsion sample.

microscopic observation of the emulsion sample.

In order to obtain a high probability of observation, a chip with 9 windows, a film thickness of 20 nm, and a frame of 100 µm was used. The window consists of 8 windows of 100 µm x 100 µm and 1 window of 100 µm x 350 µm.

2.2. SEM/EDS observation method and measurement conditions

The prepared sample was placed on a sample holder for SEM observation as shown in Figure 3 and fixed with carbon tape. Colloidal graphite (EM Japan Co., Ltd.) was applied across the adhesive to reduce charge-up due to the adhesive between the copper foil and the chip. In this experiment, an SEM (JEOL, JSM6700F) was used for observation in vacuum at room temperature. The acceleration voltage was 20~30 kV. During the EDS measurement, the detector was placed close to the sample and mapping was performed for 30~45 minutes. After mapping was completed, a point analysis evaluation was performed.

3. Results and Discussion

We used EDS to compare the nitrogen spectra of SiN films on Si substrates. Figure 4 (a) shows the spectrum up to 0~2.5 keV, and (b) shows an enlarged spectrum near nitrogen. In the nitrogen spectrum in (b), it was confirmed that nitrogen was almost undetectable in the thinner film. Although the emulsion sample itself does not contain nitrogen, it is considered that nitrogen contained in the liquid sample can be detected with high accuracy by applying the thinner film to the observation of the liquid sample that contains nitrogen.

Figure 5 (a) shows the SEM image and (b) and (c) show the EDS mapping results. On the SiN film in (a), there are structures of various sizes ranging from 3 to 30 µm in size that are slightly darker than the surrounding area, indicating weak detection of secondary electrons. The EDS mapping results show that the C-distributed image in (b) shows a strong intensity, while the O-distributed image in (c) shows a weaker intensity than the surrounding area. Since C is a constituent of oil, we observed an O/W type emulsion with oil dispersed in water.

Figure 6 (a) shows the SEM image and (b) and (c) show the EDS mapping results. Again, several structures of 3 to 15 µm in diameter can be seen. The EDS mapping results show an oil structure in water, confirming an O/W type emulsion. Furthermore, in the O distribution image in (c), the C intensity is strong outside of the strong area, indicating that the O/W emulsion is dispersed in the oil, indicating an O/W/O complex emulsion.

For O/W/O emulsions, point analysis evaluation by EDS was also performed. Figure 7 (a) shows the SEM

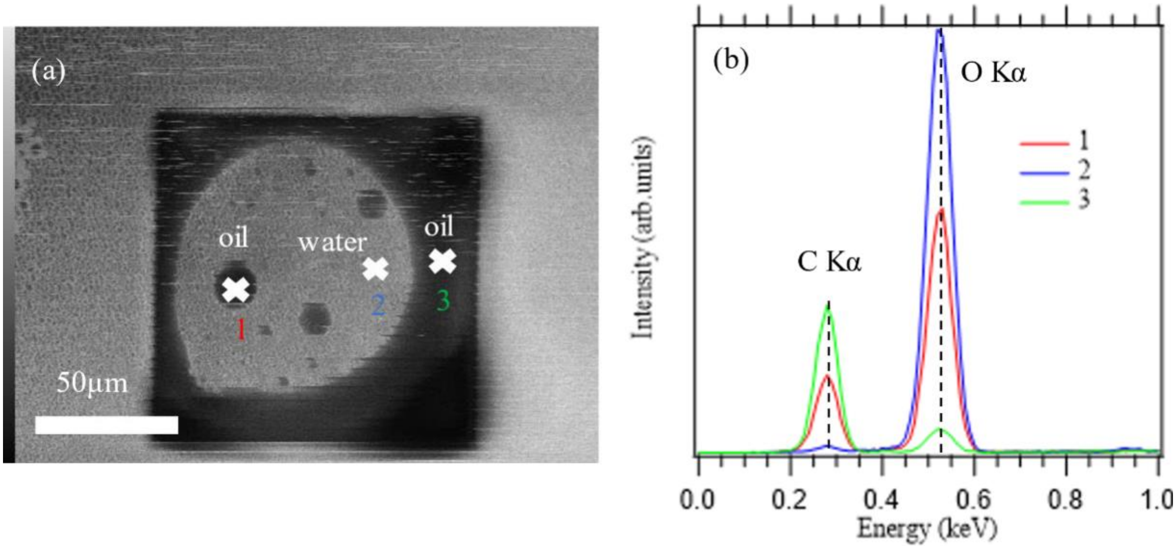

Figure 7. (a) SEM image of an emulsion sample noting the point analysis position. (b) Characterstic X-ray spectrum.

image of the point analysis, and (b) shows the spectral distribution of characteristic X-rays from the point analysis. The oil distribution points 1 and 3 show a strong C Kα line, while the carbon spectrum is almost undetectable in 2. Since oxygen is also a constituent element of oil, it can be confirmed that the oxygen intensities of 1 and 3 are respectively emitted. This indicates that the oxygen spectrum was strongly detected at the location where water was distributed, confirming that oil and water were detected, respectively.

On the other hand, the point 1 was oil, but oxygen was detected more strongly. Possible causes include signals from the surrounding water and the influence of signals from the lower part of the emulsion.

4. Conclusion

The objective of this study was to observe emulsion samples using a conventional SEM, and O/W emulsions and O/W/O emulsions were successfully observed. Qualitative analysis evaluation by EDS point analysis was also conducted to confirm the distribution of water and oil, respectively. The evaluation of SiN film thickness showed that the application of a thin film to the observation of samples containing nitrogen improves the accuracy of qualitative analysis of liquid samples. Furthermore, it was found that sealing of viscous samples such as oil and detergent is possible, indicating that it can lead to the observation of all kinds of liquid samples.

Droplet size distribution (DSD) of emulsions is one of the important properties, and there is a view that the tolerance of emulsions is affected by the size distribution and the smaller the droplet is, the more stable it is[5]. In the future, we aim to observe nano-sized emulsions. Also, we aim to observe nanobubbles and analyze their behavior in emulsion solutions using ultrafine bubbles as a substitute for surfactants.

We are also developing a liquid cell for PEEM, which is considered to be difficult to fabricate, for PEEM, which uses electron lenses to magnify and project the spatial distribution of photoelectrons with a spatial resolution of several tens of nanometers[6]. The PEEM will be used to analyze all kinds of samples under vacuum conditions.

References

[1] T. Suzuki: *J. Soc. Cosmet. Chem. Jpn*, **44**, 103-117 (2010).
[2] M. Yamashita et al: *J. Soc. Cosmet. Chem. Jpn*, **32**, 52-58 (1998).
[3] T, Okamoto et al: *J. Macromolecular Science and Technology*, **75**, 290-292 (2018).
[4] K. Takahara et al: *J. Appl. Phys*, **130**, 025302 (2021).
[5] M. Moradi, V. Alvarado, S. Huzurbazar: *Energy Fuels*, **25**, 260-268 (2011).
[6] M. Kotsugi et al: *J. Surface Science*, **37**, 3-8 (2016).

List of publications

Papers

1. **“Spectral distribution and flux of γ-ray beams produced through Compton scattering of unsynchronized laser and electron beams”**
   Dan Filipescu, Ioana Gheorghe, Kontantin Stopani, Sergey Belyshev, Satoshi Hashimoto, Shuji Miyamoto, and Hiroaki Utsunomiya
   Nuclear Instruments and Methods in Physics Research Section A: Accelerators, Spectrometers, Detectors and Associated Equipment **1047**, 167885 (2022)

2. **“Prediction model of elastic constants of BCC high-entropy alloys based on first-principles calculations and machine learning techniques”**
   G. Hayashi, K. Suzuki, T. Terai, H. Fujii, M. Ogura, and K. Sato
   Science and Technology of Advanced Materials: Methods **2**, 381-391 (2022)

3. **“Difference in Ge and Ni Underlayer for Nanographene Synthesis Using Soft X-ray Irradiation Effects of Ge and Ni catalytic underlayers to nanographene synthesis from pentacene-based film via soft X-ray irradiation”**
   Akira Heya, Kazuhiro Kanda, Ryo Yamasaki, and Koji Sumitomo
   Japanese Journal of Applied Physics **61**, SC1057 (2022)

4. **“An experiment demonstrating the capability of a symmetrical layout type double crystal monochromator controlled using electronic cam technology”**
   Masato Okui, Atsushi Shimoguchi, Naoki Yato, Norio Murayama, Isao Kikuchi, Ichiro Tsuboki, and Kazuhiro Kanda
   Journal of Physics: Conference Series **2380**, 012054 (2022)

5. **“Anion Substitution at Apical Sites of Ruddlesden−Popper-type Cathodes toward High Power Density for All-Solid-State Fluoride-Ion Batteries”**
   Yanchang Wang, Kentaro Yamamoto, Yoshihiro Tsujimoto, Toshiyuki Matsunaga, Datong Zhang, Zulai Cao, Koji Nakanishi, Tomoki Uchiyama, Toshiki Watanabe, Tsuyoshi Takami, Hidenori Miki, Hideki Iba, Kazuhiko Maeda, Hiroshi Kageyama, and Yoshiharu Uchimoto
   Chem. Mater. **34**, 609 (2022)

6. **“Observation of Solid-Liquid Interface Reaction Between High-Capacity Amorphous Si Film Electrode for Lithium Ion Battery and $LiPF_6$ Electrolyte Solution Using Soft X-ray Absorption Spectroscopy”**
   Koji Nakansihi, Takuya Mori, Hiroshi Ohzono, Kazuhiro Kanda, and Satoru Suzuki
   Adv. X-Ray. Chem. Anal., Japan **54**, 185-192 (2023)

7. **“Evaluation of sample charging in near-ambient pressure X-ray photoelectron spectroscopy”**
   Koji Takahara, Kento Takenaka, Hirosuke Sumida, and Satoru Suzuki
   Adv. X-ray Chem. Anal., Japan **54**, 75-80 (2023)

8. **“Cross-sectional Observation of Micro- and Nanobubbles Formed In-situ in a Scanning Electron Microscope”**
   Koji Takahara and Satoru Suzuki
   e-Journal of Surface Science and Nanotechnology **20**, 248-251 (2022)

9. **“Effects of sample-aperture cone distance on the environmental charge compensation in near-ambient pressure hard X-ray photoemission spectroscopy”**
   Satoru Suzuki, Kento Takenaka, Koji Takahara, and Hirosuke Sumida

J. Electron Spectrosc. Relat. Phenom. **257**, 147192-1-9 (2022)

10. **“Soft X-ray Absorption/Emission Spectroscopy and Atomic Hydrogen Irradiation Effect of Ammonia Borane”**
    Masahito Niibe, Yuichi Haruyama, Akira Heya, and Seigo Ito
    e-Journal of Surface Science and Nanotechnology **20**, 226-231 (2022)

12. **“In situ XAFS study on chemical states of Co and Ir nanoparticles under conventional growth condition of single-walled carbon nanotube via alcohol catalytic chemical vapor deposition”**
    Shusaku Karasawa, Kamal Prasad Sharma, Takahiro Saida, Shigeya Naritsuka, Yuichi Haruyama, Toru Asaka, and Takahiro Maruyama
    Chemical Physics Letters **808**, 140135 (2022)

13. “**Comparison of Photoresist Sensitivity between KrF, EB and EUV Exposure**”
    Yosuke Ohta, Atsushi Sekiguchi, Shinji Yamakawa, Tetsuo Harada, Takeo Watanabe, and Hiroki Yamamoto
    Journal of Photopolymer Science and Technology **35**, 49-54 (2022)

14. “**Development of Selenonium PAGs in EUV Lithography toward High Sensitivity Achievement**”
    Tomohito Kizu, Shinji Yamakawa, Takeo Watanabe, Seiji Yasui, and Tomoyuki Shibagaki
    Journal of Photopolymer Science and Technology **35**, 55-59 (2022)

15. “**Grazing-Incidence Soft-X-ray Scattering for the Chemical Structure Size Distribution Analysis in EUV Resist**”
    Atsunori Nakamoto, Shinji Yamakawa, Tetsuo Harada, and Takeo Watanabe
    Journal of Photopolymer Science and Technology **35**, 61-65 (2022)

16. **“Micro Stirrer with Heater Mounted on SAW Actuator for High-speed Chemical Reaction”**
    Masatoshi Takahashi, Akinobu Yamaguchi, Yuichi Utsumi, Masahiro Takeo, Satoshi Amaya, Hiroaki Sakamoto, and Tsunemasa Saiki
    Journal of Photopolymer Science and Technology **35**, 147-151 (2022)

17. **“Evaluation of Surface-Enhanced Raman scattering substrate consisting of gold nanoparticles grown on nanoarrays of boehmite fabricated using magnetron sputtering process”**
    Taku Tanaka, Shyunya Saegusa, Masayuki Naya, Takao Fukuoka, Sho Amano, Yuichi Utsumi, and Akinobu Yamaguchi
    Journal of Photopolymer Science and Technology **35**, 249-253 (2022)

18. **“Determination of radiation dose leading to molecular chain destruction of amino acids”**
    Shyunya Saegura, Ryo Nakamura, Naoya Akamatsu, Yuichi Utsumi, Tomoko Ishihara, Masaki Oura, and Akinobu Yamaguchi
    Journal of Photopolymer Science and Technology **35**, 255-260 (2022)

19. **“Microtaggant Technology for Ensuring Traceability of Pharmaceutical Formulations: Potential for Anti-counterfeiting Measures, Distribution and Medication Management”**
    Toshiya Yasunaga, Takao Fukuoka, Akinobu Yamaguchi, Noriko Ogawa, and Hiromitsu Yamamoto
    YAKUGAKU ZASSHI **142**, 1255-1265 (2022)

20. **“Physical Stability of Stealth Nanobeacon using Surface-Enhanced Raman Scattering for Anti-counterfeiting and Monitorring Medication Adherence: Depostion on Various Coating Tablets”**
    Toshiya Yasunaga, Takao Fukuoka, Akinobu Yamaguchi, Noriko Ogawa, and Hiromitsu Yamamoto
    International Journal of Pharmaceutics **624**, 121980 (2022)

21. **“Uniaxial in-plane magnetic anisotropy mechanism in Ni, Fe, and Ni-Fe alloy films deposited on single crystal Y-cut 128° $LiNiO_3$ using magnetron sputtering”**

Masayoshi Ito, Shota Ono, Hayato Fukui, Keiichi Kogirima, Natusmi Maki, Tatsuo Hikage, Takeshi Kato, Takuo Ohkochi, Akinobu Yamaguchi, Mutsuhiro Shima, and Keisuke Yamada
Journal of Magnetism and Magnetic Materials **564**, 170177 (2022)

22. **"Design and Fabrication of PTFE Substrate-Integrated Waveguide Butler Matrix for Short Millimeter Waves"**
Mitsuyoshi Kishihara, Kaito Fujitani, Akinobu Yamaguchi, Yuichi Utsumi, and Isao Ohta
IEICE Transactions on Electronics **E106-C**, 111-115 (2023)

23. **"The effect of pH on X-ray-radiolysis-induced synthesis of nickel nanoparticles on lithium niobate substrates"**
Shyunya Saegusa, Ikuya Sakurai, Ikuo Okada, Yuichi Utsumi, Keisuke Yamada, Mutsuhiro Shima, Atsushi Yamaguchi, Mari Ishihara, and Akinobu Yamaguchi
Materials Science & Engineering **B 287**, 116093 (2023)

24. **"Development and evaluation of microwave microfluidic devices made of Polydimethylsiloxane"**
Ryota Tanaka, Tomoyuki Nakano, Kaito Fujitani, Mitsuyoshi Kishihara, Akinobu Yamaguchi, and Yuichi Utsumi
Jpn. J. Appl. Phys. **62**, SG1027 (2023)

25. **"Study on magnetization dynamics modulated by spin-orbit-torque in a $Ni_{81}Fe_{19}$/NiO/$Ni_{81}Fe_{19}$ multilayered wire"**
Akinobu Yamaguchi, Nobuko Matsumoto, Wataru Yoshikawa, and Yasuhisa Fujii
AIP Advances **13**, 025341 (2023)

26. **"Oriented sp^2 bonded carbon structure of hydrogenated amorphous carbon films"**
Naoki Umada, Kazuhiro Kanda, Masato Niibe, Yuki Hirata, Naoto Ohtake, and Hiroki Akasaka
Diamond and Related Materials **131**, 109533 (2023)

Books

1. **“Materials and Microfabrication for Biosensing “**
   Akinobu Yamaguchi
   Edited by Editorial committee of Materials and Microfabrication for Biosensing
   CORONA PUBLISHING, 2022 (ISBN 978-4-339-07278-5)

Proceedings

1. **“Application of laser inverse Compton photon on measurement of photoneutron production double differential cross section“**
   Toshiya Sanami, Tuyet Tran, Thuong Nguyen, Hirohito Yamazaki, Toshiro Itoga, Yoichi Kirihara, Yoshihito Namito, Hiroshi Nakashima, Syuji Miyamoto, Satoshi Hashimoto, and Yoshihiro Asano
   Proceedings of 19th Annual Meeting of Particle Accelerator Society of Japan, p.70 (2022)

2. **“Ultrashort laser light source for demonstrating the monocycle FEL scheme”**
   Yuichiro Kida, Satoshi Hashimoto, Shuji Miyamoto, Tadashi Togashi, Hiromitsu Tomizawa, Sumiyuki Okabe, Aoi Gocho, Keisuke Kaneshima, Yoshihito Tanaka, and Takashi Tanaka
   Proceedings of 19th Annual Meeting of Particle Accelerator Society of Japan, p.75 (2022)

3. **“Real-time analysis of betatron oscillation waveforms using machine learning at the NewSUBARU storage ring”**
   Hitoshi Fujii, Keisuke Watanabe, and Satoshi Hashimoto
   Proceedings of 19th Annual Meeting of Particle Accelerator Society of Japan, p.557 (2022)

4. **“Present status of the NewSUBARU synchrotron light facility”**
   Satoshi Hashimoto, Hitoshi Fujii, Tatsuyuki Sakurai, Takahiro Ushizawa, Yasuyuki Minagawa, Kazuyuki Kajimoto, Shotaro Nakata, and Hideyuki Hirayama
   Proceedings of 19th Annual Meeting of Particle Accelerator Society of Japan, p.1119 (2022)

5. **“Current Status and Prospect for EUV Lithography”**
   Takeo Watanabe, Tetsuo Harada, and Shinji Yamakawa
   RadTech Asia 2022, S4-01 (2022)

Reviews

1. **“Existence of nanobubbles and surface nanobubbles”**
   Satoru Suzuki
   Vac. Surf. Sci. **65**, 594 (2022)

2. **“Introduction to Laboratory of Advanced Science and Technology for Industry, University of Hyogo”**
   Satoru Suzuki
   Materia Japan **62**, 131 (2023)

International Meetings

1. **“An experiment demonstrating the capability of a symmetrical layout type double crystal monochromator controlled using electronic cam technology”**
   Masato Okui, Atsushi Shimoguchi, Naoki Yato, Norio Murayama, Isao Kikuchi and Ichiro Tsuboki, and Kazuhiro Kanda
   14th International Conference on Synchrotron Radiation Instrumentation (SRI2021), Online, 2022/3-4

2. **“EUV Research Activities at NewSUBARU”**
   Takeo Watanabe, Tetsuo Harada, and Shinji Yamakawa
   IEUVI Resist TWG Workshop 2022, Online, 2022/4

3. **“Hydrogen Cleaning Evaluation of Mo/Si Multilayer using an EUV Irradiation Tool at NewSUBARU”**
   Tetsuo Harada, Shinji Yamakawa, and Takeo Watanabe
   Photomask Japan 2022, Online, 2022/4

4. **“Development of Grazing-Incidence Coherent EUV Scatterometry Microscope for Resist Pattern Observation”**
   Naoya Kawakami, Tetsuo Harada, Shinji Yamakawa, and Takeo Watanabe
   Photomask Japan 2022, Online, 2022/4

5. **“Functionalization of an Inner-wall of Diamond-like Carbon Coated Small-diameter Long-sized Tube by Oxygen Plasma Treatment”**
   Yuichi Imai, Tatsuyuki Nakatani, Shinsuke Kunitsugu, Kazuhiro Kanda, Yasuhiro Fujii, Daiki Ousaka, Susumu Oozawa, and Tomio Uchi
   2022 MRS Spring Meeting, Hybrid, 2022/5

6. **“Investigation of Free Volume in Diamond-like Carbon Films Using a Slow Positron Beam”**
   Kazuhiro Kanda, Tomohiro Mishima, Hiroki Akasaka, Fuminobu Hori, Atsushi Yabuuchi, and Atsushi Kinomura
   15th International Conference on New Diamond and Nano Carbons (NDNC2022), Kanazawa Bunka Hall, Japan, 2022/6

7. **“Effects of Sample-Aperture Cone Distance on Environmental Charge Compensation in Hard X-ray Photoelectron Spectroscopy”**
   Kento Takenaka, Koji Takahara, Hirosuke Sumida, and Satoru Suzuki
   9th Int. Conf. on Hard X-ray Photoelectron Spectroscopy (HAXPES 2022), Online, 2022/6

8. **“Determination of radiation dose leading to molecular chain destruction of amino acids”**
   Shunya Saegusa, Ryo Nakamura, Naoya Akamatsu, Yuichi Utsumi, Tomoko Ishihara, Masaki Oura, and Akinobu Yamaguchi
   ICPST-39, Online, 2022/6

9. **“Evaluation of Surface-Enhanced Raman scattering substrate consisting of gold nanoparticles grown on nanoarrays of boehmite fabricated using magnetron sputtering process”**
   Taku Tanaka, Syunya Saegusa, Masayuki Naya, Takao Fukuoka, Yuichi Utsumi, Sho Amano, and Akinobu Yamaguchi
   ICPST-39, Online, 2022/6

10. **“Micro Stirrer with Heater Mounted on SAW Actuator for High-speed Chemical Reaction”**
    Masatoshi Takahashi, Yuichi Utsumi, Akinobu Yamaguchi, Masahiro Takeo, Satoshi Amaya, Hiroaki Sakamoto, and Tsunemasa Saiki

ICPST-39, Online, 2022/6

11. **“Grazing-Incidence Soft-X-ray Scattering for the Chemical Structure Size Distribution Analysis in EUV Resist”**
Atsunori Nakamoto, Shinji Yamakawa, Tetsuo Harada, and Takeo Watanabe
ICPST-39, Online, 2022/6

12. **“Development of Selenonium PAGs in EUV Lithography toward High Sensitivity Achievement”**
Tomohito Kizu, Shinji Yamakawa, Takeo Watanabe, Seiji Yasui, and Tomoyuki Shibagaki
ICPST-39, Online, 2022/6

13. **“Comparison of Photoresist Sensitivity between KrF, EB and EUV Exposure”**
Yosuke Ohta, Atsushi Sekiguchi, Shinji Yamakawa, Tetsuo Harada, Takeo Watanabe, Hiroki Yamamoto, Shinji Yamakawa, Ako Yamamoto, Seiji Yasui, Takeo Watanabe, and Tetsuo Harada
ICPST-39, Online, 2022/6

14. **“Research Activities Including the Hydrogen Brittle Evaluation in EUVL at NewSUBARU”**
Takeo Watanabe, Tetsuo Harada, and Shinji Yamakawa
2022 EUVL Workshop, Online, 2022/6

15. **“Study on spin-orbit-torque-induced magnetization modulation using rectifying plannar Hall effect”**
Akinobu Yamaguchi, Nobuko Matsumoto, Wataru Yoshikawa, and Yasuhisa Fujii
Joint European Magnetic Symposia (JEMS2022), Warsaw, Poland, (Hybrid), 2022/7

16. **“Photon Flux Density Dependence of Nanographene Synthesis by Soft X-ray Irradiation from Pentacene-based Molecules Prepared on Ni Films by Hot Mesh Deposition”**
Akira Heya, Kazuhiro Kanda, Ryo Yamasaki, and Koji Sumitomo
29th International Workshop on Active-Matrix Flatpanel Displays and Deviceses(AMFPD2022), Ryukokou Univ., Kyoto, Japan, 2022/7

17. **“Spin transport properties in multilayer including Pt and NiO layers”**
Akinobu Yamaguchi
Joint European Magnetic Symposia (JEMS2022), Warsaw, Poland, (Hybrid), 2022/7

18. **“Structural changes of highly hydrogenated DLC films by SR irradiation”**
Kazuhiro Kanda, Daisuke Niwa, Tomohiro Mishima, Masahito Niibe, Hiroki Akasaka, Fuminobu Hori, Atsushi Yabuuchi, and Atsushi Kinomura
ASIAN Conference on X-ray Absorption Spectroscopy 2022 (ACXAS2022), NongNooch Pattaya International Convention and Exhibition Center, Pattaya, Thailand, 2022/8

19. **“Current Status and Prospect for EUV Lithography”**
Takeo Watanabe, Tetsuo Harada, and Shinji Yamakawa
RadTech Asia 2022, Tsukuba, Japan, 2022/8

20. **“Comparative Study of Atomic Hydrogen Exposure on Hydrogenated and Hydrogen-Free Amorphous Carbon Films”**
Yuichi Haruyama, Daiki Morimoto, Akira Heya, Koji Sumitomo, Noriaki Toyoda, and Seigo Ito
22nd International Vaccum Congress (IVC-22), Sapporo, Japan, 2022/9

21. **“Effect of Atomic Hydrogen Exposure on Hydrogen-Free Amorphous Carbon Films”**
Yuichi Haruyama, Daiki Morimoto, Akira Heya, Koji Sumitomo, Noriaki Toyoda, and Seigo Ito
22nd International Vaccum Congress (IVC-22), Sapporo, Japan, 2022/9

22. **“Study on Microfluidic analysis system with molecular sensing based on Surface enhanced Raman Scattering”**
Akinobu Yamaguchi, Taku Tanaka, Shunya Saegusa, Masayuki Naya, Takao Fukuoka, Sho Amano, and Yuichi Utsumi
SSDM 2022, Chiba, Japan, 2022/9

23. **“Chemical Physical Unclonable Functions Taggant for Anti-Counterfeiting and Authentication Systems”**
Akinobu Yamaguchi, Toshiya Yasunaga, Yuichi Utsumi, Kyoko Namura, Momofumi Suzuki, and Takao Fukuoka
MNE2022, Leuven Belgium, 2022/9

24. **“Fabrication and evaluation of SERS structures on boehmite using magnetron sputtering method for molecular sensing”**
Shunya Saegusa, Taku Tanaka, Masayuki Naya, Takao Fukuoka, Sho Amano, Yuichi. Utsumi, and Akinobu Yamaguchi
MNE2022, Leuven, Belgium, 2022/9

25. **“Deviation of photoelectron intensity from the Lambert-Beer’s law in near-ambient pressure hard X-ray photoelectron spectroscopy”**
Kento Takenaka, Koji Takahara, Tomoki Eguchi, Hirosuke Sumida, and Satoru Suzuki
Int. Symp. on Atomic Level Characterizations for New Materials and Devices (ALC 2022), Okinawa, Japan, 2022/10

26. **“Optofluidic device with Gold-nanofève-based-SERS active nanostructure”**
Shunya Saegusa, Taku Tanaka, Masayuki Naya, Takao Fukuoka, Sho Amano, Yuichi Utsumi, and Akinobu Yamaguchi
13th Japan-China-Korea Joint Conference on MEMS/NEMS, Kagoshima, Japan, 2022/10

27. **“On chip organic synthesis by microwave heating in a microchannel coupled with post-wall waveguide”**
Kaito Fujitani, Mitsuyoshi Kishihara, Ryota Tanaka, Tomoyuki Nakano, Akinobu Yamaguchi, and Yuichi Utsumi
13th Japan-China-Korea Joint Conference on MEMS/NEMS, Kagoshima, Japan, 2022/10

28. **“On-chip synthesis of metal complex by microwave heating in a microchannel embedded in post-wall waveguide”**
Kaito Fujitani, Mitsuyoshi Kishihara, Akinobu Yamaguchi, and Yuichi Utsumi
MNC 2022, Tokushima, Japan, 2022/10

29. **“Development and evaluation of microwave microfluidic devices made of PDMS”**
Ryota Tanaka, Tomoyuki Nakano, Kaito Fujitani, Mitsuyoshi Kishihara, Akinobu Yamaguchi, and Yuichi Utsumi
MNC 2022, Tokushima, Japan, 2022/10

30. **“Development of low-energy-electron-flood-exposure tool (LEEFET)”**
Wataru Kusada, Shinji Yamakawa, Tetsuo Harada, and Takeo Watanabe
MNC 2022, Tokushima, Japan, 2022/11

31. **“Study on spin-orbit-torque-induced magnetization modulation using rectifying plannar Hall effect”**
Akinobu Yamaguchi, Nobuko Matsumoto, Wataru Yoshikawa, and Yasuhisa Fujii

Magnetism and Magnetic Materials 2022, Online, 2022/10-11

32. **"Fundamental Research for EUV Lithography at NewSUBARU Synchrotron Light Facility"**
    Takeo Watanabe
    Materials Science, Engineering & Technology, Online, 2022/11

33. **"In situ spectroscopic study of electrochemical deposition processes and molecular sensing using microchemical systems"**
    Akinobu Yamaguchi, Takao Fukuoka, Masaru Kato, Ichizo Yagi, Masaki Oura, and Yuichi Utsumi
    International congress on pure and applied chemistry (ICPAC), Kota kinabalu, sabah, Malaysia, 2022/11

34. **"Technical issue of EUVL and prospect for EUVL and Beyond EUVL"**
    Takeo Watanabe
    7th EUV-FEL Workshop, Tsukuba (hybrid), Japan, 2023/1

35. **"Plasmonic Nanotags for On-dose-authentication of Medical Tablets"**
    Takao Fukuoka, Toshiya Yasunaga, Kyoko Namura, Motofumi Suzuki, and Akinobu Yamaguchi
    Pittcon 2023, Philadelphia, USA, 2023/3

Academic Degrees

Master of Engineering

Naoya Kawakami (University of Hyogo)
"Improvement of Sensitivity of Grazing-Incident Coherent-Scatterometry Microscope for Resist-Pattern Defect Detection"

Koji Takahara (University of Hyogo)
"Observation and shape control of surface microbubbles"

Taku Tanaka (University of Hyogo)
"Fabrication of Imaging Substrates Surface Enhanced Raman Scattering (SERS) and its Mounting on Micro Chemical Chips"

Ryota Tanaka (University of Hyogo)
"Fabrication and evaluation of Microwave Chemical Synthesis chips combined with in situ Raman spectroscopy"

Kozo Tamada (University of Hyogo)
"High-Strength Ni-W Deposition Using the LIGA Process Development of Micro Gears and Micro Turbines"

Tomoyuki Nakano (University of Hyogo)
"Prototyping and Evaluation of Microwave Chemical Synthesis Chip for nano- and microbubble generation"

Daiki Morimoto (University of Hyogo)
"Effect of atomic hydrogen exposure on amorphous carbon films"

Taki Watanabe (University of Hyogo)
"Moving Mask X-ray Lithography High Yield of Submicron Mist by Development and Research of Generating Nebulizer"

Laboratory of Advanced Science and Technology for Industry,
University of Hyogo

3-1-2 Kouto, Kamigori, Ako-gun, Hyogo 678-1205 Japan

兵庫県立大学　高度産業科学技術研究所
〒678-1205 兵庫県赤穂郡上郡町光都3-1-2